Electron and Positron Production in
14.6 A· GeV/c Nucleus-Nucleus Collisions

by

Kevin David Rathbun

Submitted to the Department of Physics
in partial fulfillment of the requirements for the degree of

Bachelor of Science in Physics

at the

MASSACHUSETTS INSTITUTE OF TECHNOLOGY

May 1994

Author . . . .
Department of Physics
May 28, 1994

Certified by . . . .
George F. Stephans
Principal Research Scientist, Laboratory for Nuclear Science
Thesis Supervisor

Accepted by . . . .
Arthur Bernstein
Department of Physics, Undergraduate Thesis Coordinator

Electron and Positron Production in 14.6 A· GeV/c Nucleus-Nucleus Collisions

by

Kevin David Rathbun

Submitted to the Department of Physics
in partial fulfillment of the requirements for the degree of

Bachelor of Science in Physics

at the

MASSACHUSETTS INSTITUTE OF TECHNOLOGY

May 1994

Author ....
Department of Physics
May 28, 1994

Certified by ....
George F. Stephans
Principal Research Scientist, Laboratory for Nuclear Science
Thesis Supervisor

Accepted by ....
Arm Bernstein
Department of Physics, Undergraduate Thesis Coordinator

Electron and Positron Prodution in

14.6 A· GeV/c Nucleus-Nucleus Collisions

by

Kevin David Rathbun

Submitted to the Department of Physics
on May 28, 1990, in partial fulfillment of the
requirements for the degree of
Bachelor of Science in Physics

Abstract

This thesis is a study of electrons and positrons ($e^{\pm}$) produced in relativistic heavy ion collisions at the Brookhaven National Lab. The data was obtained from silicon on gold collisions with 14.6 GeV/c per projectile nucleon. The inefficiency of the gas Cerenkov counter at detecting $e^{\pm}$ was determined to be about 4%. The over-efficiency of the gas Cerenkov counter for detecting $\pi^{\pm}$ was determined to be 10-30% near the beam line, and falling off rapidly to about 2% at reaction angles of 34° to 44°. The contamination of the $e^{\pm}$ data by pions was determined for momenta between .2-1.0 GeV/c. The contamination results were used to determine $e^{\pm}$ yields and the $e^{\pm}$ yields are compared to $\pi^{\pm}$ yields.

Thesis Supervisor: George S. F. Stephans
Title: Principal Research Scientist, Laboratory for Nuclear Science

For George, who kept me sane, and Rita, who drove me crazy. Also, mom and dad.

Contents

List of Figures

9

12

List of Tables

Chapter 1

Introduction

To study the character of relativistic heavy-ion colisions, electron and positron ($e^{\pm}$) data obtained from an experiment performed at the Brookhaven National Lab were analysed. The end results obtained were yields of $e^{\pm}$ in inelastic silicon on gold collisions. To get to this result, functional aspects of the detectors had to be explored in order to understand the meaning of the raw data from the experiments. In the process of determining the yields, the distinction between the physical system being analysed and the experimental detectors used to analyse it were found to be hazy. At one extreme, the dense nuclear matter that is formed in a space several fermi's wide and lasting on the order of 10^{-22} seconds might be considered the physical system. However, the extension of this space-time to include the passage of the produced particles into the spectrometer is a physical system that is also important and interesting to study. In fact, the interactions between the particles and the detectors is a difficult matter, and the question of what is happening in the tiny volume of dense nuclear matter is irrelevant until that is understood. This study is focused on the interplay between the $e^{\pm}$ and several of the detectors in the spectrometer. The response of the gas Cerenkov counter to the particles was analysed. The results of this analysis extended the ability to determine $e^{\pm}$ yields to momenta significantly beyond what was available from the raw data. The efficiency of the gas Cereknov counter at detecting $e^{\pm}$ and $\pi^{\pm}$ was found. Also, the collision multiplicity and angular dependence of these inefficiencies were obtained.

Chapter 2

Experimental Setup

In order to discover the physics of heavy-ion collisions, ^{16}O and ^{28}Si beams accelerated to 14.6 GeV/c per nucleon by the Brookhaven National Laboratory Tandem-AGS accelerator facility were collided into gold and aluminum targets in experiment E859. The present work will examine the data collected from Silicon on Gold collisions collected by a large-solid-angle magnetic spectrometer (figure 2-1). To survey the collisions for events causing particle production, the 25 msr magnetic spectrometer could rotate to reaction angles between 5° and 58°. The experiments were performed in many runs, each of which was rotated to a reaction angle of 5°, 14°, 24°, 34° or 44°. The run angle defined the beam side edge of the spectrometer's approximately 14° acceptance for particle trajectories. This acceptance is defined by the geometry of the tracking chambers on the spectrometer. The spectrometer's anatomy includes a dipole magnet, four tracking chambers, two trigger chambers, a time-of-flight wall (TOF), a gas Cerenkov counter (GasC), and a target multiplicity array (TMA). The spectrometer in combination with a segmented gas Cerenkov (GasC) counter offered good particle identification at momenta between $\sim$ .5 to $\sim$ 5.2 GeV/c and high momentum resolution ($\Delta p/p \leq 0.005$). In order to obtain a well-collimated beam of projectiles for the spectrometer, a system of plastic scintillation counters were responsible for selecting the correct ion species, confirming the beam particle traversed the target, and setting the start for the time-of-flight. The gold foil targets were mounted in remote-controlled movable frames which were kept in vacuum. Three

19
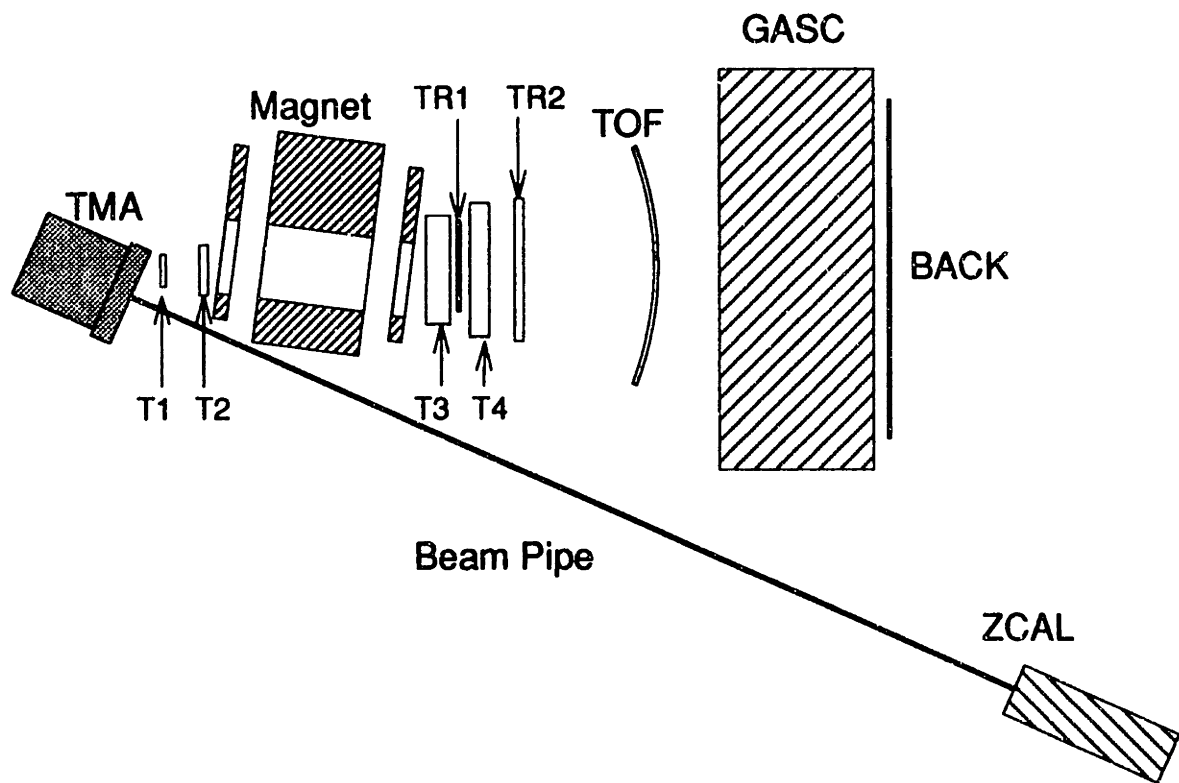
Figure 2-1: E859 Spectrometer

Angle	# Runs	AU3%	AU2%	AU1%	4A	4B	2A	2B
5	121	-	-	121	13	108	-	-
14	18	11	2	5	5	1	3	9
24	6	6	-	-	-	2	3	1
34	3	3	-	-	-	1	1	1
44	6	6	-	-	2	3	1	-

Table 2.1: Number of runs at each spectrometer angle, target thickness, and magnet setting from which data for this analysis was taken.

target thicknesses were used - AU 1%, AU 2% and AU 3% - based on their fraction of the interaction length of a silicon nucleus passing through gold. The TMA is composed of proportional tubes with 3240 copper cathode pads for readout. They are arranged as a barrel surrounding the target along the beam axis and a wall with a hole for the spectrometer forward of the target, which together cover reaction angles from 6° to 149°. The charged particle multiplicity supplied by the TMA is assumed to be an indicator of the centrality of the collision between the nuclei due to the larger overlapping volume between the two nuclei for increased particle production. Typical event multiplicities $\sim$ 250 are measured with small losses of $\sim$ 15 counts due to multiple hits. Charged particles are deflected in the dipole magnet, known as 'Henry Higgins', to determine the momentum. It has a maximum bending power of $\sim$ 1.5 Tesla-meters due to a field which is shaped for maximum homogeneity inside the magnet by correcting coils and minimized outside the magnet by large steel plates. The magnet's field can be set to field values of 2 or 4 kGauss, with either negative (A) or positive (B) polarity. In table 2, the number of runs used at each angle is shown with a breakdown into the types of target used and the magnet polarity and strength.

The B polarity points up and its effect is to bend positrons back toward the beam axis. Because the particles enter the magnet at an angle oblique to the normal of its face, there is an asymmetry in its acceptance of different sign particles. For B polarity, the angular acceptance is wider for positive particles being bent back towards the beam than for negative particles being bent away from the beam. The situation

is reversed for opposite polarity and the difference is magnified for low momenta particles which have a smaller radius of curvature in the magnet. The geometrical acceptance, determined by the two drift chambers on the target side of the magnet, is about $14°$ in polar angle and about $7°$ in azimuthal angle. Along with two other drift chambers behind the magnet, particle tracks are reconstructed through the magnet and projected back to the target. Thus, particles not originating from the target are excluded. The tracking chambers are made up of planes with alternating anode and cathode wires grouped into modules of 2-3 wire planes. When a charged particle passes near one of the wires a signal is generated which can be used to determine its spatial location. The planes in each module are staggered to remove left-right ambiguity and each module is oriented at an angle to the others to give vectorial information. The tracking algorithm achieves about 90.5% efficiency reconstructing multiplicity-6 Monte Carlo events, and the chambers have single particle resolution of $\sim 150\mu m$. The time-of-flight (TOF) wall, placed 6.5 meters down from the target, consisted of 160 vertical plastic scintillator pickets with photomultiplier tubes at each end. The phototube signals are used to determine the charge of the particle, set the stop time, and supplement the tracking information of the drift chambers. The wall is estimated to have a timing resolution of $\sigma = 90ps$. The gas Cerenkov counter is segmented into 40 cells by aluminized mylar walls, each containing Freon-12 at 3.8 atmospheres with an index of refraction of n=1.0045. At the end of each light cell is an elliptical mirror that reflects the Cerenkov radiation to a photomultiplier tube. When a charged particle passes through the gas dielectric, it polarizes the medium along its path causing the gas to radiate like an elementary dipole. When the particle is travelling below the speed of light in the gas, the complete symmetry of the polarization field around the path causes the radiated wavelets to interfere destructively so that the distant intensity is zero. However, when the particle is travelling above the speed of light in the gas, the radiated wavelets can be in phase and create a coherent wavefront of Cerenkov radiation. The threshold velocity for the GasC is $\beta_{min} = 1/n = .99552$. The momentum threshold for $\pi^\pm$ firing the GasC is $p = 1.47$.

22

To solve the logistical problem posed by the large amounts of data produced, the data written to tape in each run was selected during run-time by a combination of triggers. These triggers could also be scaled down to keep a certain percentage of the triggering events. The trigger for a good beam was formed when the beam-evaluating scintillators agreed that the beam particle was the correct type, properly focused, and not immediately followed by another beam particle. Another scintillator downstream of the target on the beam axis measures the charge of collision fragments. If the beam is triggered, and this post-collision scintillator reveals a charge loss, it is assumed there was an inelastic interaction with the target and the INT1 trigger is set true. The detection of an inelastic interaction by measuring the fragment charge is limited to only interactions in which the nuclei lost at least one proton. The SPEC trigger is often set along with the INT1 trigger because it indicates when a particle has passed through the spectrometer based on signals from the trigger chambers and the TOF wall. A LVL2 trigger offered greater selectivity by only keeping events which had identified particles that were considered interesting. In the case of E859, there was an interest in events which produced strangeness, and so rare events in which kaons were detected were exclusively kept in some runs. The study being made here does not consider those kaon triggered runs at spectrometer angles of 14°, 24°, 34° and 44°. It is expected that there would be some bias in the results because the $e^{\pm}$ being observed in that subset of runs were produced in peculiar collisions. The remaining unbiased triggers were NOPID, $K^{+}K^{-}$ Veto Out, K^{+} Veto Out and K^{-} Veto Out. In addition to these triggers, the yield calculations required that the SPEC trigger was set. In the NOPID runs the particle identification was turned off and in the Veto Out runs the LVL2 trigger's veto of the SPEC or INT1 trigger was turned off. At 5° all runs that triggered on $K^{+}K^{-}$, K^{+} or K^{-} were used, except that only those events that set the INT1 trigger were kept. This was necessary at 5° because there were no NOPID or Veto Out runs. It was assumed that the requirement of an INT1 event reduced the bias to being negligible.

Chapter 3

Analysis of Gas Cerenkov Counter

Momentum and velocity information is sufficient for distinguishing $e^{\pm}$ from $\pi^{\pm}$ at momenta below about .5 GeV/c. At .2 GeV/c, the lowest momenta for which there is data, the $e^{\pm}$ have an energy 400 times their rest mass and so their velocities are close enough to the speed of light to be indistinguishable from it with the experimental detectors. The relation for the useful quantity $\beta^{-1} = c/v$ is

$$\beta^{-1} = (1 + (m_o/p)^2)^{1/2} = E/p$$

where m_o is the particle rest mass and c=1. The $e^{\pm}$ with momentum .2 GeV/c have a $\beta^{-1} = 1.000003$. As particle momenta increase, the $\pi^{\pm}$ velocity approaches the $e^{\pm}$ velocity and detector velocity resolution becomes an important factor. The velocity resolution depends on the time-of-flight resolution, which has been estimated to be between 90 and 120 ps. The particle β^{-1} distribution at a specific momentum spreads out into a gaussian peak with a broad tail. The approximate β^{-1} sigma of the $e^{\pm}$ gaussian is .0047, and for the $\pi^{\pm}$ above .5 GeV/c it is about .006. Above .5 GeV/c the distributions of $\pi^{\pm}$ begin to overlap with the $e^{\pm}$ so that both particles are no longer distinguishable by momentum and velocity information alone. The $\pi^{\pm}$ β^{-1} distribution overlaps progressively more with the $e^{\pm}$ β^{-1} distribution with increasing momentum. To further resolve the two particles, a gas Cerenkov detector (GasC) is employed. Beginning well below .5 GeV/c, $e^{\pm}$ that traverse the detector emit

Momentum Bin (GeV/c)	e^- Mean	e^- Sigma	e^+ Mean	e^+ Sigma
.2 - .3	1.0005(1)	.0046(1)	1.0002(1)	.0045(2)
.3 - .4	1.0007(1)	.0048(1)	1.0006(1)	.0047(1)
.4 - .5	1.0002(1)	.0044(1)	1.0001(1)	.0047(1)
.5 - .6	1.0004(1)	.0046(1)	1.0002(1)	.0047(1)

Table 3.1: Measurements of TOF calibration and uncertainty from gaussian fits to $e^\pm$ from .2-.6 GeV/c.

Cerenkov radiation. The pinp momentum threshold for emitting Cerenkov radiation is 1.47 GeV/c. Thus, the GasC detector allows the β^{-1} distribution of $e^\pm$ and pinp to be further resolved in the .5-1.47 GeV/c range. There are three unique regions in the 2-D plot of particle momentum vs. β^{-1}, called the PID (Particle IDentification) plot (figure 3-1). There is the region in which electrons can still be identified by momentum and β^{-1} alone because the pion distribution does not overlap. Call this the region of TOF-ID electrons. Similarly there is the region of TOF-ID pions. Above .5375 GeV/c in both TOF-ID regions, the GasC is checked even though it isn't necessary, to further verify the particle identification. In the third region where the electron and pion distributions overlap the GasC information is crucial. It makes the final decision concerning particle identification in what will be called the overlap region.

Calibration of particle time-of-flight was checked using $e^\pm$ in the momentum range of .2-.6 GeV/c. Using momentum slices of .1 GeV/c and a β^{-1} binsize of .001, the $e^\pm$ slices were fit with gaussians and their means recorded in table 3.1.

To utilize the GasC information in the overlap region, it was useful to first approximately determine the GasC detector's efficiency. The TOF-ID electron region was used to estimate the GasC detector's inefficiency. Recognizing that all the electrons in this region should fire the GasC, an analysis of the percentage of particles that did not fire the GasC should represent an estimate of the inefficiency. To accomplish this the data was separated into three categories according to whether the particle fired the GasC, did not fire the GasC, or was out of the GasC's angular range. Each data set was sliced into momentum bins of .1 GeV/c to observe any correlation between inefficiency and momentum. The number of particles that did not fire was divided
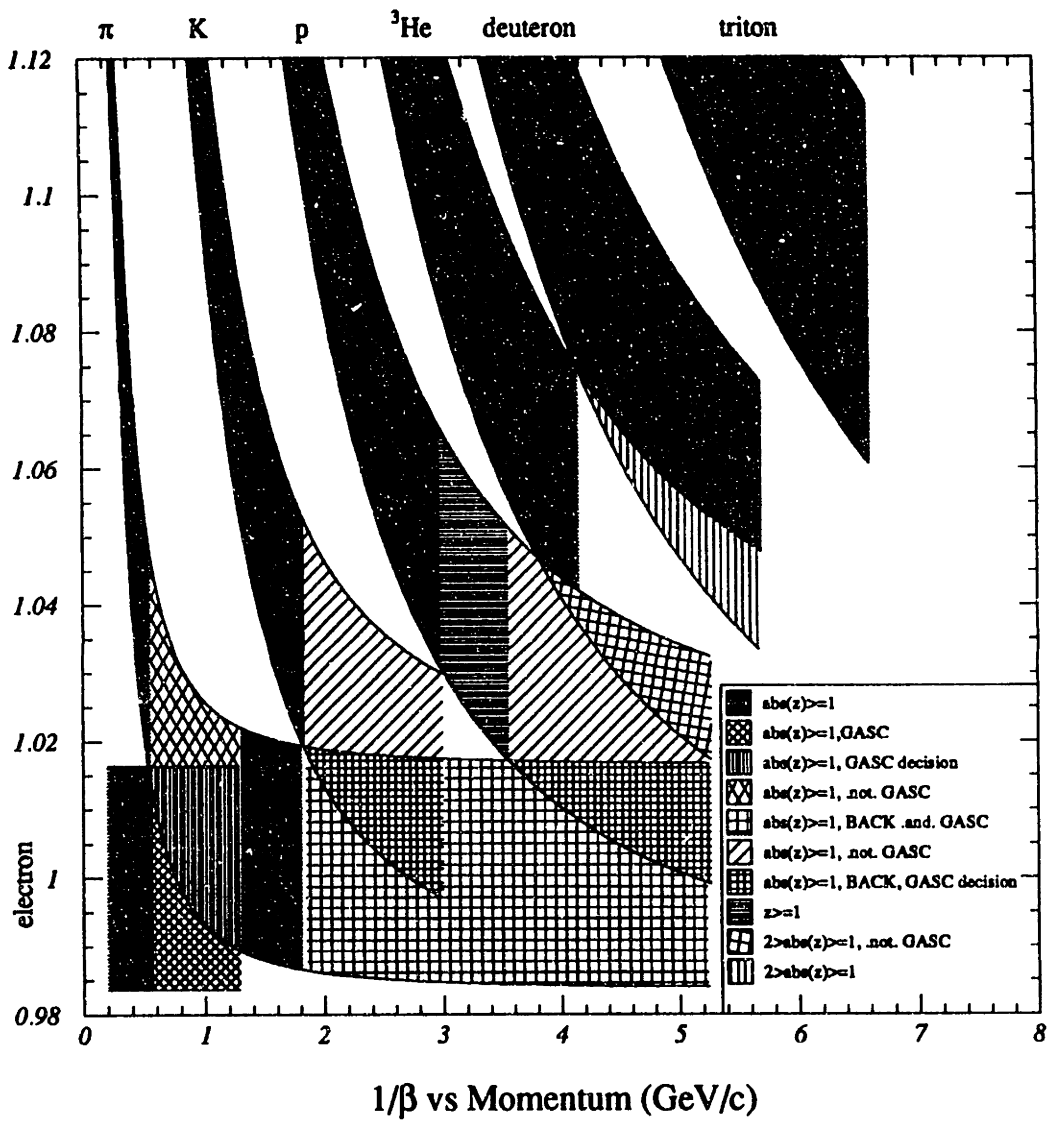
Figure 3-1: Particle IDentification (PID) plot

27

Spectrometer Angle	Inefficiency
5	3%
14	4%
24	4%
34	4%
44	4%

Table 3.2: Inefficiency of the gas Cerenkov counter, based on percentage of .2-.4 GeV/c electrons and positrons that did not fire it.

by the number of particles that did fire and the results for .2-.8 GeV/c are shown in figure 3-2 for each spectrometer angle. The apparently sharp increase in inefficiency at .5 GeV/c at all angles is due to the leakage of muons and pions that did not fire the GasC into the $e^{\pm}$ TOF-ID region. The 2-D PID plot for TOF-ID $e^{\pm}$ that did not fire the GasC shows the increase to be predominantly due to particles observed along the border with the overlap region (figures in Appendix B). The muons are lighter than the pions so they begin to overlap with the electrons at the lower momentum of about .4 GeV/c (figure 3-3). A closer examination of the muons and pions leaking into the electron TOF-ID region at 14° as the momentum increases is shown in figures 3-4 and 3-5. The .3-.4 GeV/c momentum slice depicts most clearly the shoulder on the pion peak that has not yet leaked into the electron TOF-ID region. It is also apparent in this momentum slice that the distribution of particles not firing the GasC detector in the TOF-ID electron region has a symmetrical shape similar to that of the identified electrons that fired the GasC. Beyond .4 GeV/c, the distribution of inefficient par- ticles in the TOF-ID electron region takes on an asymmetry due to first the muons and then the pions leaking into it.

The muons and pions are behaving as they should by not firing the GasC, so the true Gasc inefficiency was based on the mostly uncontaminated data from .2- .4 GeV/c. The percentage inefficiency values used in the cross-section analysis are recorded in table 3.2.

The data from the TOF-ID pions region was also separated according to GasC response and sliced into .1 GeV/c bins to estimate the GasC overefficiency. The
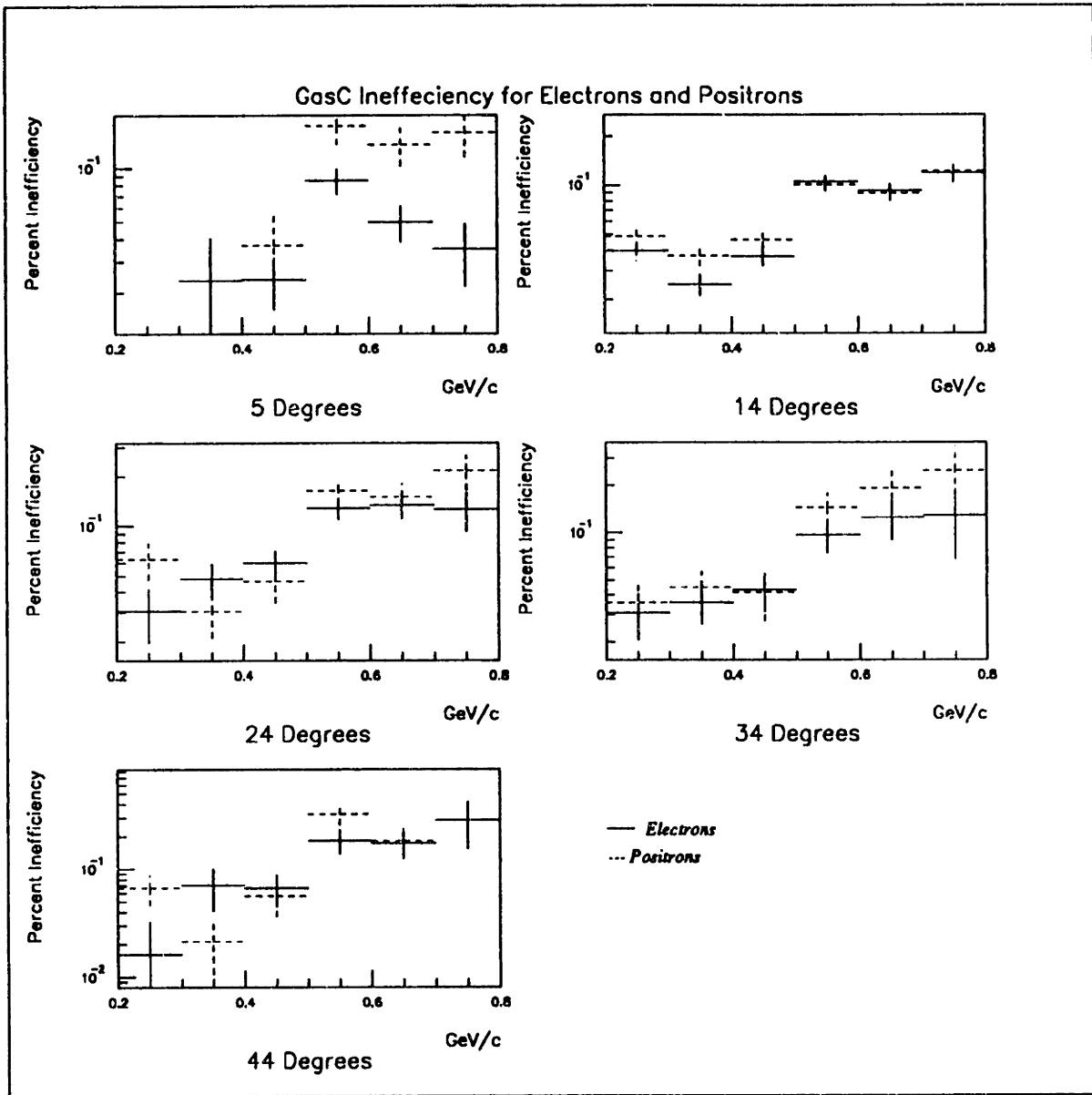
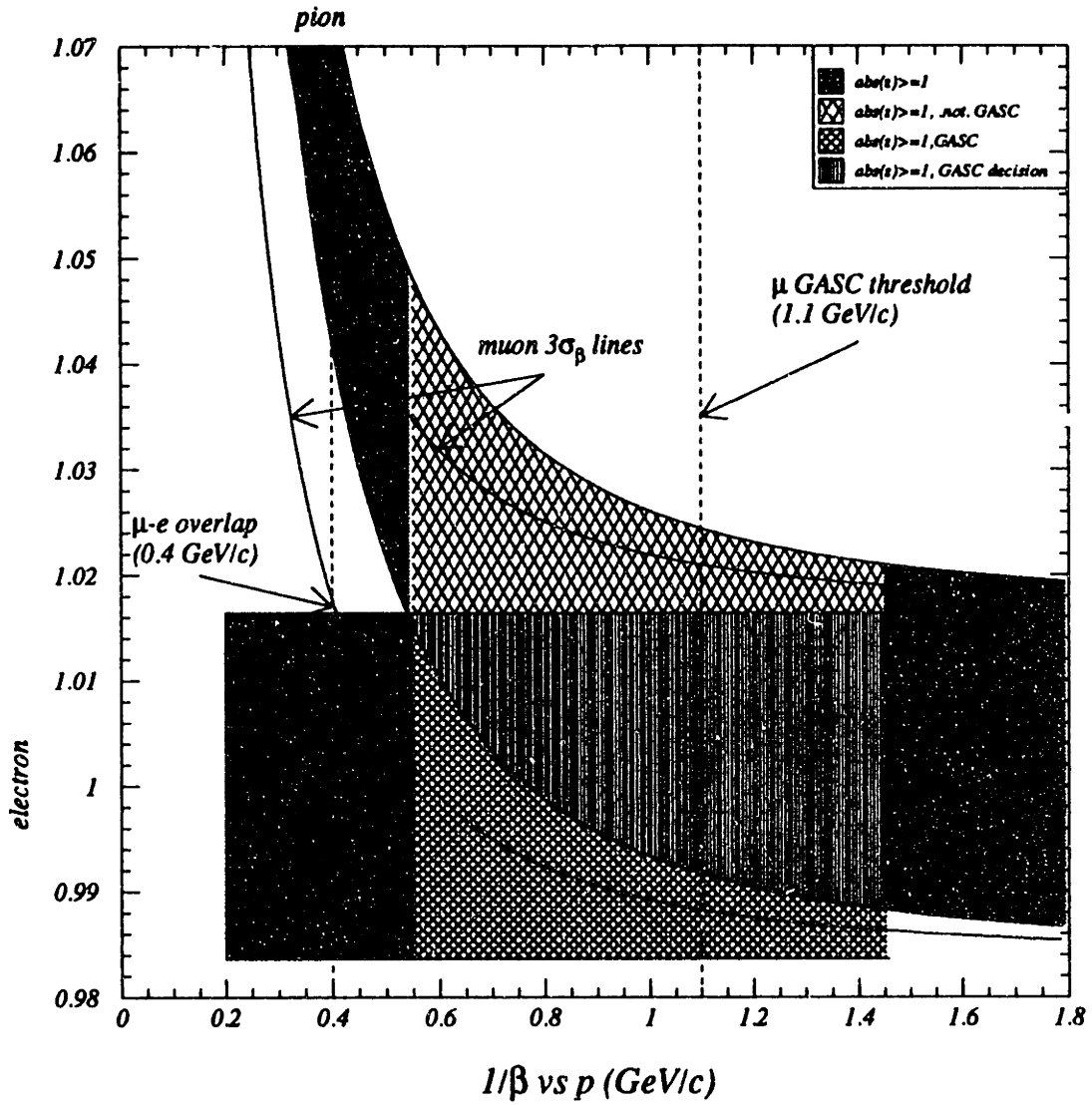Figure 3-2: Gas Cerenkov Counter Ineffeciency for Electrons and Positrons with momenta between .2-.9 GeV/c.

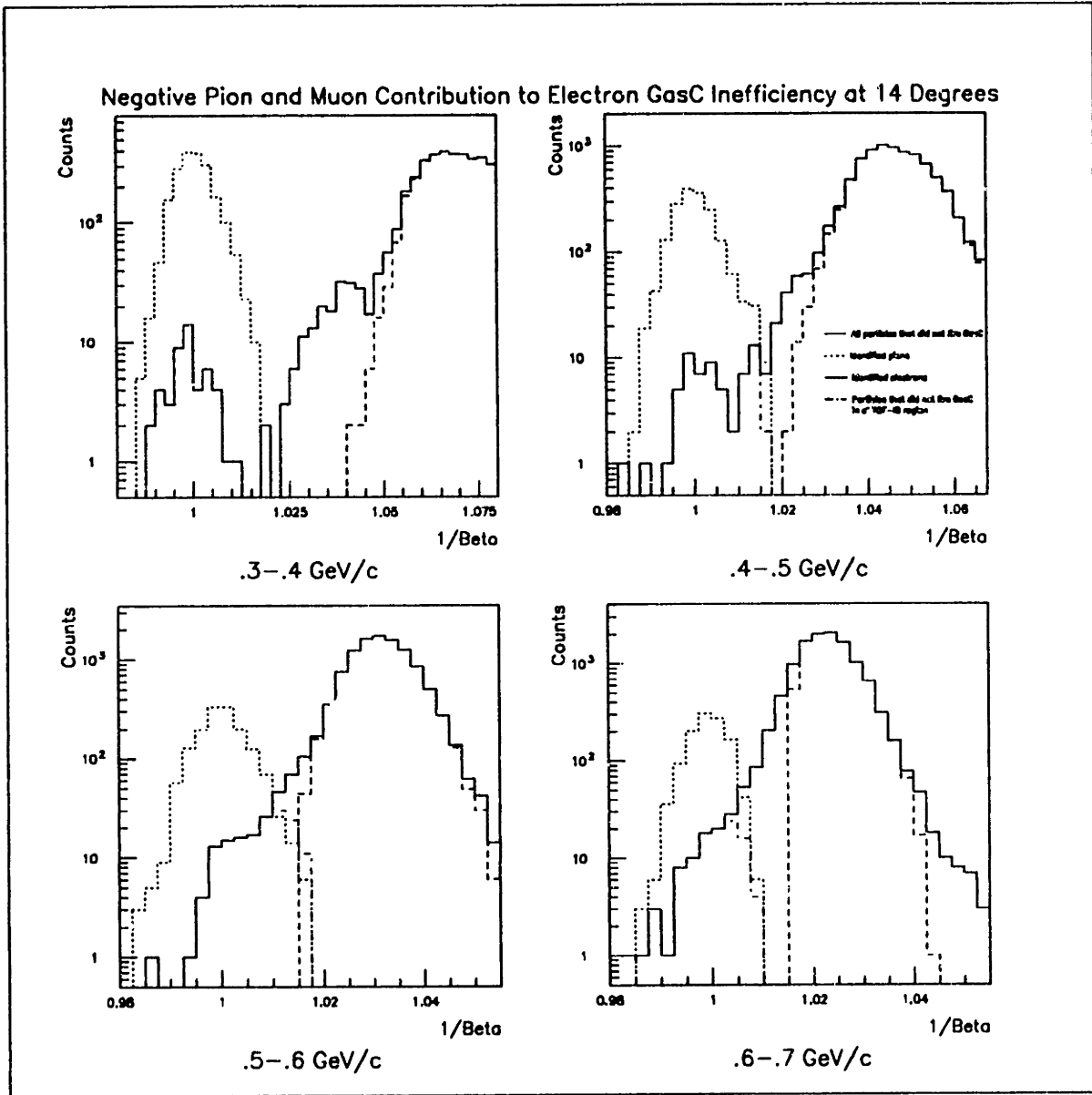Figure 3-3: Particle IDentification (PID) plot for Region with Intersecton of Electons, Muons and Pions.

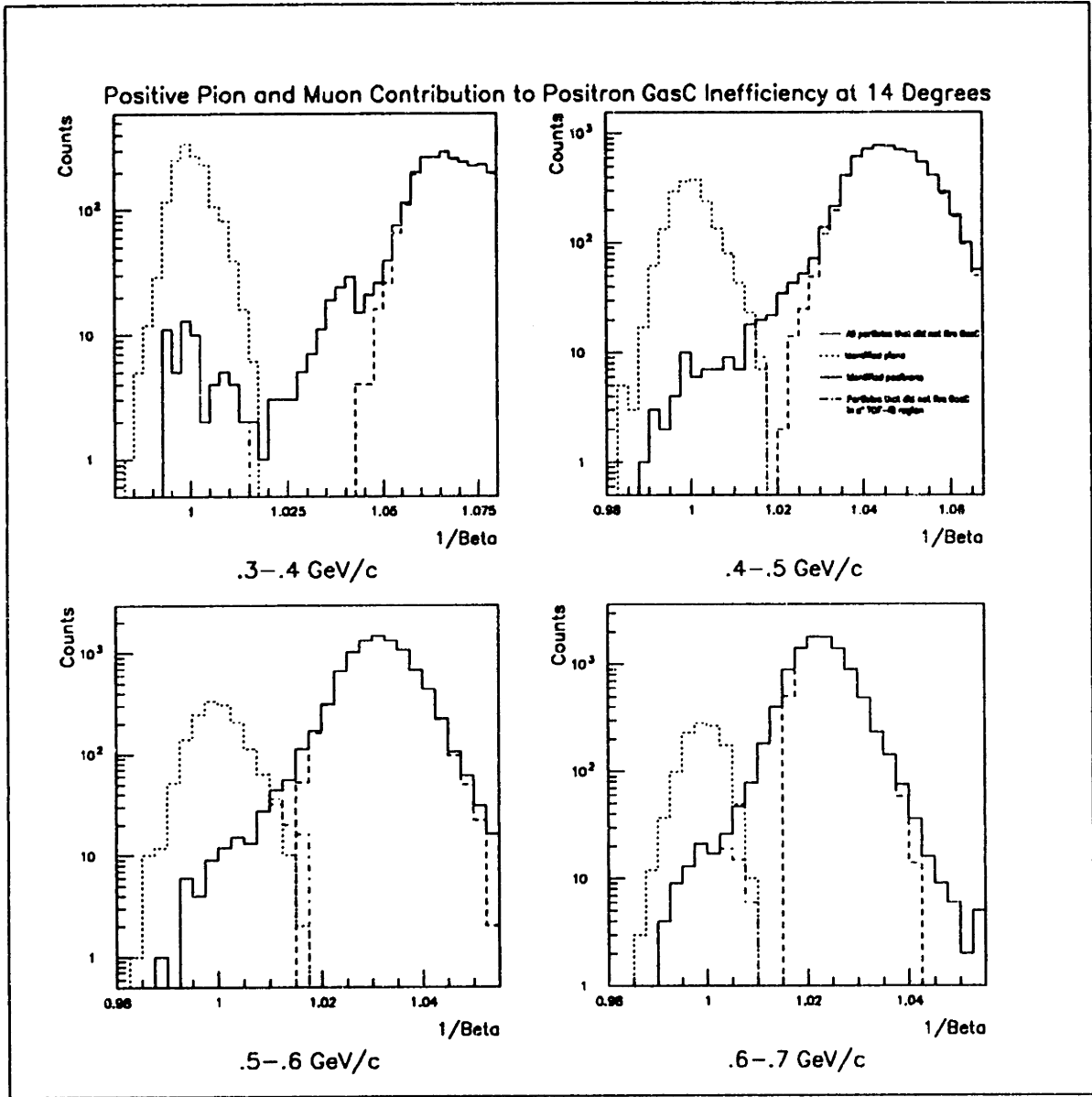Figure 3-4: Leakage of Negative Pions and Muons into Electrons at 14°

31

Figure 3-5: Leakage of Positive Pions and Muons into Positrons at 14°

Spectrometer Angle	Overefficiency
5	8%
14	5%
24	3%
34	2.5%
44	2%

Table 3.3: Over-efficiency of the gas Cerekov counter, based on percentage of negative and positive pions that fired it.

number of particles that did fire was divided by the number that did not fire and the results are shown in figure 3-6.

Estimates of the overall over-efficiency at each angle are given in table 3.3. Above .9 GeV/c the statistics drop significantly because most of the pions are now in the overlap region. More significantly, the muons which are being included in the TOF-ID pions region begin to fire the GasC at 1.1 GeV/c. There is a corresponding steady rise in the GasC over-efficiency above this momentum.

To investigate the decrease in GasC overefficiency as the spectrometer angle increased, the tracks at each spectrometer angle were separated into two data sets according to the track angle. Each spectrometer angle setting has a range of about 14°, so the division was made 7° into the spectrometer. However, due to insufficient counts at each angle, no finer angular dependence was observed. From table 3.3, the over-efficiency decreased 3% from 5°-14°, 2% from 14°-24°, and .5% between 24°-34° and 34°-44°.

It turned out that a better indicator of the angular dependence of the overefficiency would be the position of the particle's hit on the TOF wall. The particles produced in a collision are focused primarily in the forward direction along the beam axis. By way of multiple collisions, these particles may be deflected or scatter other fast particles into the GasC detector. The probability for one of these stray particles firing the GasC at the same time as a legitimate particle that has passed through the spectrometer is increased on the beam side of the GasC. Looking at this angular dependence from the track angle loses the useful information because the magnet
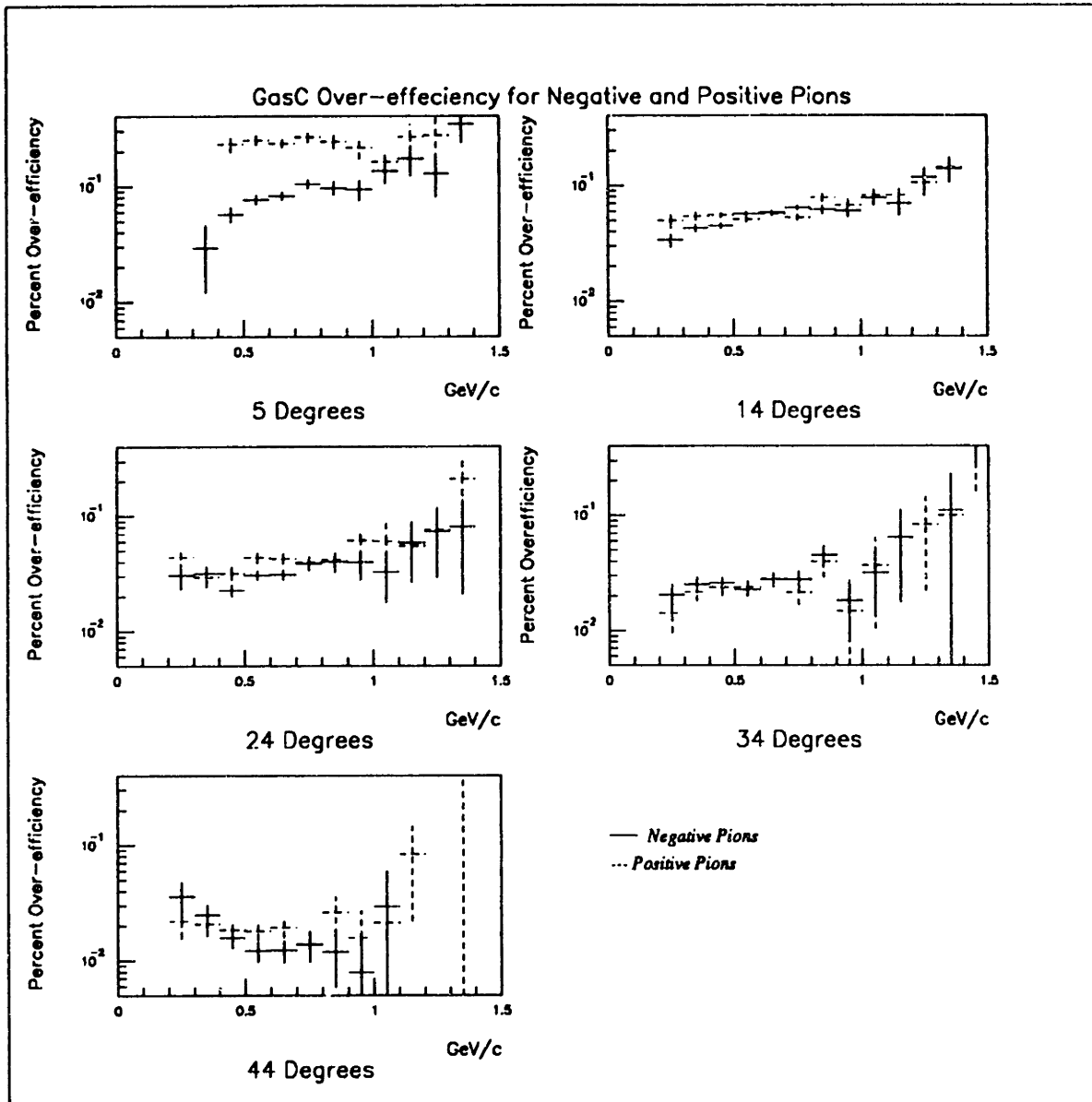
33

Figure 3-6: Gas Cerenkov Counter over-efficiency for pions with momenta from .2-1.5 GeV/c

bends the tracks according to charge. Where a track ends up in the GasC has as much to do with its charge and momentum as the track angle. But because the TOF wall is placed directly in front of the GasC, it is suitable for addressing the question of angular dependence. The data for pions with the spectrometer at 5° and 14° were divided into those particles that hit the outside half of the TOF wall and those that hit the beam side half. The over-efficiency shows a clear dependence on the region of the TOF wall the particle hit (figure 3-7).

If the distribution of particles across the GasC were uneven, it would make sense to weight the particles according to where they hit the TOF wall. The difference is quite dramatic at 5° the outside cells firing at about 8% over-efficiency while the beam-side cells fire at about 30% over-efficiency. At 14° the outside cells fire at about 4-5% over-efficiency and the beam-side cells at about 7%.

The overefficiency was also studied as a function of multiplicity at 14°. The events were divided into those with less than 3 tracks in the spectrometer and those with 3 or more tracks. The events with higher track multiplicity corresponded with a greater overefficiency. For the lower multiplicity events, the overefficiency at 14° was 4-5%. High multiplicity tracks resulted in overefficiencies of 5-8%. This suggests that some of the pions counted as firing the GasC are due to coincidence with other particles firing the GasC.
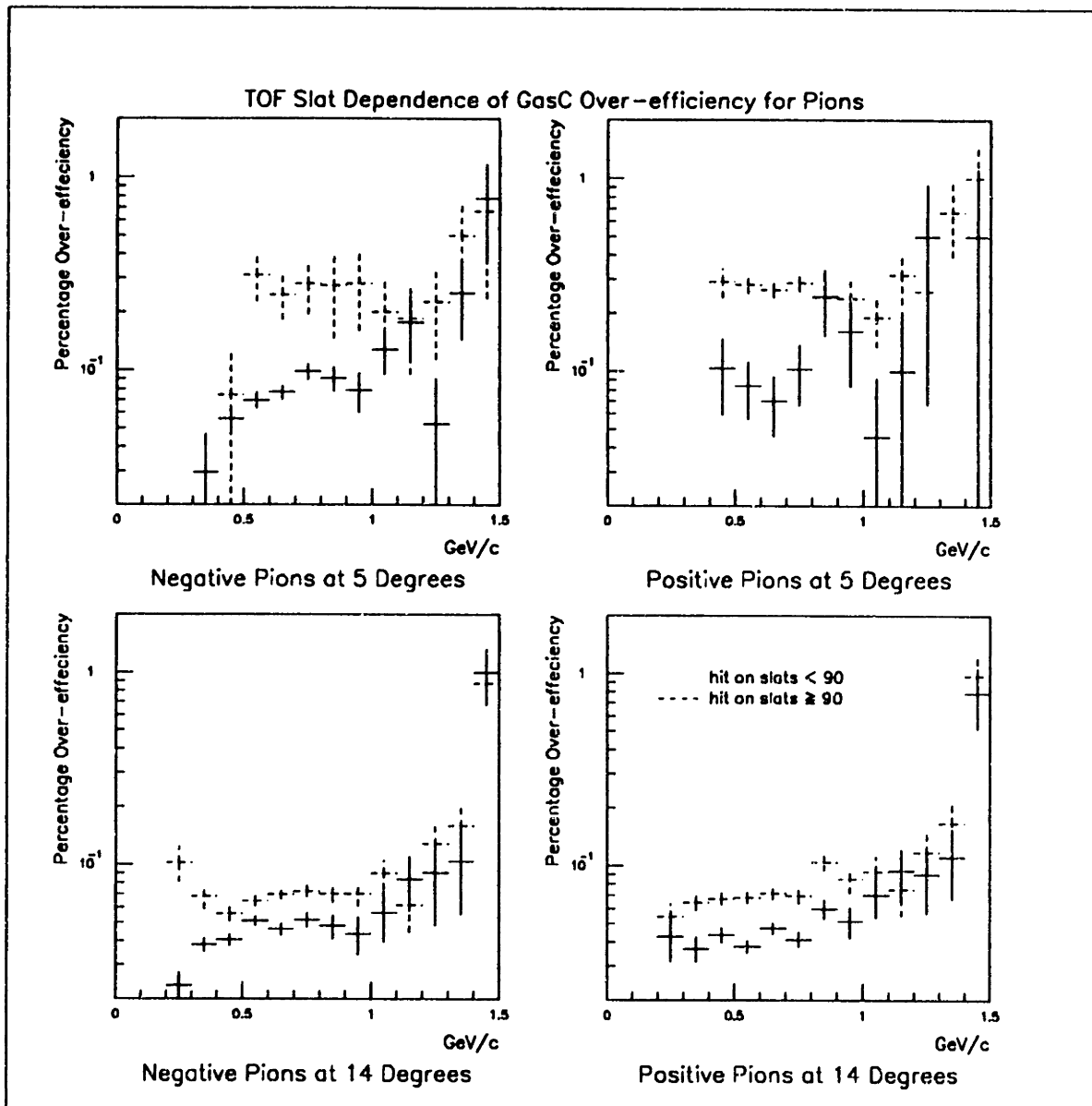
Figure 3-7: Dependence of GasC over-efficiency on TOF wall for pions with the spectrometer at 5° and 14°

Chapter 4

Analysis of Pion Contamination

Having obtained approximate values for the GasC detector efficiency, the next stage of analysis involved separating the electrons from the pions in the overlap region. While the GasC detector is useful for identifying most of the pions in this region, the overefficiency of the detector allows some of the pions to be confused as electrons. Because the pion counts are many times larger than the electron counts, the small percentage of pions that fire the GasC are a substantial contribution to the electrons in the overlap region. These fake electrons due to pion contamination increase with momentum for two reasons. First, as already noted, the higher momenta pions overlap more because their β^{-1} values approach those of the electrons. Second, the electron counts decrease more rapidly than the pion counts with increasing momentum. As a result, above 1.0 GeV/c the contaminating pions overlap the electrons almost completely and have about the same or more counts.

These pions cannot be distinguished from the electrons using the momentum, velocity and GasC information at this point. However, it is possible to recognize the gaussian forms of the electron and pion β^{-1} distributions. The pion contamination begins at $\sim$ .5 GeV/c where the β^{-1} distributions mingle, and increases as the distributions progressively converge until at $\sim$ 1.0 GeV/c the two peaks are indistinguishable. In this transitional momentum range the particle distributions are fit with gaussians and the contamination of the electron peak by the pion peak can be approximately determined.

This was the task of the next stage, which relied on two strategies. The general strategy was to fit a double gaussian to the electron and pion peaks allowing the amplitude, mean and sigma parameters of both peaks to be adjusted for a best fit. When this failed, the alternative strategy was to allow only the amplitudes to vary, fix the means to their calculated values, and fix the sigmas to values determined by successful fits of the general strategy.

The double gaussian fits were performed on electrons and pions that fired the GasC detector in the .4-1.0 GeV/c momentum range. The data was sliced into .1 GeV/c momentum bins. This was determined to be wide enough to insure sufficiently high statistics for good fits and narrow enough to minimize broadening of the gaussian peaks. The approximately gaussian distributions in each slice result from a convolution of a continuum of gaussians with β^{-1} mean values determined by the momentum range of the slice and Equation 1. Fortunately, the significant pion contamination occurs at higher momenta where the broadening effect becomes negligible. For each slice the data was binned in .002 β^{-1} bins, giving sufficient statistics and good gaussian peaks for all angles except 44°.

The criterion for a good fit was based on qualitative agreement between the fit and the data. The good fits were further verified by agreement between the fitted means and the calculated means, the fitted sigmas and the average sigma, as well as the computed area under the gaussian fits and the sum of the fitted bin contents.

Fits made with the general strategy were successful up to .8 GeV/c for all angles except 44°. The fits for .8-.9 GeV/c slices succeeded for positive and negative particles at 5°. They also succeeded for negative particles at 14°, positive particles at 24°, and positive particles at 34°. The general strategy would not converge properly for the .9-1.0 GeV/c slices because the peaks were too close. At 44° the counts were so low that the positive fits failed to give reasonable sigma values and the negative fits varied dramatically.

The electron means for the good fits were all within $\sim$ .001 of the calculated value of 1.000. The pion means varied between .001-.002 away from the calculated means. The electron sigmas ranged between about .004-.0055 and averaged about .0045. The

Momentum Slice	Momentum Center	β^{-1} Mean	$\Delta\beta^{-1}$
.4-.5	.45	1.047	.021
.5-.6	.55	1.032	.012
.6-.7	.65	1.023	.007
.7-.8	.75	1.017	.005
.8-.9	.85	1.013	.003
.9-1.0	.95	1.011	.002

Table 4.1: The Pion β^{-1} mean values used by the amplitude gaussian fits as determined by the center of the momentum bin.

pion sigmas ranged between about .0042-.008 and averaged about .006.

The alternative strategy was applied to the 44° slices, the bad .8-.9 GeV/c slices, and the .9-1.0 GeV/c slices. The β^{-1} values for the means were calculated based on the momentum at the center of each slice. Table 4.1 lists the β^{-1} means along with the range of β^{-1} values over the slice responsible for gaussian broadening. For the electron gaussians the sigma used was .0045 and for the pion gaussians the sigma was .006. The .8-.9 GeV/c alternate fits at 14°, 24°, and 34° were good. The 44° alternate fits were good up to .8 GeV/c. The low counts of the higher 44° momentum slices made a good fit difficult given the variation in counts from bin to bin, but the resulting fits were acceptable. The .9-1.0 GeV/c fits were also difficult to judge but seemed reasonable.

With the amplitudes, means, and sigmas of the double gaussian fits in hand, contamination of the electrons by pions that fired the GasC could be determined. To do this, it was necessary to establish more precisely the boundaries on the PID plot of the region in which a particle is called an electron. The low end of the momentum range is simply determined by the acceptance of the spectrometer. Electrons are produced in reasonable quantities at momenta below .2 GeV/c but they are deflected out of the spectrometer when passing through the magnet. The high end of the momentum range would be at 1.47 GeV/c, the momentum threshold for pions firing the GasC. However, analysis has shown that pion contamination makes electron data above roughly 1.0 GeV/c unreliable. It was noted previously that the β^{-1} borders

of the electron region were determined by the TOF uncertainty. The PID code that identifies the particles uses the 3σ of the TOF and momentum uncertainty to determine the acceptable range for particle identification. This value may vary depending on the TOF slat that the particle hit, since several slats have a larger uncertainty than the others. The TOF uncertainty also seems to have some slight momentum dependence. The lower β^{-1} border of .98 is unambiguous because there are no overlapping particles to confuse with the electrons. The upper β^{-1} border required some analysis because the value was calculated by the particle identification code.

It was known that particles on the pion side of the β^{-1} border which did not fire the GasC would be called pions by the particle ID code, whereas particles on the electron side of the border which did not fire the GasC would not be given a good particle ID status. Therefore, the $14°$ data was binned with .0001 β^{-1} bins and particles which did not fire the GasC and were called pions were looked at in detail along the electron-pion border. The particles called pions by the code were found down to the 1.0159 bin edge. A value of 1.016 was used for the β^{-1} border because the .0001 difference would be completely insignificant in the pion contamination analysis, which used a .002 bin size. Also, the exact value of the border seemed to change slightly with momentum, as indicated by analysis of particles which did fire the GasC and were called electrons. While the pions extended down to 1.0159 at .6-.7 GeV/c, the electrons extended up to 1.0167 at .2-.3 GeV/c and up to 1.0162 at .5-.6 GeV/c. There were too few counts along the disputed border region to obtain a better value than 1.016, and no sufficient reason for needing a more precise or momentum dependent value.

The β^{-1} border was used to observe the agreement between the total number of electrons and pions in the electron region as computed by the area under the gaussian fits and by a summation of the actual bin counts. The relevant area under the gaussians in each momentum slice was in the β^{-1} range from .98-1.016. The electron gaussian area was computed using the analytic expression for the integral of a gaussian from $-\infty$ to ∞:

$$amp \int_{-\infty}^{\infty} e^{-\frac{1}{2}(\frac{x-mean}{sigma})^2} = \frac{amp\sqrt{2\pi}\,sigma}{binsize}.$$

Momentum Slice:	.5-.6	.6-.7	.7-.8	.8-.9	.9-1.0
5°	.04	5.7	24.5	39.5	48.1
14°	.16	7.1	29.8	41.6	45.7
24°	.38	8.6	17.8	31.9	44.1
34°	.67	2.5	18.6	50.5	53.8
44°	.10	4.5	17.7	57.6	42.4

Table 4.2: Percentage values for contamination of electrons by negative pions from .5-1.0 GeV/c.

The area under the electron gaussian tails extending beyond the β^{-1} borders was insignificant. The pion gaussian area in the electron region was computed using the error function in the CERN program library. The function was defined as

$$freq(x) = \frac{1}{\sqrt{2\pi}} \int_{-\infty}^{x} e^{(\frac{-t^2}{2})} dt$$

and was computed by rational Chebyshev approximation. The function integrates up to x for a gaussian with mean equal to zero and sigma equal to one. Setting $x = \frac{1.016 - mean}{sigma}$ resulted in an integration from $-\infty$ to 1.016 for each pion gaussian. This was considered to be the number of pions that were being identified as electrons by the PID code. To determine the fractional percentage of pion contamination in the PID-identified electrons, this value for the number of pions was divided by its sum with the number of electrons given by the electron gaussian.

The electron and pion counts from the gaussian fits are plotted on top of the counts from the bin summation and the Poisson errors associated with the bin totals. They are shown in Appendix G. The agreement is generally good, the gaussian totals falling within error of the bin totals, even for the bad fits.

It was straightforward to extract the pion contamination from the electron and pion gaussian counts. The number of pions in the electron region was divided by the sum of the electrons and pions. The resulting pion contamination percentages used for further analysis are shown in table 4.2 and table 4.3.

Inspired by the results from the pion over-efficiency dependence on TOF wall

41

Momentum Slice:	.5-.6	.6-.7	.8-.9	.9-1.0	
5°	1.7	15.2	48.3	63.8	65.2
14°	.35	10.2	24.2	41.6	42.6
24°	.26	6.8	30.3	39.3	53.3
34°	.05	6.1	32.1	30.7	33.7
44°	.11	4.6	16.9	65.0	45.3

Table 4.3: Percentage values for contamination of positrons by positive pions from .5-1.0 GeV/c.

slats, the pion contamination was subjected to the same examination. The 5° data was divided according to whether the particle hit the outside half of the TOF wall or the beam-side half of the TOF wall. Better statistics at 14° allowed for the same analysis with the TOF wall divided into thirds. The results are show in figure 4-1. As with the pion over-efficiency, the 5° data shows a greater disparity in the effect of the position of hit on the TOF wall on contamination.
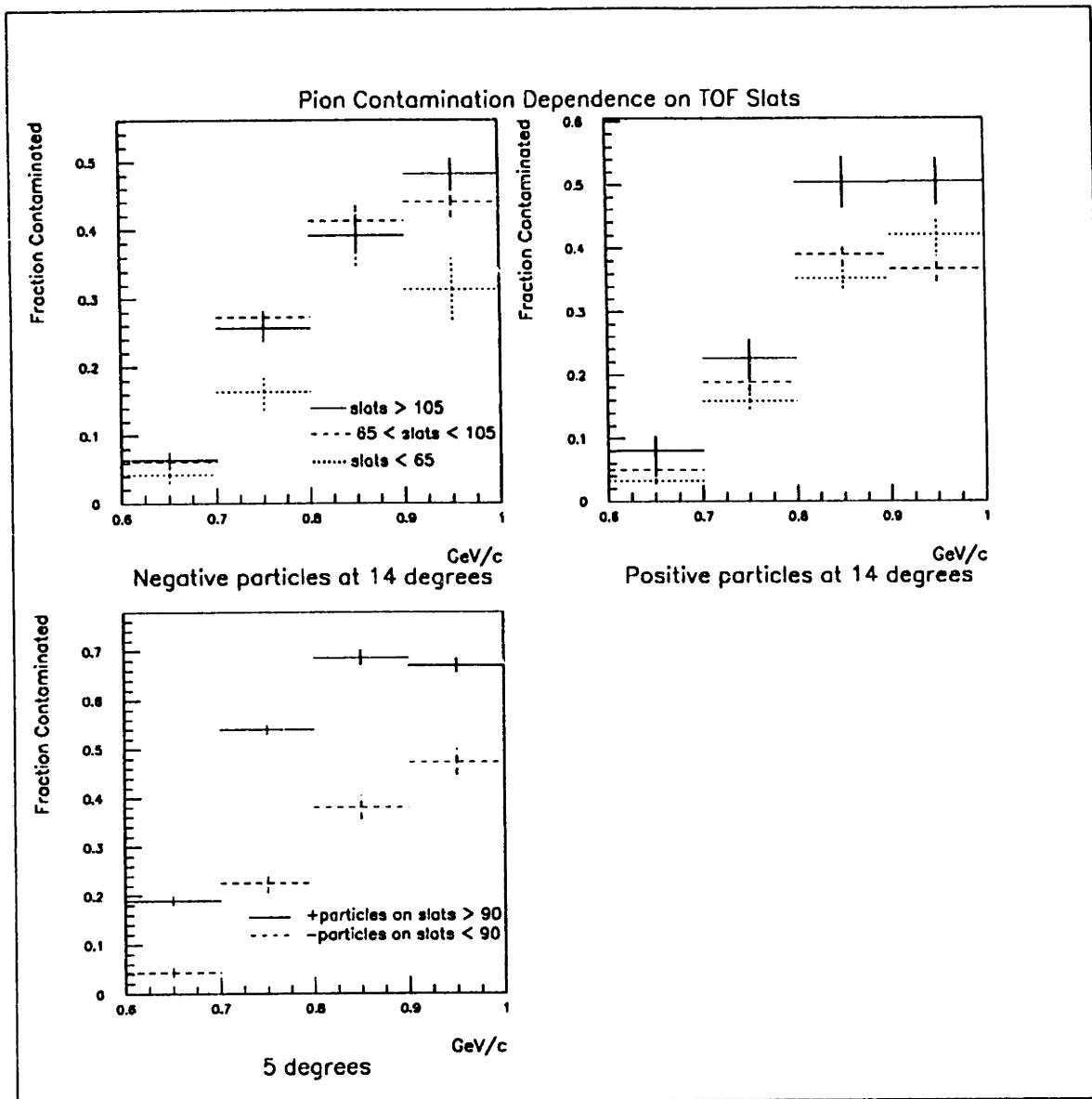
Figure 4-1: Dependence of pion contamination of electrons on TOF wall hits at 5°
and 14°

Chapter 5

Invariant Cross Sections and Yields

Cross sections and yields can be created for different combinations of trigger types and event selections depending on what particle production scenarios are of interest. The combinations used in this analysis were chosen to produce inelastic yields with a minimum bias. Minimum bias events are of interest because they represent those events with the least constraints on the nucleus-nucleus system. If the events chosen were required to have a multiplicity beyond a certain threshold, this would bias the data towards high-multiplicity production mechanisms that affect the particle yields.

The kinematic variables used in the cross-section analysis are total momentum p, track angle θ, rapidity y, and transverse mass m_t. The total momentum and track angle together form a phase space (p, θ) that readily corresponds to the experimental geometry. The track angle is defined as the angle between the particle track as it leaves the collision and the beam axis. The total momentum is along the track, and may be decomposed into $p_\parallel$ along the beam axis, and $p_\perp$ perpendicular to the beam axis. However, because of the high energies involved in the collisions, switching between the target, center-of-mass, or projectile frame would require transformations of $p_\parallel$ that make it less useful for characterising the invariant properties of the particles. The relativistic analog of velocity is called rapidity and its Lorentz invariance makes

45

it the variable of choice. It is defined as

$$y = \frac{1}{2} ln \frac{E + p_{\parallel}}{E - p_{\parallel}} = tanh^{-1} \beta_{\parallel}$$

where $\beta_{\parallel}$ is the longitudinal velocity.

The Galilean transformations that boost rapidity along the beam axis preserve the shape of the rapidity distribution because only an additive constant is required. The constant is the rapidity of the boosted frame with respect to the unboosted frame. The rapidity forms a useful phase space with the transverse mass (y, m_t). The transverse mass characterizes perpendicular distributions, and is defined as

$$m_t = \sqrt{p_{\perp}^2 + m_o^2}$$

where m_o is the particle rest mass. If the rest mass is subtracted from m_t, then it is called the transverse kinetic energy. In the case of $e^{\pm}$ the difference between them is negligible. The (y, m_t) space is popular because it has displayed exponential behavior for broad rapidity and transverse mass ranges. Exponential distributions are expected from thermalized systems, a feature called m_t scaling. The electrons are plotted to make similar exponential fits and look at the dependence of the slopes on rapidity.

What is plotted in the phase spaces are differential yields and total yields. The differential yield, d^3n/dp^3, is the number of particles of a certain type falling in a discrete bin in momentum space per event. The differential yield will vary depending on the event type chosen and where the bin is in momentum space. The total yield is calculated by integrating the differential yield over all momentum space:

$$n = \int \frac{d^3n}{dp^3} d^3p.$$

The average yield per event is obtained from an ensemble of N events, appropriately normalized. For example, the set of NOPID and Veto Out runs analysed comprise a large set of differently characterised events. The set of all SPEC events

represent a fraction of that large set. Calculations based on the set of SPEC events, normalized by the number of beam events, lead to values for the differential and total yield. The differential yield is usually seen in its Lorentz invariant forms, with the dependence on the azimuthal angle averaged out over many symmetric collisions:

$$dn(y, m_t) = \frac{d^2n}{2\pi m_\perp dm_\perp dy}$$

and

$$dn(p, \theta) = \frac{d^2n}{2\pi p^2 sin\theta dp d\theta}.$$

Having decided which run triggers and event types are appropriate, the histograms required to produce the cross sections and yields can be filled. For each run that meets the trigger criteria, the events are looped over one by one. For events of the correct type, the particles are binned in their own histograms in the chosen phase space as raw counts measured by the spectrometer. It is then necessary to apply weights to the raw counts based on extrapolations to how many actual counts were produced for each count measured. The number of particles captured by the spectrometer's angular acceptance and then identified determines the raw yields within that angular acceptance. But these particles represent only a surviving fraction of the total number of particles that were emitted within the spectrometer's angular acceptance. The actual yields evolve into these raw yields from the collision event to data tape according to the fortunes of the particles in the experimental environment. To reproduce the actual yields requires determining the effects of these fortunes on the particle populations. They include multiple scattering and absorption in the spectrometer material, detector inefficiencies and particle decays. These effects are bound up into the probability that a particle headed for the spectrometer will have its track reconstructed and be properly identified. These values are in practice determined only as a function of momentum, and then used to weight the raw yields. The results presented here are based on weights obtained by David Morrison, except for the additional correction based on the GasC efficiency. Dave investigated the efficiency for capturing and identifying a particle by running an ensemble of single-particle events in a Monte-Carlo simulation

47

of the E859 experiment. Peter Rothschild's results for reconstruction efficiency as a function of multiplicity are also used. The pion reconstructions are further disabled by decays, which obey the exponential decay law:

$$N = N_o exp(-\frac{t}{\gamma\tau}) = N_o exp(-\frac{L}{\beta\gamma c\tau}) = N_o exp(-\frac{Lm_o}{pc\tau}).$$

L is the particle's path length, p the momentum, m_o the rest mass, and τ the particle lifetime. For pions, $c\tau = 780$ cm. From 1.0 GeV/c down to .5 GeV/c, the calculated percentage of pions that survive to the TOF wall drops from about 90% to about 80%.

The spectrometer acceptance accounts for the border between the regions in phase space where if a particle lands in a bin it is either definitely in the spectrometer or it is not. In any one of the border bins there will be a certain fraction of particles that make it into the edge of the spectrometer, and the rest will just barely escape it. The counts that are collected in that bin are weighted to make up for the lost fraction of particles. The most significant weighting factor in the acceptance is due to the azimuthal ϕ acceptance. The ϕ acceptance affects the weight of a θ bin because as the spectrometer moves away from the beam line which defines the z-axis of the coordinate system, the ϕ acceptance decreases.

The yields are divided into positive and negative particles. For each particle sign, there are Au 1% yields which include 5° and 14° runs, and there are Au 3% yields which include 14°, 24°, 34° and 44° runs.

In figures 5-1 to 5-4 the differential yields are plotted in (p,θ) space for the Au 1% target. Each symbol type corresponds to a slice in θ of 10°. For each increasing angle slice, the differential yields are scaled down by a factor of 10 so that they are not plotted on top of one another. For each particle type, the decrease in yields with increasing momentum can be observed, but the $e^{\pm}$ yields seem to fall off faster than the pions with increasing momentum.

In figures 5-5 to 5-8 the differential yields are plotted for the Au 3% target. These can be compared to the results of a preliminary investigation made using the Geant
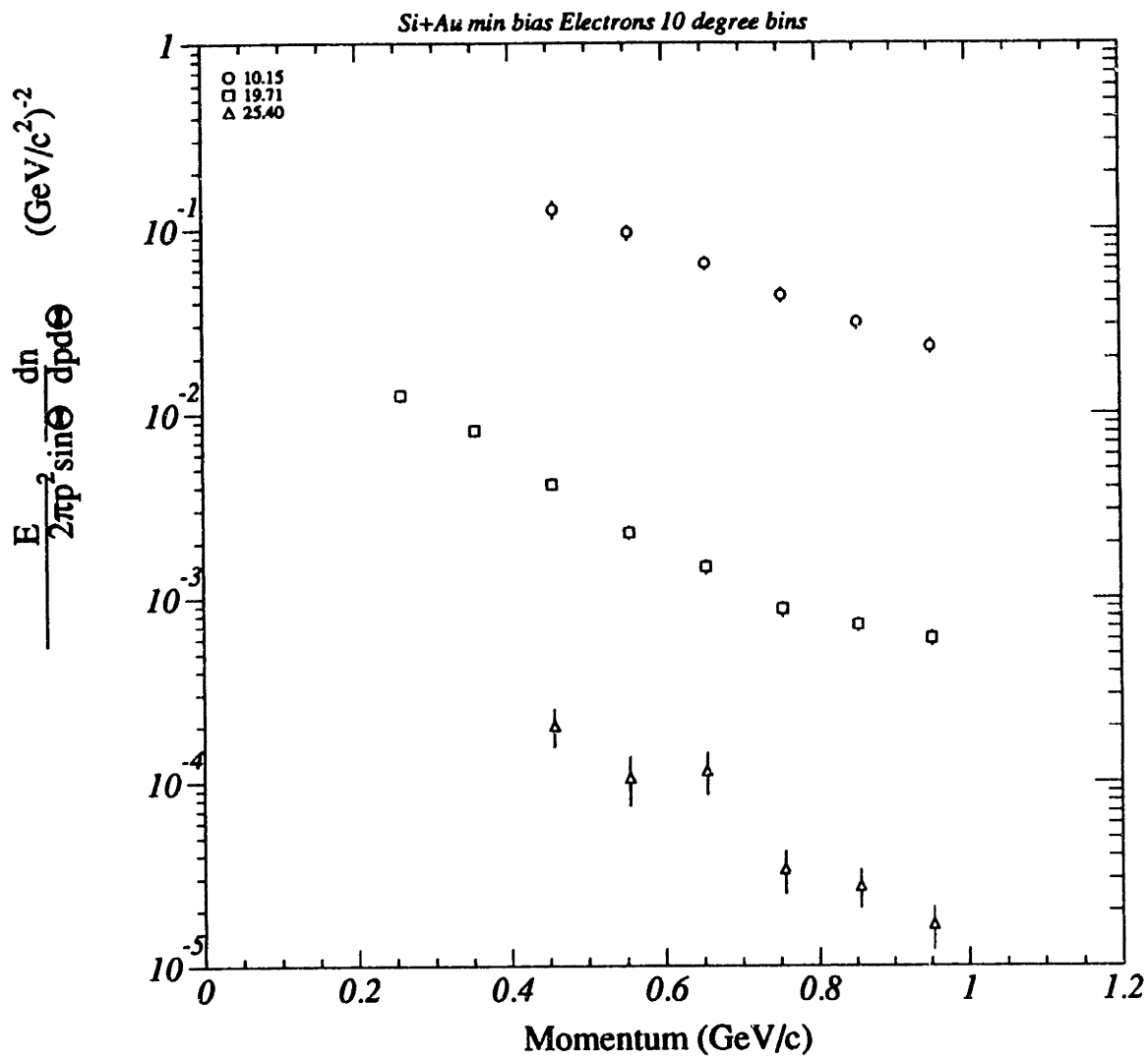
Figure 5-1: Differential Yields in (p, θ) for Electrons with Au 1% target and 5° and 14° settings
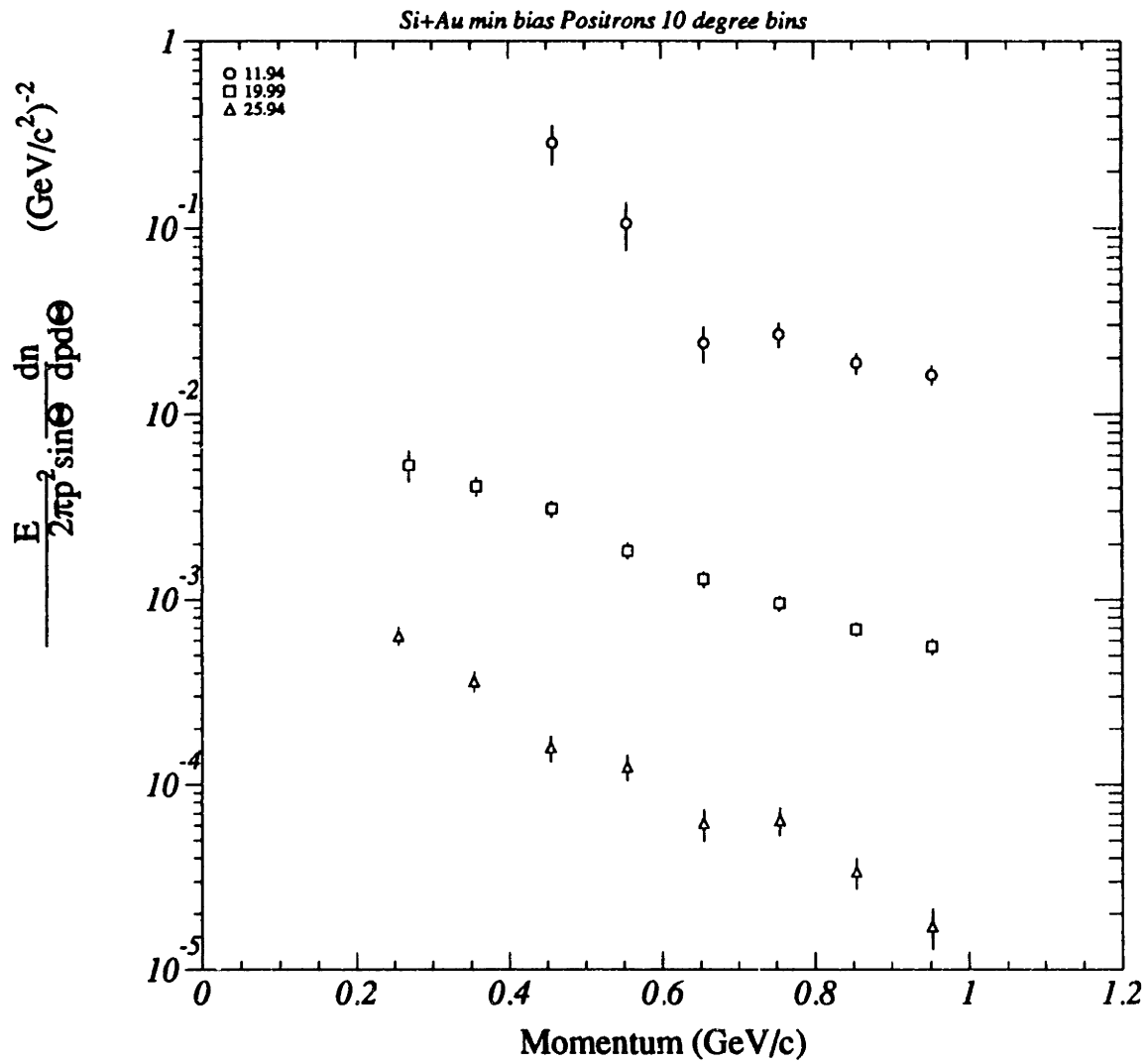
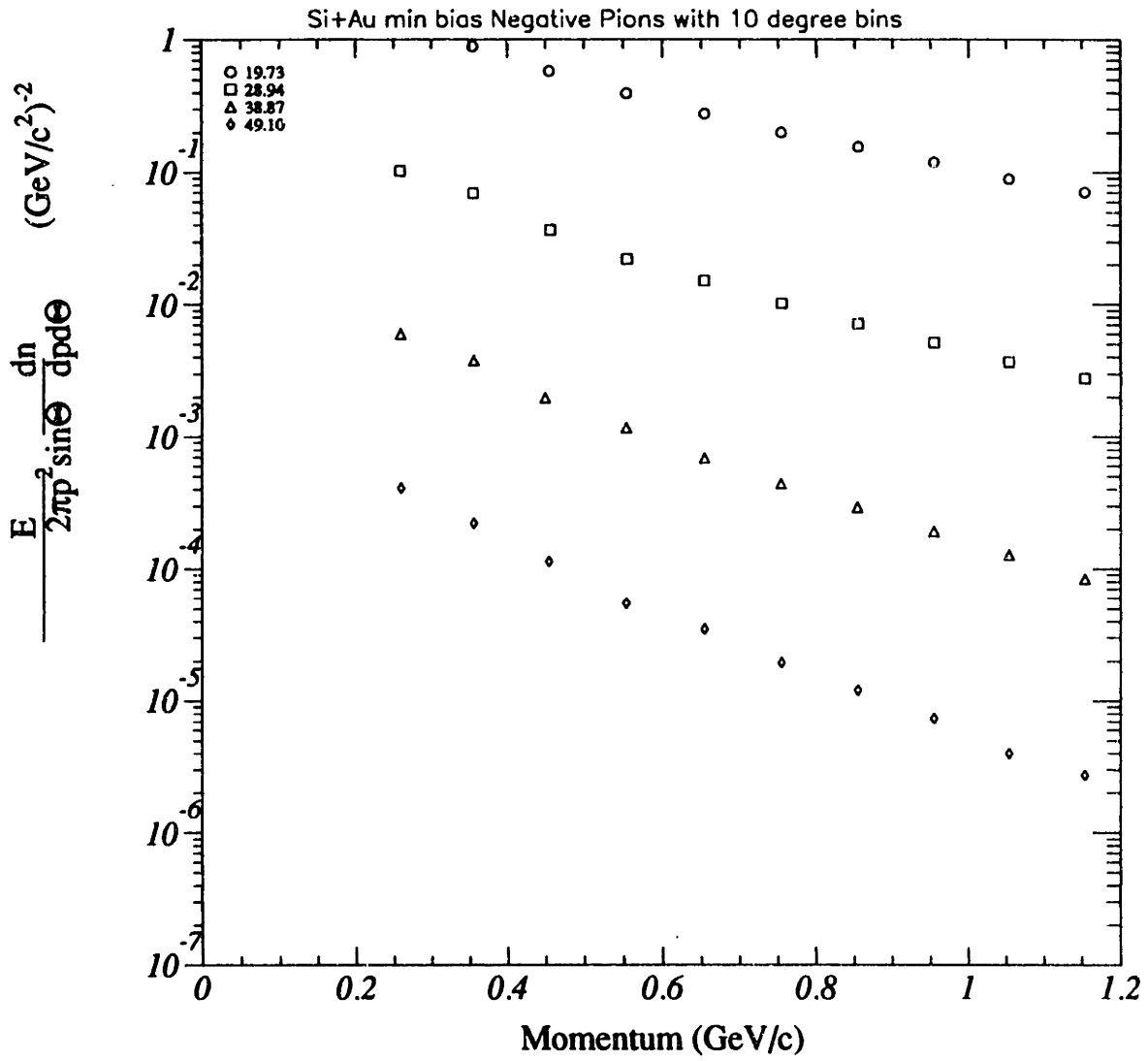Figure 5-2: Differential Yields in (p, θ) for Positrons with Au 1% target and 5° and 14° settings
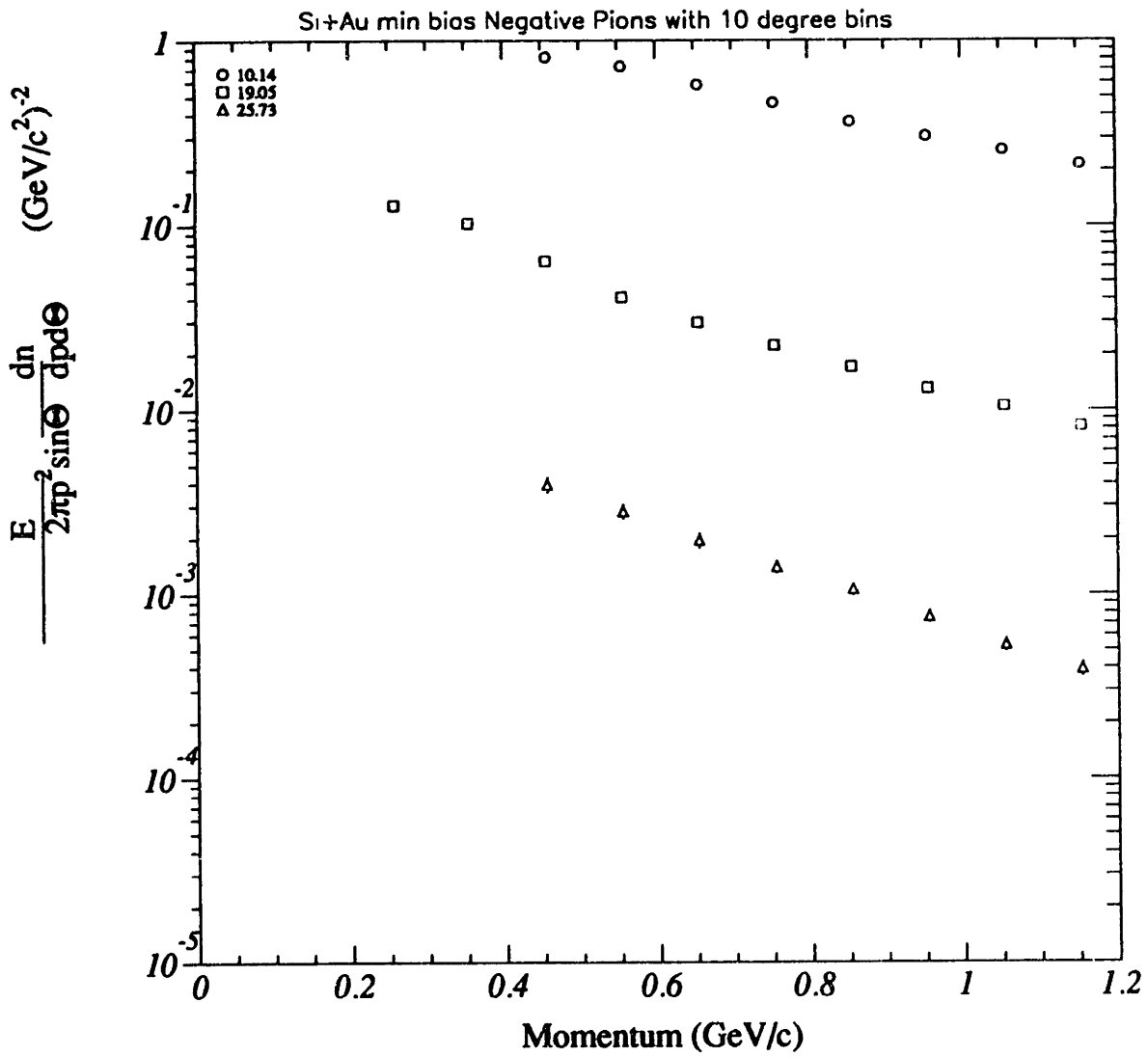
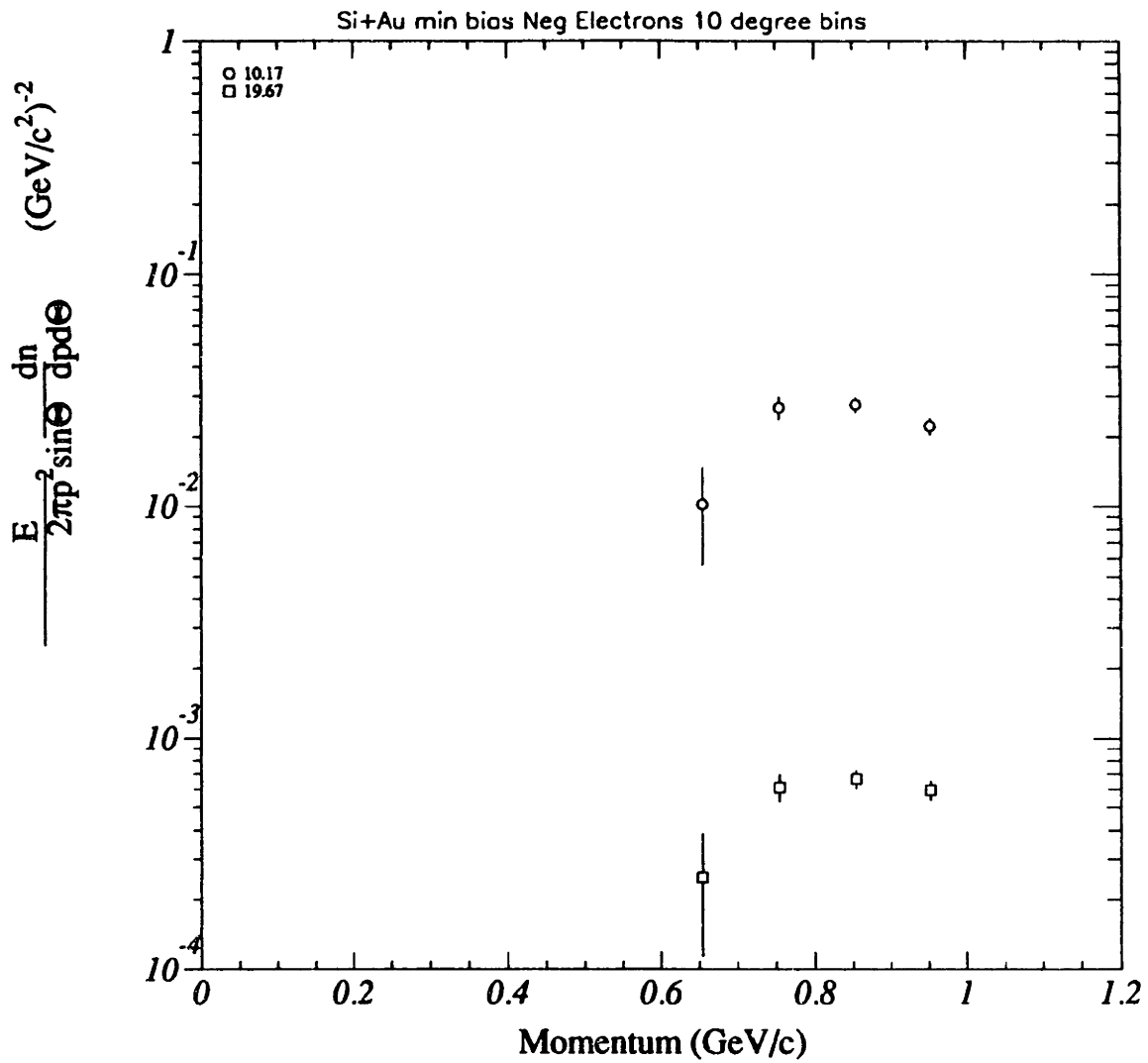Figure 5-3: Differential Yields in (p, θ) for Negative Pions with Au 1% target and 5° and 14° settings
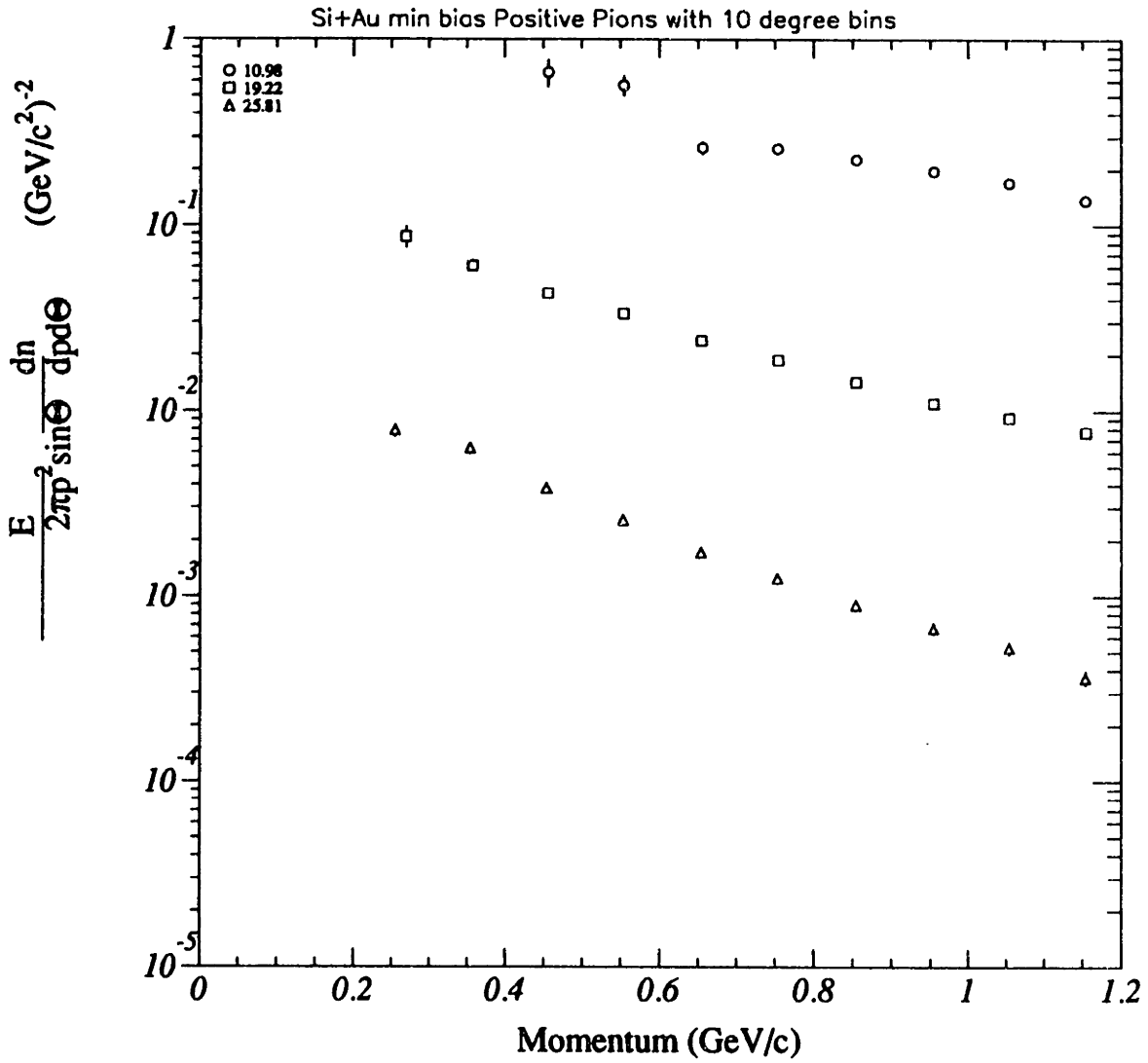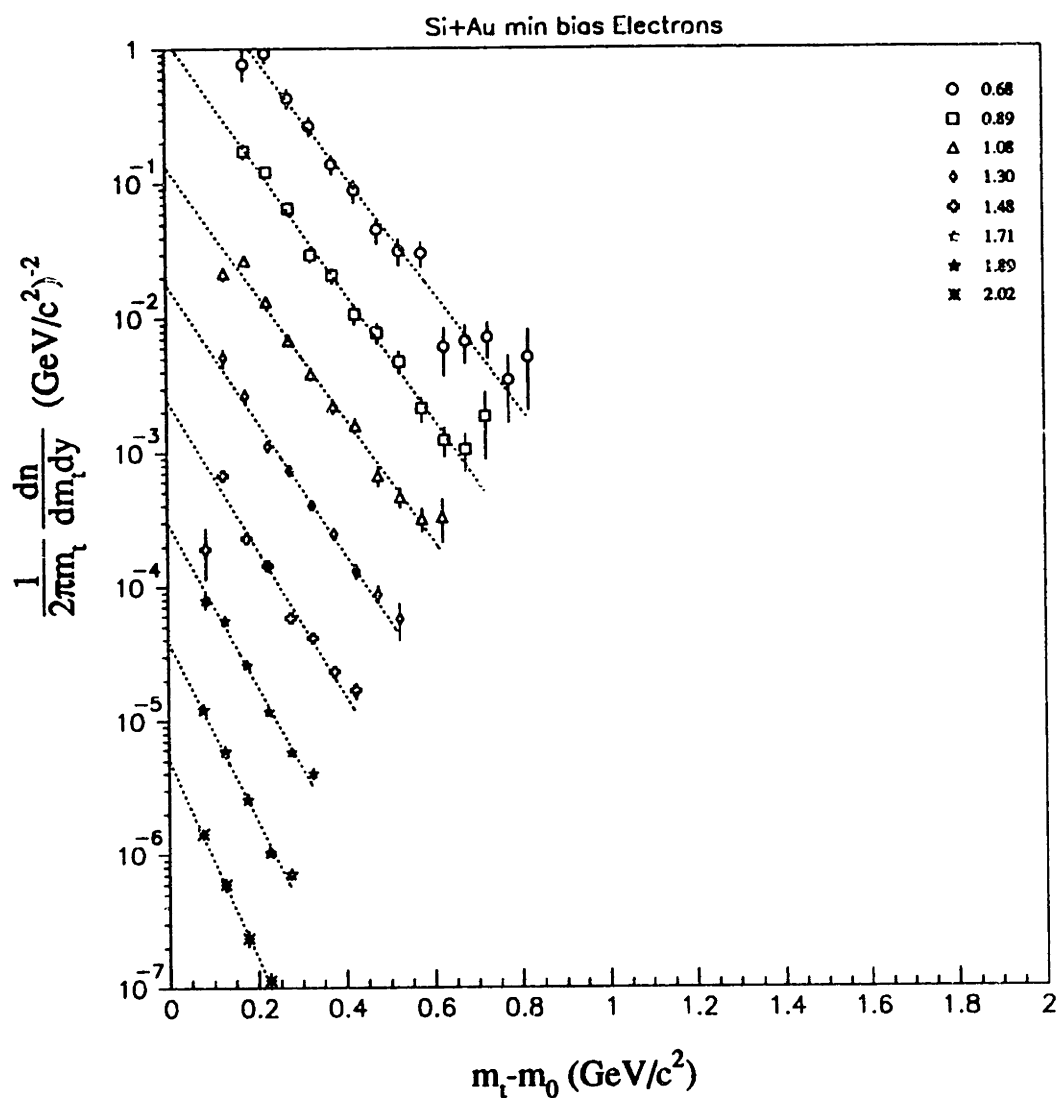
Figure 5-4: Differential Yields in (p, θ) for Positive Pions with Au 1% target and 5° and 14° settings

simulation of the E859 experimental detectors. The simulation package was given collision specifications from which it created the particles as predicted by the ARC model. The produced particles go through their collisions and decays, and are tracked through the spectrometer. Electrons and Positrons are believed to come primarily from the decays of π^o's, which have a lifetime of 8.3×10^{-17} seconds. The photons then convert into pairs when they strike the target material. The Geant simulation created 5000 events, each of which had 21 π^o's. The spectrometer was set at a reaction angle of $14°$, with the magnet at 2 kGauss and B polarity. The resulting data was then analysed by the same procedure as the real data to obtain cross-section histograms. The results are shown in (p, θ) space in figures 5-9 and 5-10. The second $10°$ slice of the electrons is limited to only the higher momentum values because the lower momentum electrons were all bent out of the spectrometer by the magnet. The simulated positron data corresponds well with the actual positron data over the .2-1.0 GeV/c momentum range and $14°$-$34°$ angular range. While the simulated electron data is reasonably similar to the actual data, there are more fluctuations from the limited statistics. It is clear that more statistics are needed for further investigation of this aspect of high-energy collisions.

The variation of the contamination of $e^\pm$ by $\pi^\pm$ is a function of the area of overlap of their distributions on the PID plot. The increase of this overlap with momentum can be observed in terms of the cross-section for $e^\pm$ to fall in the overlap region. This was found by using the freq(x) function to calculate the fraction of $e^\pm$ in the TOF-ID region in each momentum slice. This value subtracted from one and divided by the total $e^\pm$ gaussian integral gave the fraction of $e^\pm$ falling in the overlap region. The $e^\pm$ overlap fractions for the .6-1.0 GeV/c momentum slices were multiplied by the total differential yields calculated in the (p, θ) space and plotted in figures 5-11 and 5-12. The results are shown for the Au 1% targets with the $5°$ and $14°$ runs because they had better statistics.

In figures 5-13 and 5-14, $e^\pm$ from the Au 3% target are plotted in the (y, m_t) space. Each slice in rapidity has been scaled down by a factor of 10 and an exponential fit has been made. The fits are reasonably good and show a decrease in slope as the
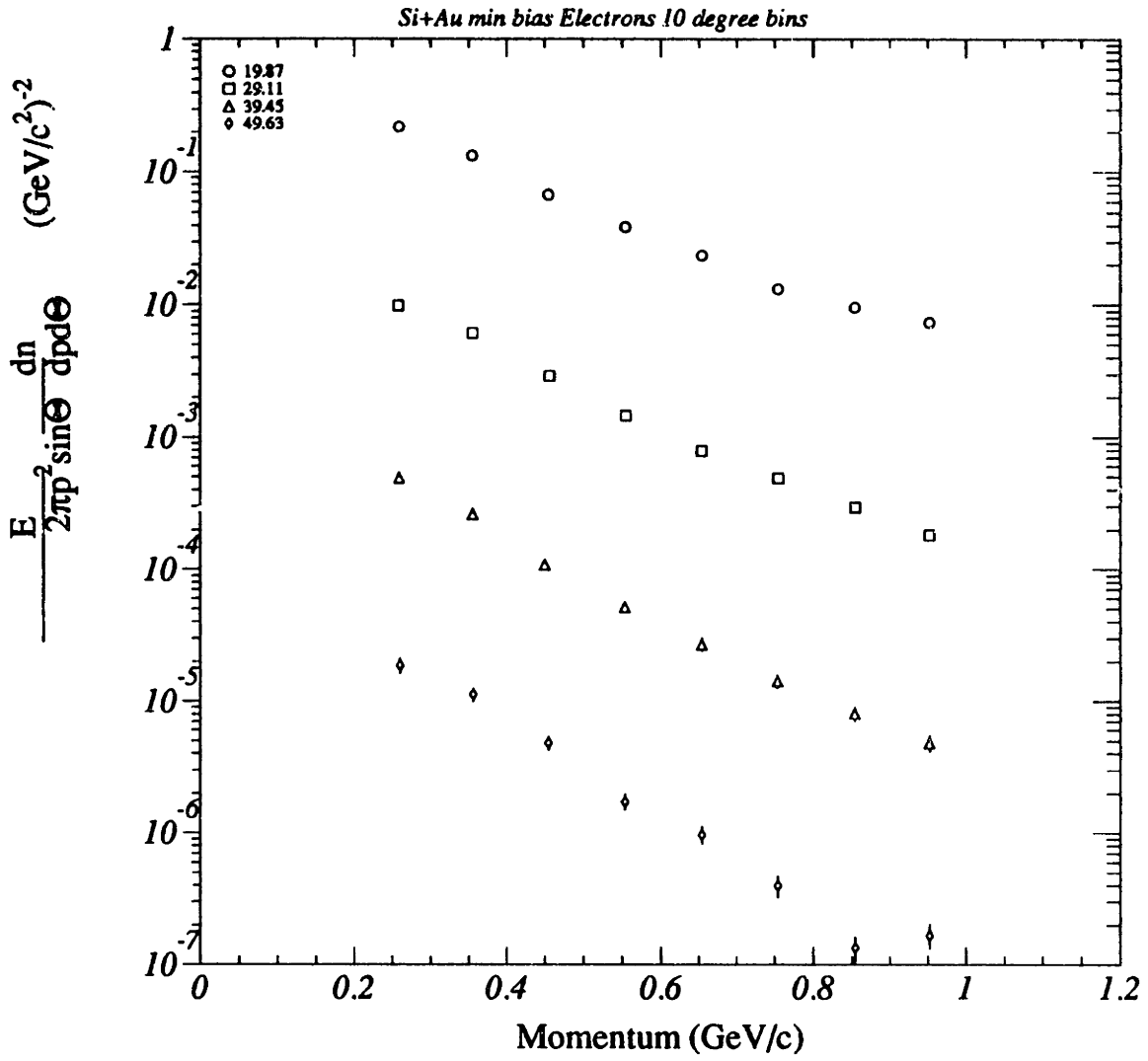
Figure 5-5: Differential Yields in (p, θ) for Electrons with Au 3% target and 14°, 24°, 34° and 44° settings
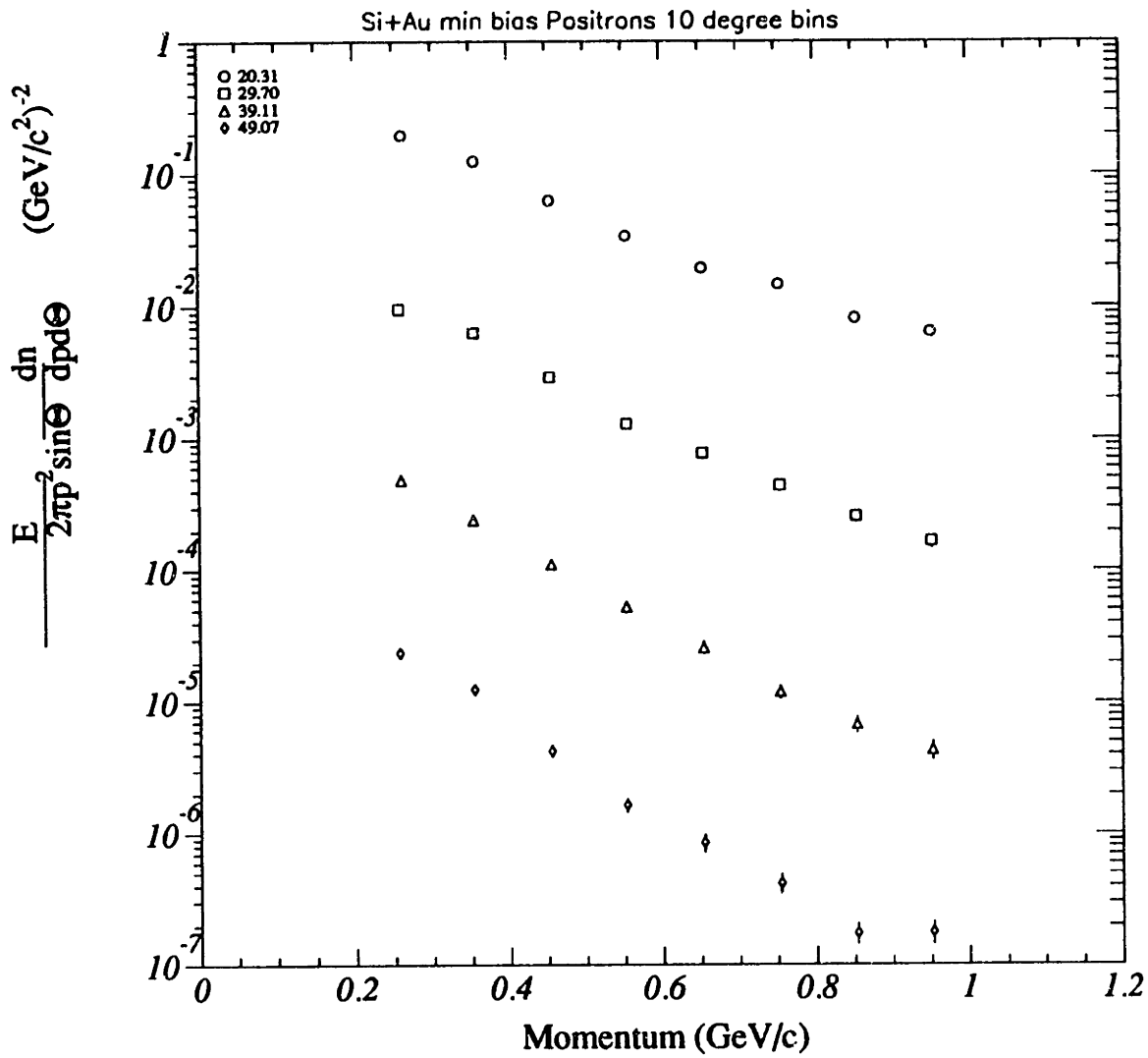
Figure 5-6: Differential Yields in (p, θ) for Positrons with Au 3% target and 14°, 24°, 34° and 44° settings

Figure 5-7: Differential Yields in (p, θ) for Negative Pions with Au 3% target and 14°, 24°, 34° and 44° settings
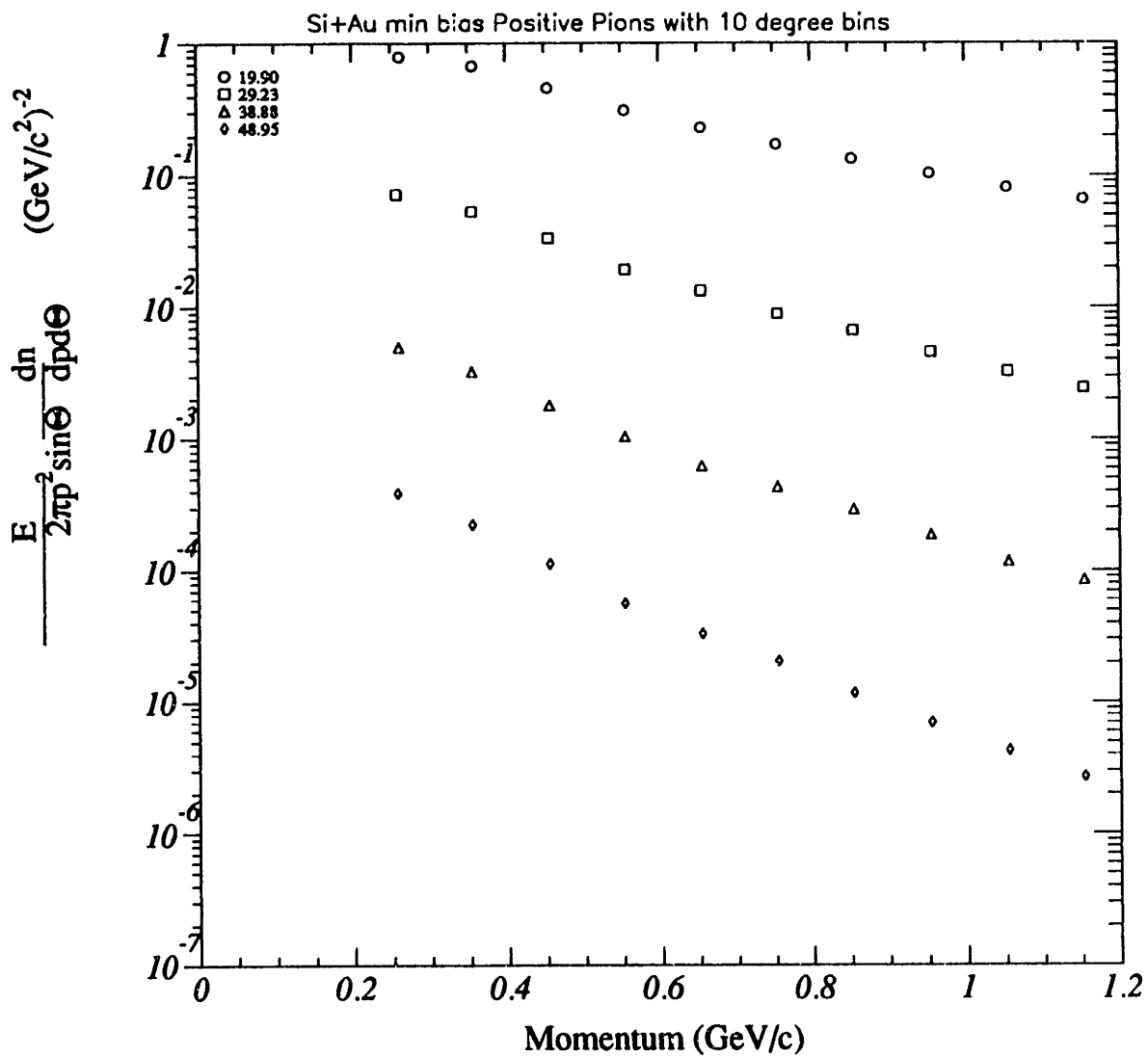
Figure 5-8: Differential Yields in (p, θ) for Positive Pions with Au 3% target and 14°, 24°, 34° and 44° settings
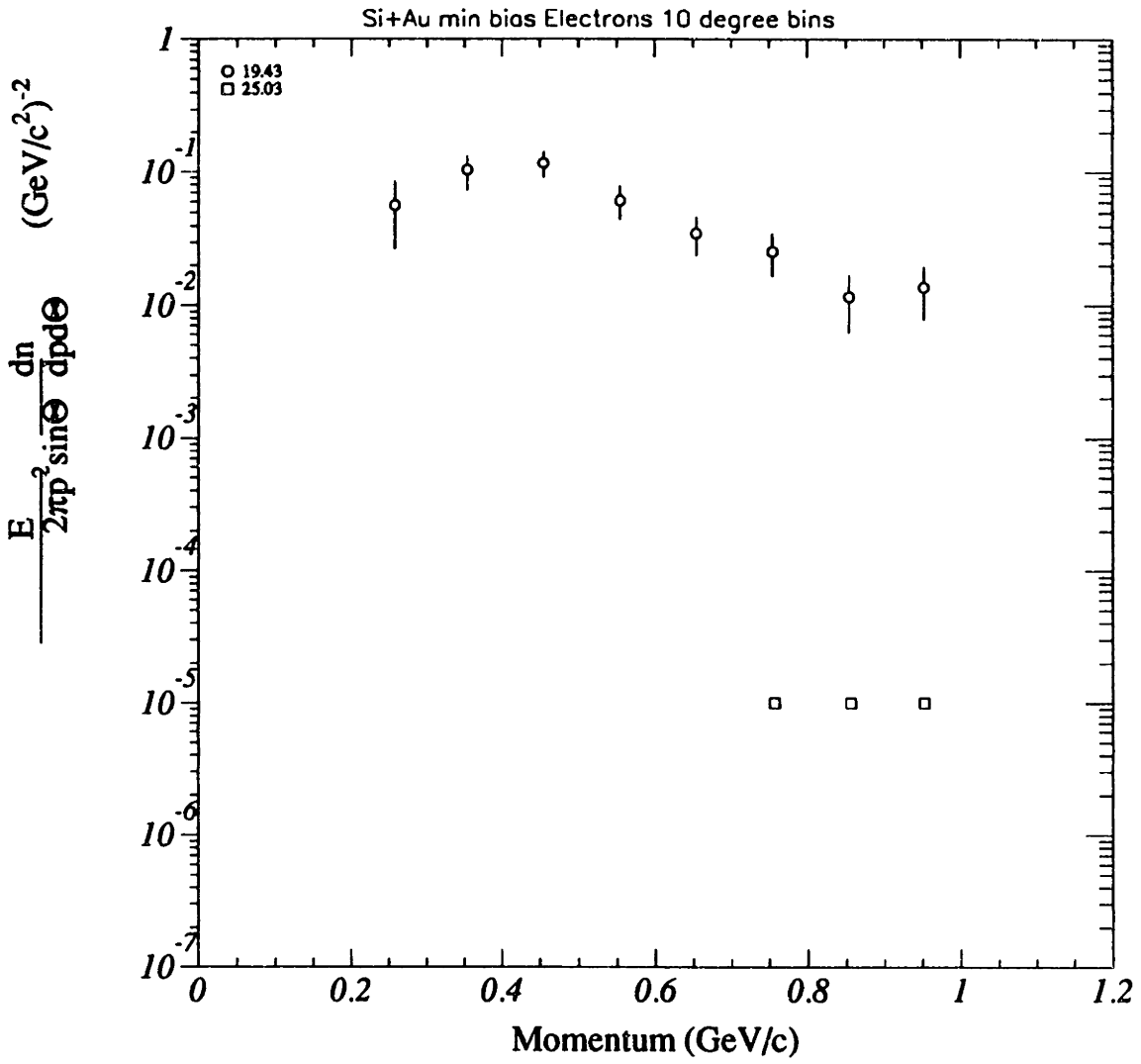
Figure 5-9: Geant Simulation Differential Yields in (p, θ) for Electrons with Au 3% target and 14° setting
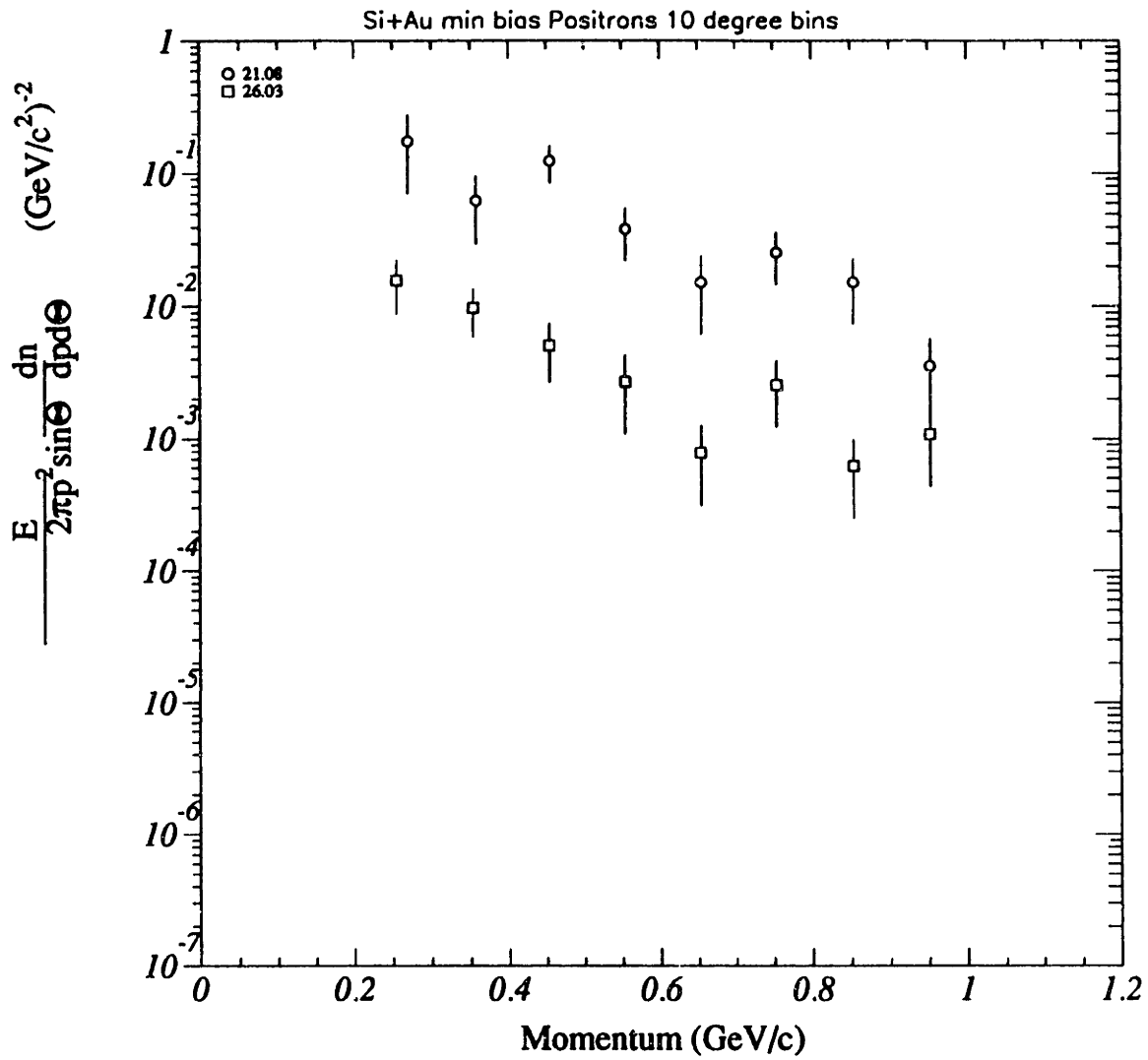
Figure 5-10: Geant Simulation Differential Yields in (p, θ) for Positrons with Au 3% target and 14° setting

Si+Au min bias Neg Electrons 10 degree bins

○ 10.17
□ 19.67

$E \dfrac{1}{2\pi p^2 \sin\Theta} \dfrac{dn}{dp d\Theta}$ $(GeV/c^2)^{-2}$

1

10^{-1}

10^{-2}

10^{-3}

10^{-4}

0 0.2 0.4 0.6 0.8 1 1.2

Momentum (GeV/c)

Figure 5-11: Differential Yields in (p, θ) for Electrons in Overlap Region with Au 1% target and 5° and 14° settings

60

Si+Au min bias Neg Positrons 10 degree bins
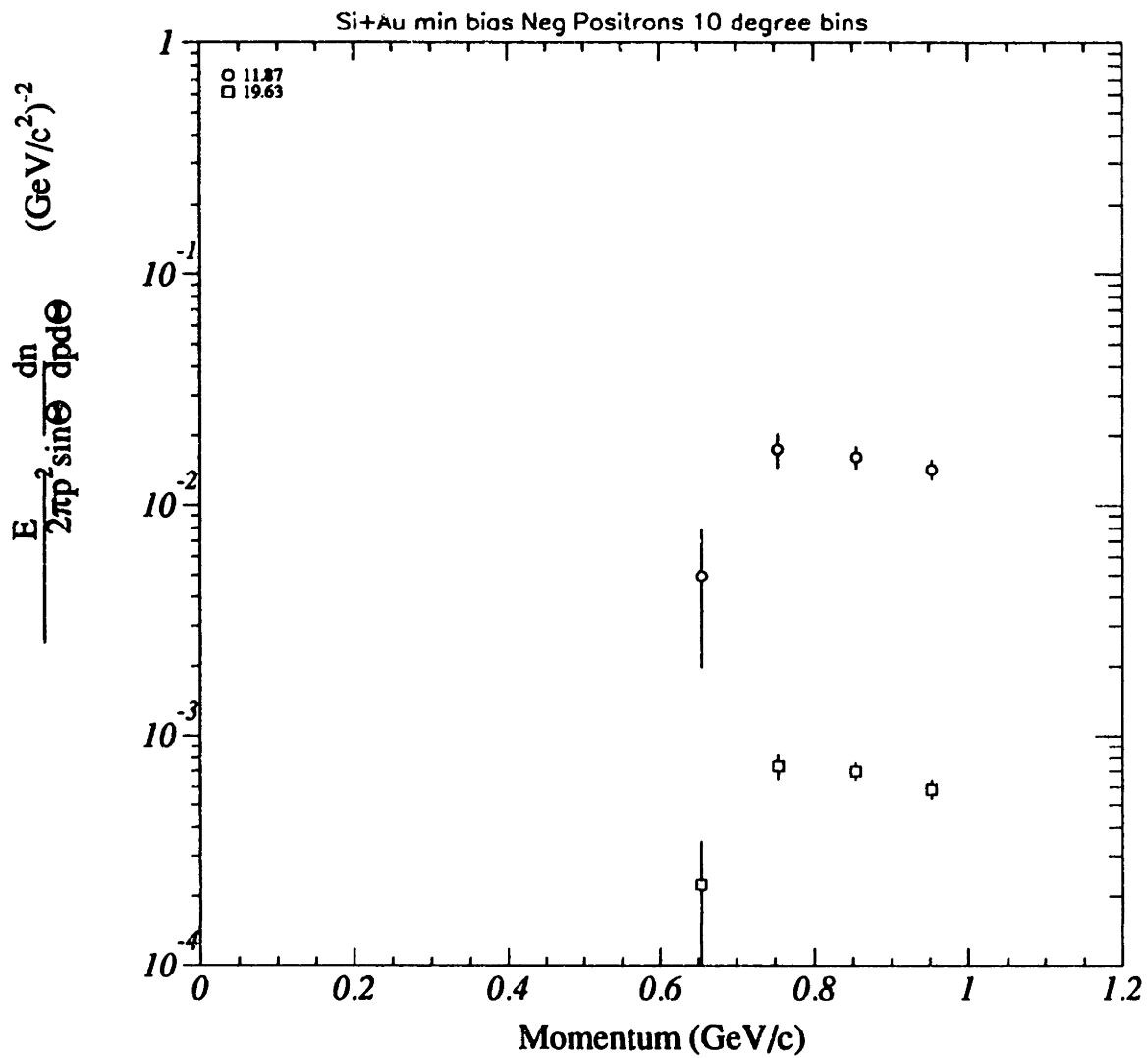
Figure 5-12: Differential Yields in (p, θ) for Positrons in Overlap Region with Au 1% target and 5° and 14° settings

61

rapidity increases. The slopes are plotted as a function of rapidity along with the total yields made by integrating over each rapidity slice in figures 5-15 and 5-16. Previous analysis done by Charles Parsons on data from 14.6 GeV/c per nucleon silicon on gold collisions resulted in total yields and and slope parameters for $e^{\pm}$ and $\pi^{\pm}$. The $\pi^{\pm}$ data had better statistics, and gave slope parameters of about .15 in a rapidity range of .5 to 2.5. The $\pi^{\pm}$ total yields had a gaussian shape around the mid-rapidity of about 1.5, with a peak yield of about 8. For $e^{\pm}$, the slope parameters for rapidities .5 to 1.5 have a mean of about .11 with a sigma of about .03. The statistics were too low to observe a gaussian figure in the total yield results, but the values have a mean of about .7 with a sigma of about .2. The slope parameter results presented in this work have significantly better statistics. At a rapidity of .75 the slope parameter is about .1, and as rapidity increases to 2 the slope parameter slowly drops to about .06. The $e^{\pm}$ total yields do not drop after mid-rapidity as the pions did. Above mid-rapidity they stay at about a dN/dy of 1.

Figure 5-13: Differential Yields in (y, m_t) for Electrons with Au 3% target and 14°, 24°, 34° and 44° settings
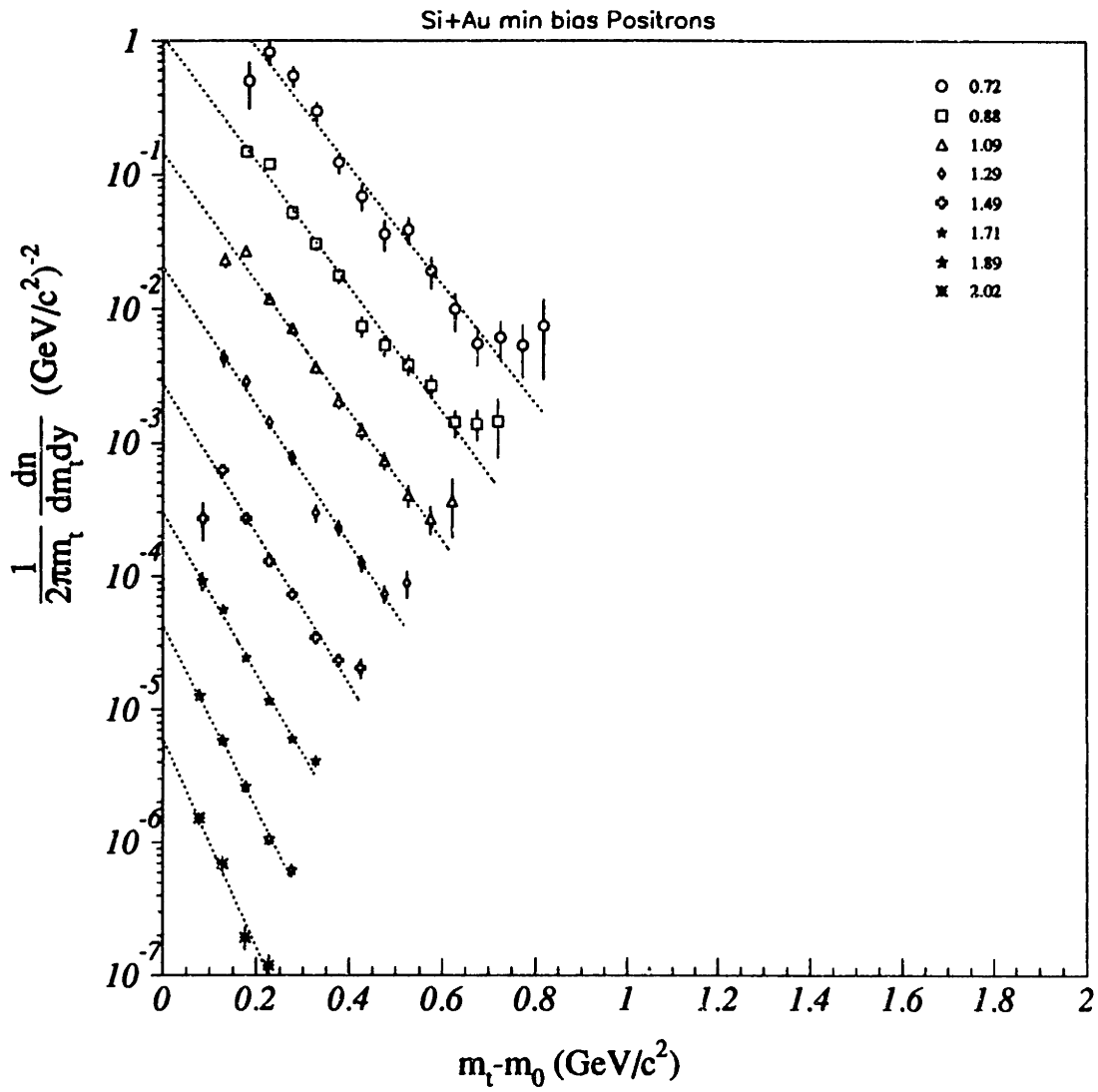
Figure 5-14: Differential Yields in (y, m_t) for Positrons with Au 3% target and 14°, 24°, 34° and 44° settings
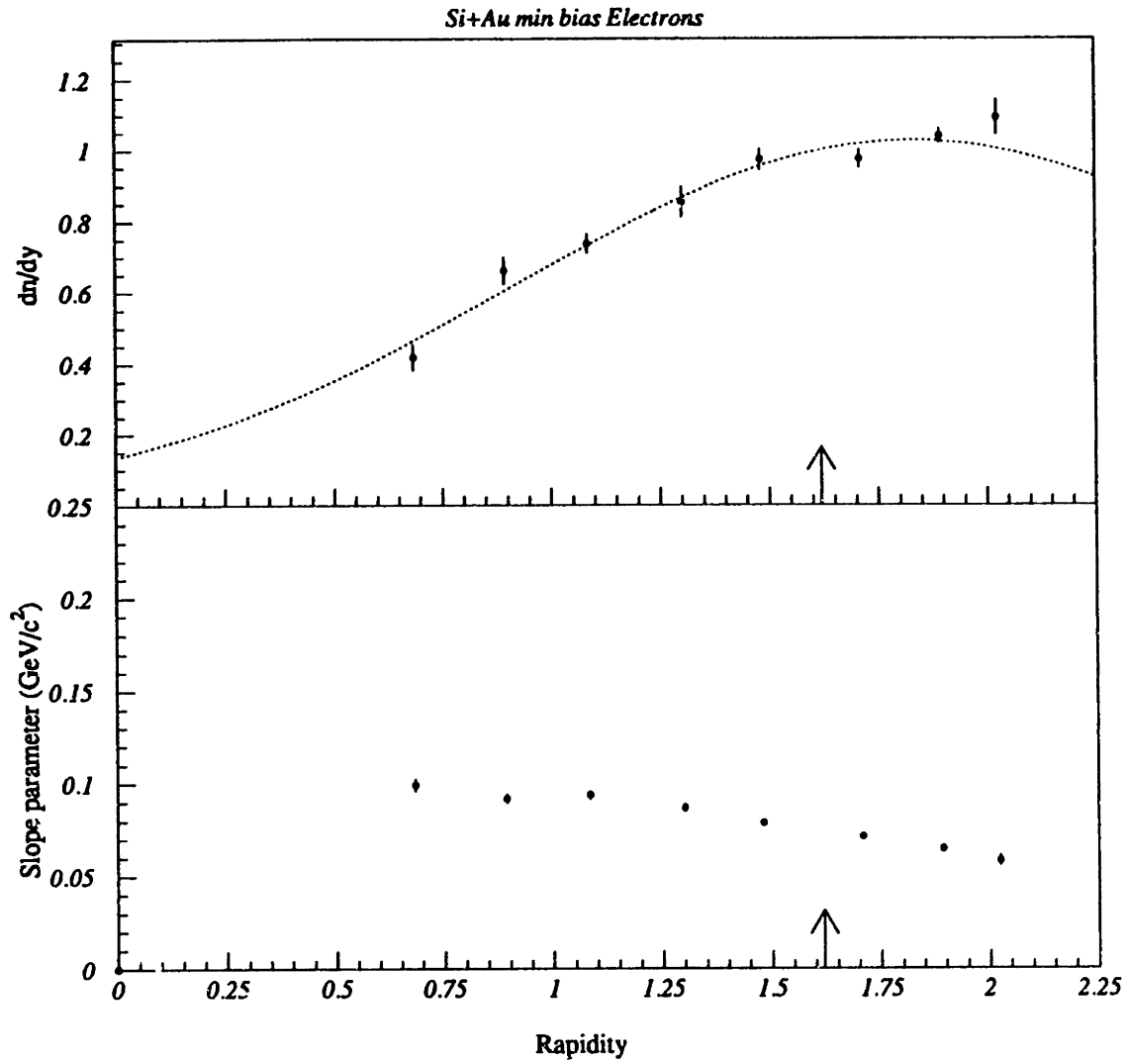
Figure 5-15: Total Yields for Electrons with Au 3% target and 14°, 24°, 34° and 44° settings
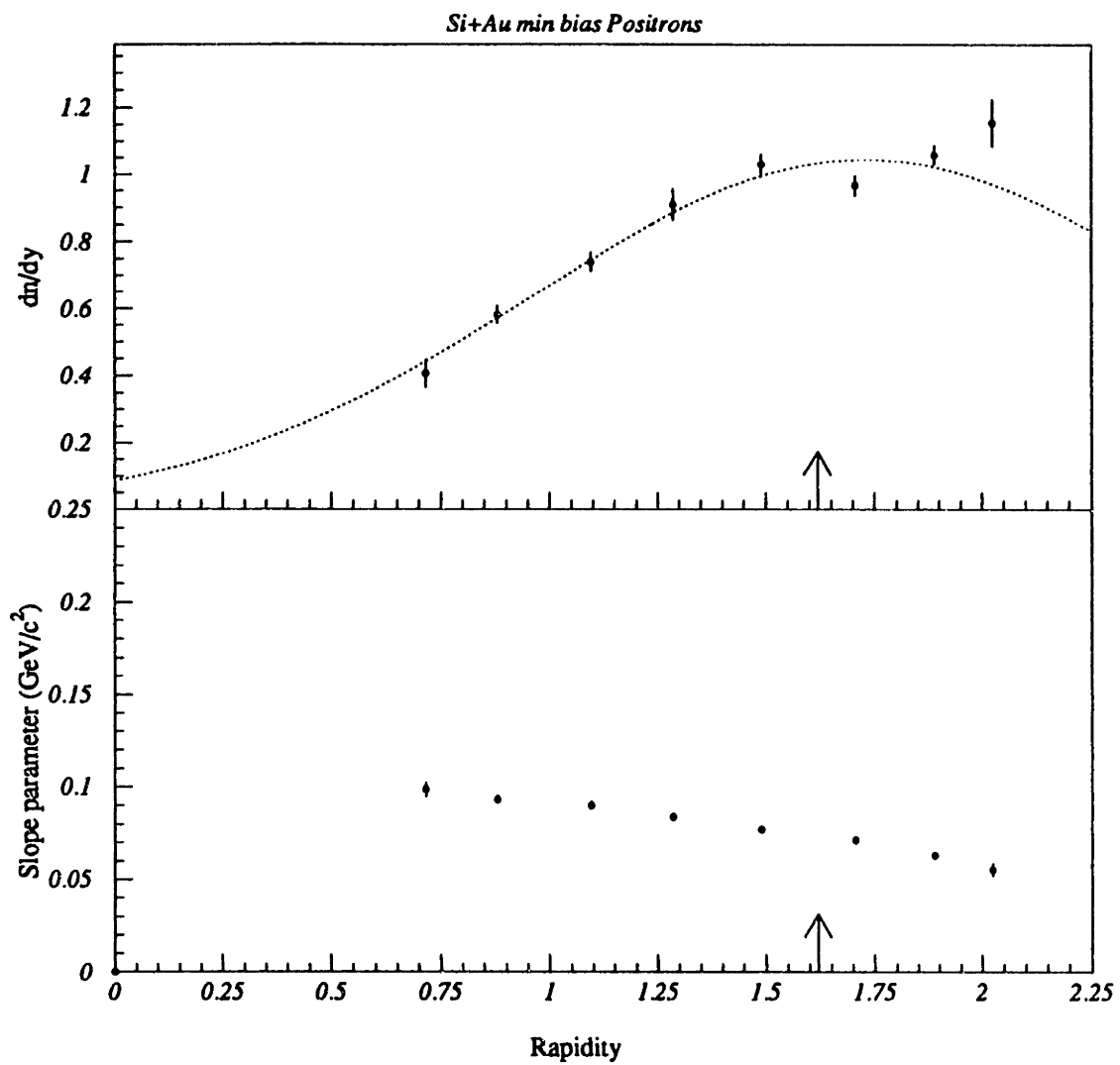
Figure 5-16: Total Yields for Positrons with Au 3% target and 14°, 24°, 34° and 44° settings

Chapter 6

Conclusion

This study was able to successfully determine several aspects of the gas Cerenkov counter's ability to discriminate between particles. The focus of the analysis was to determine the efficiency of the GasC at detectint electrons. In the process of doing that, the over-efficiency of the GasC for pions was determined. This led to a detailed examination of the resulting contamination of the electrons by pions. In the process, evidence for muons was discovered. The pion contaminations were obtained with reasonable confidence up to 1.0 GeV/c. These results were used to obtain differential and total yields for electrons and pions in inelastic collisions. The yields covered a reaction angle range from 5° to 54°, and a momentum range from .2 to 1.0 GeV/c.

.

Appendix A

TOF Wall Calibrations for $e^{\pm}$
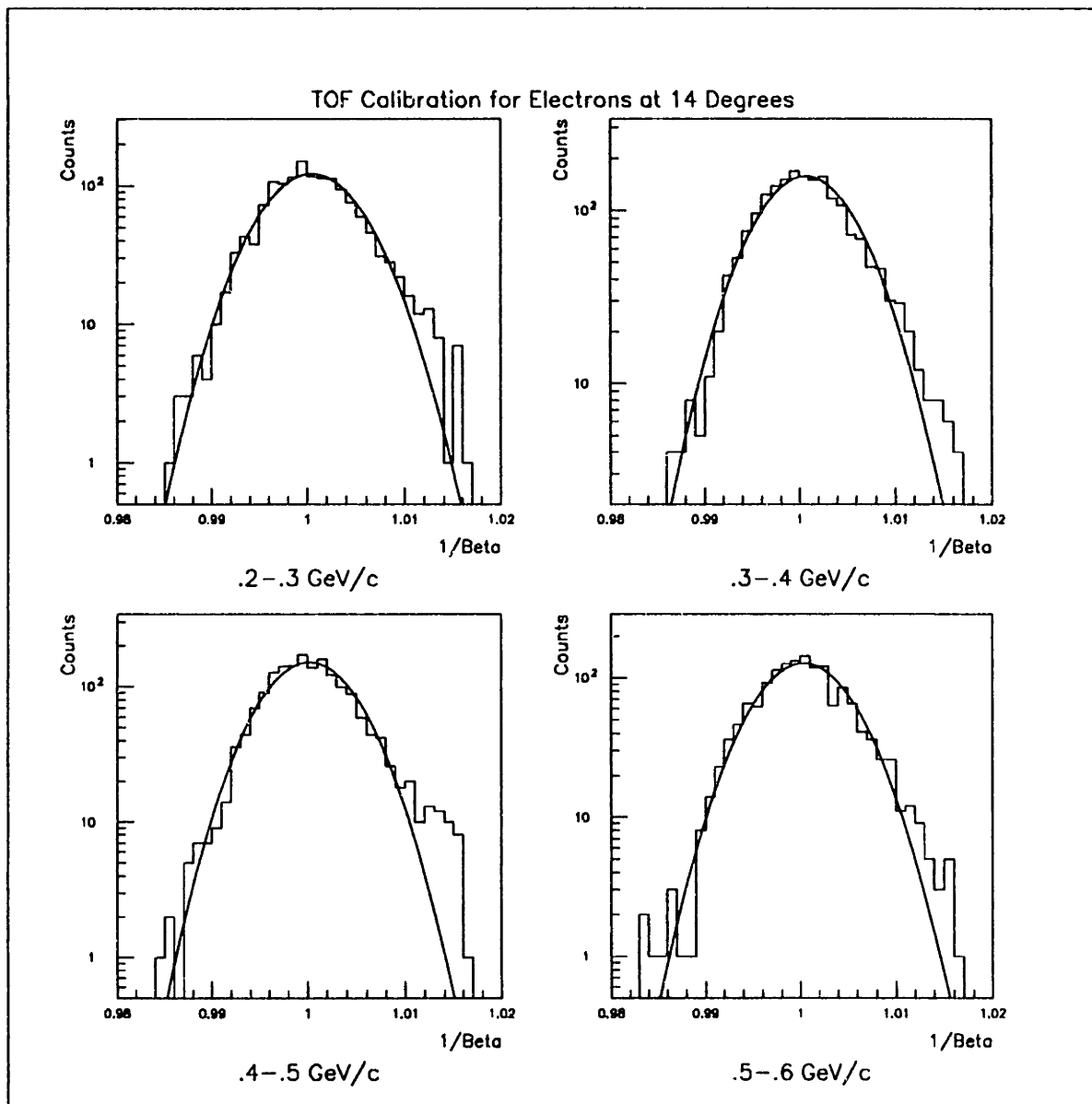
Figure A-1: TOF Wall Calibrations for Electrons
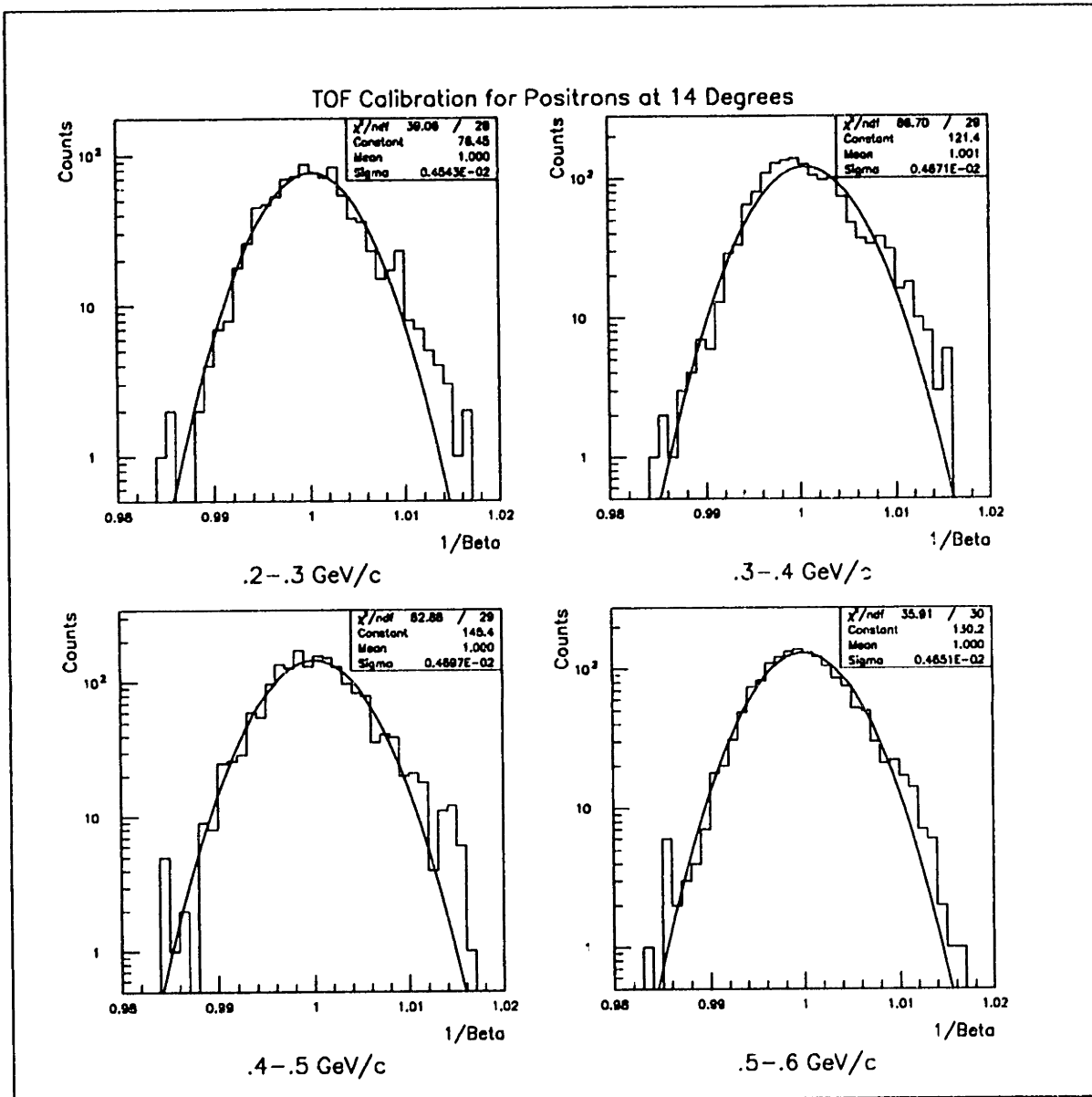
Figure A-2: TOF Wall Calibrations for Positrons

71

Appendix B

GasC Response to $e^{\pm}$ in TOF-ID Region
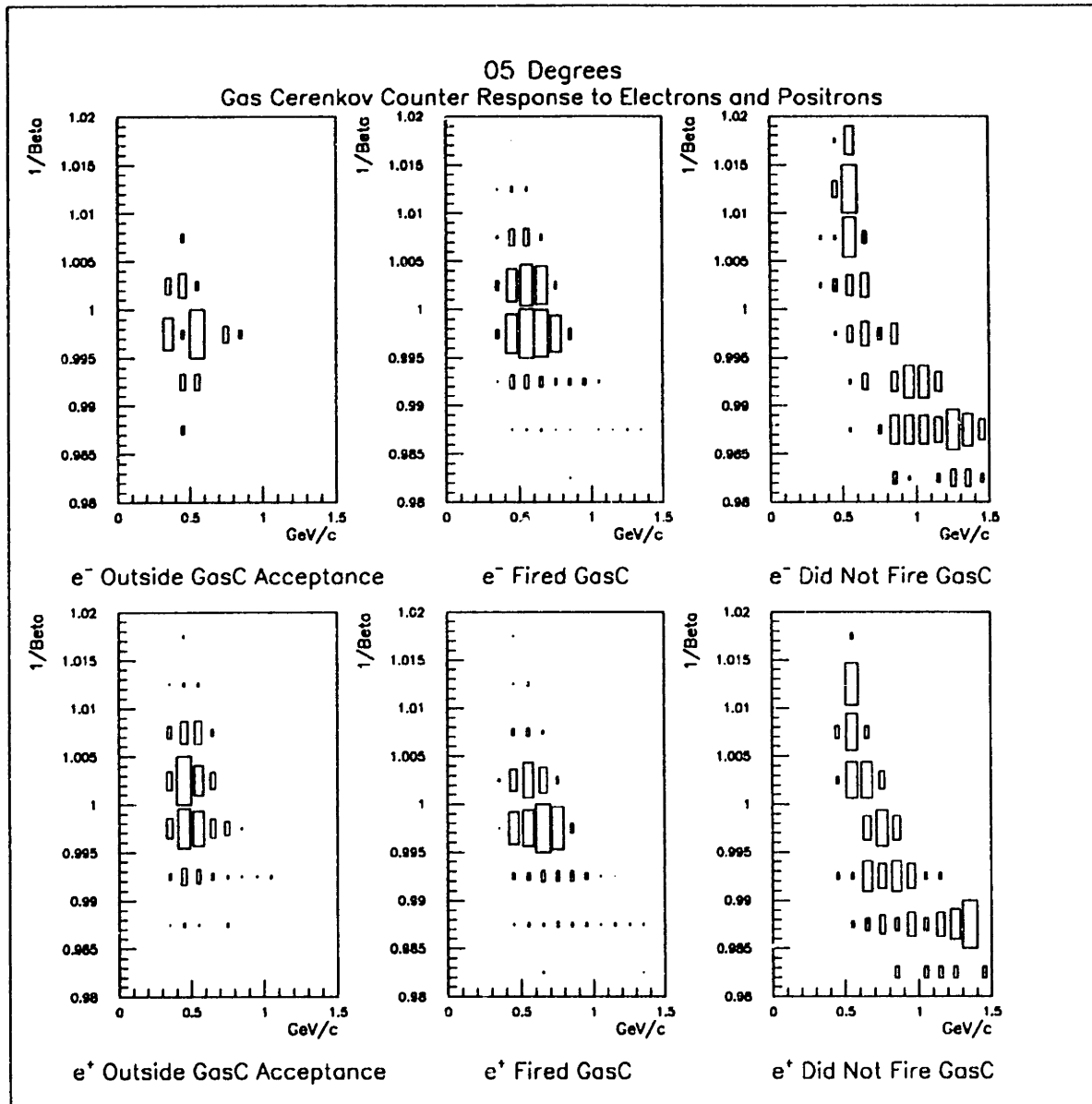
Figure B-1: GasC Response to $e^{\pm}$ at 5°

74
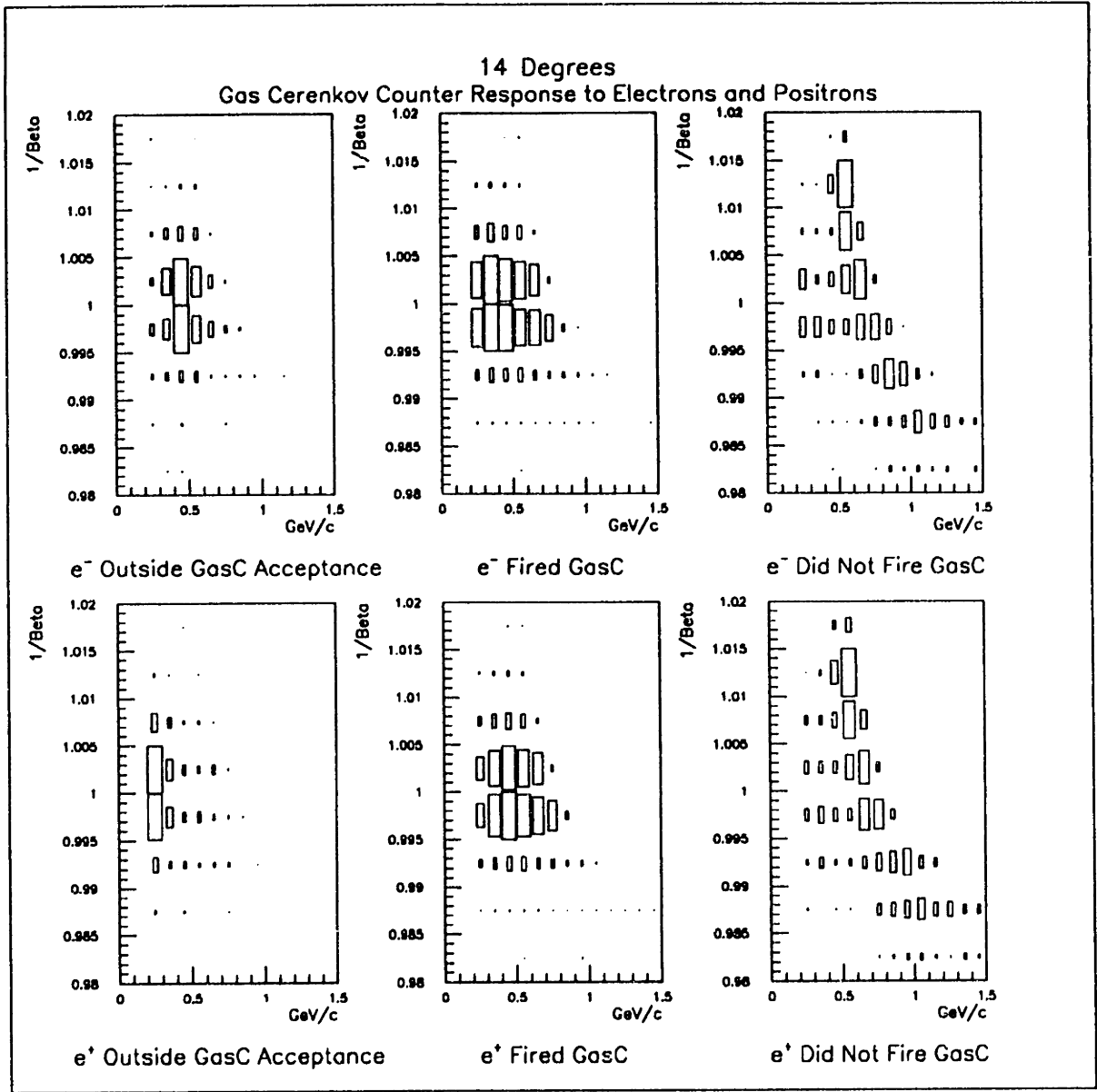
Figure B-2: GasC Response to $e^{\pm}$ at $14°$
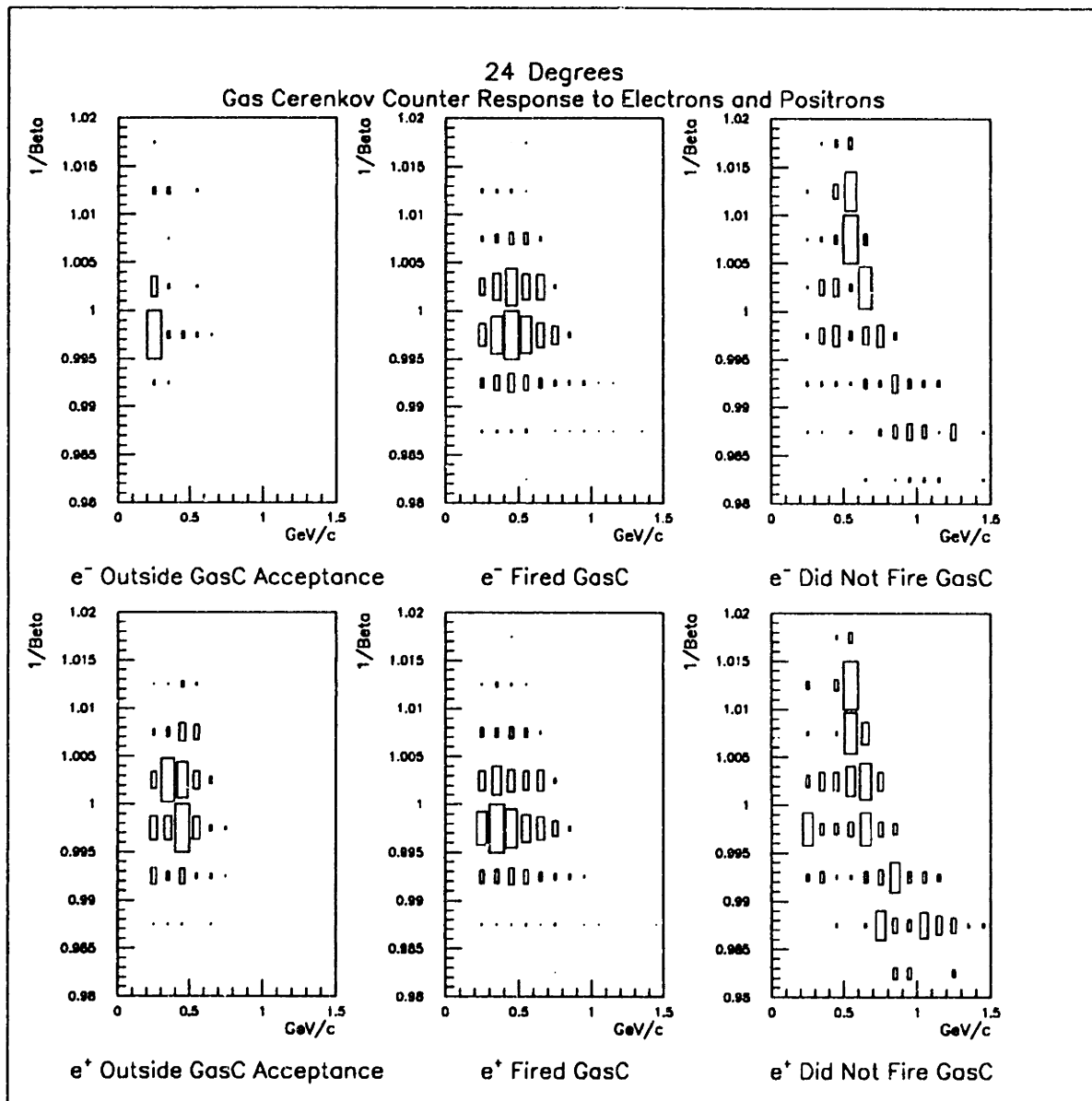
Figure B-3: GasC Response to $e^{\pm}$ at 24°
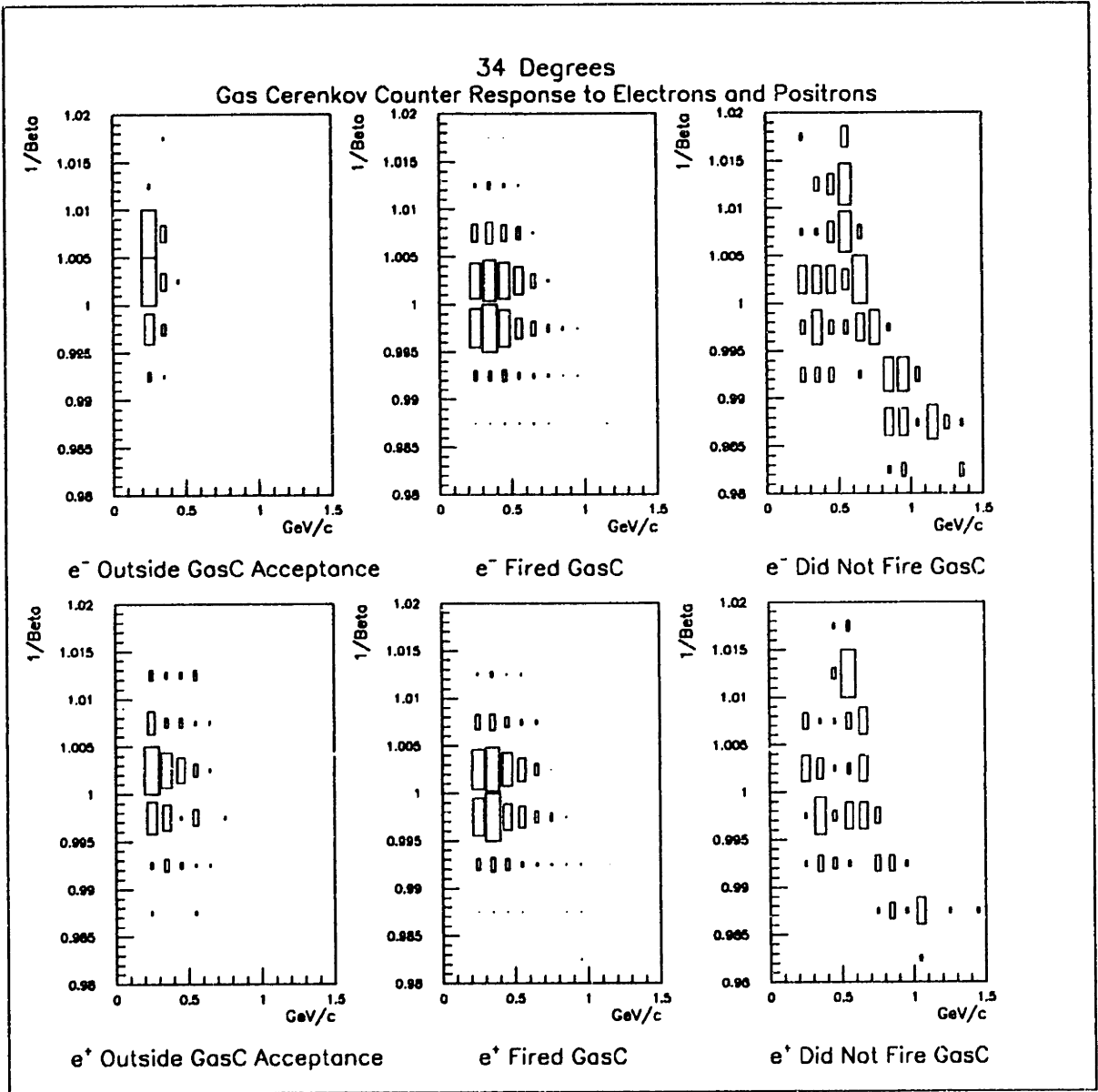
Figure B-4: GasC Response to $e^{\pm}$ at $34°$
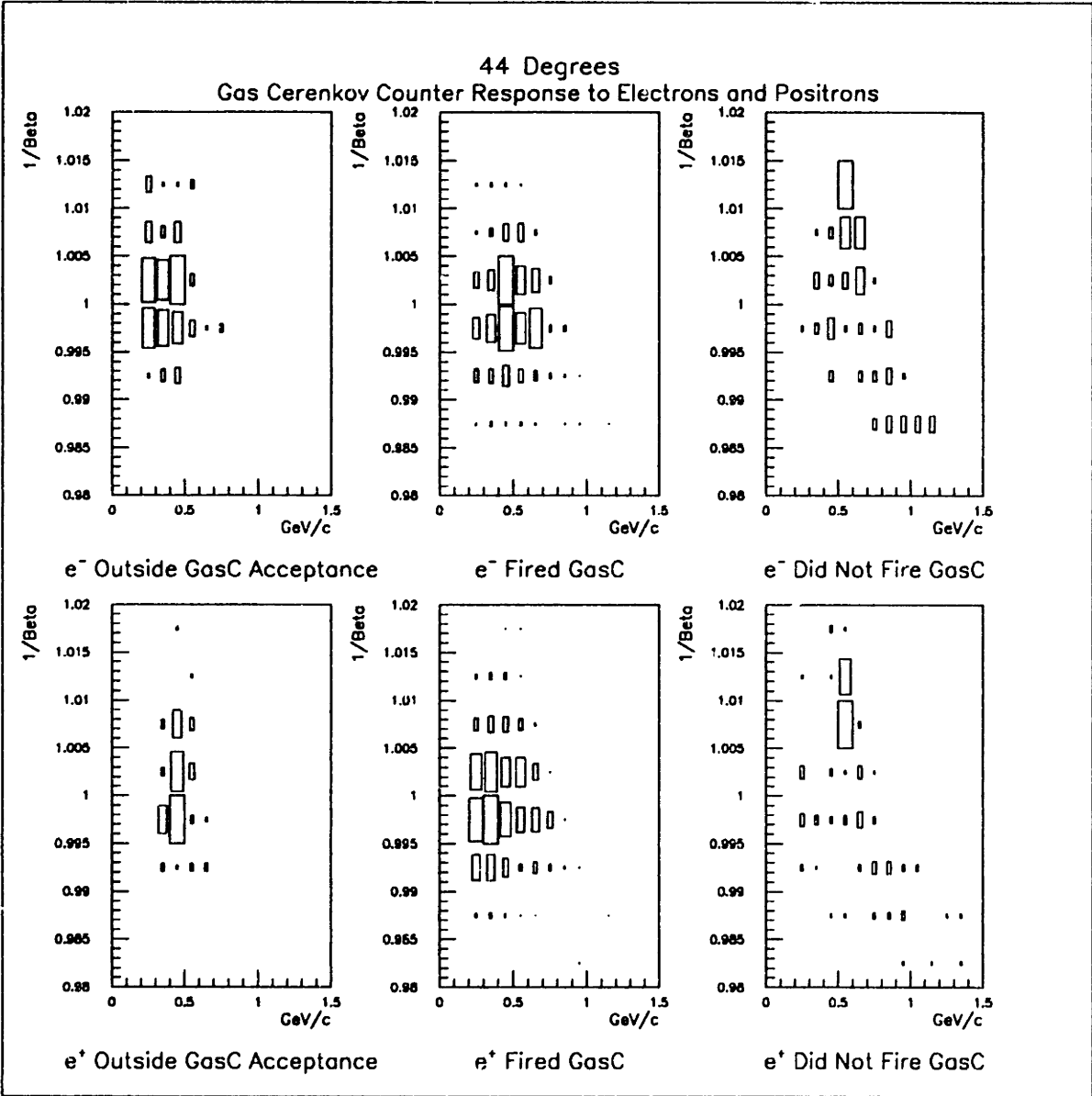
Figure B-5: GasC Response to $e^{\pm}$ at 44°

78

Appendix C

GasC Response to $\pi^{\pm}$ in TOF-ID Region
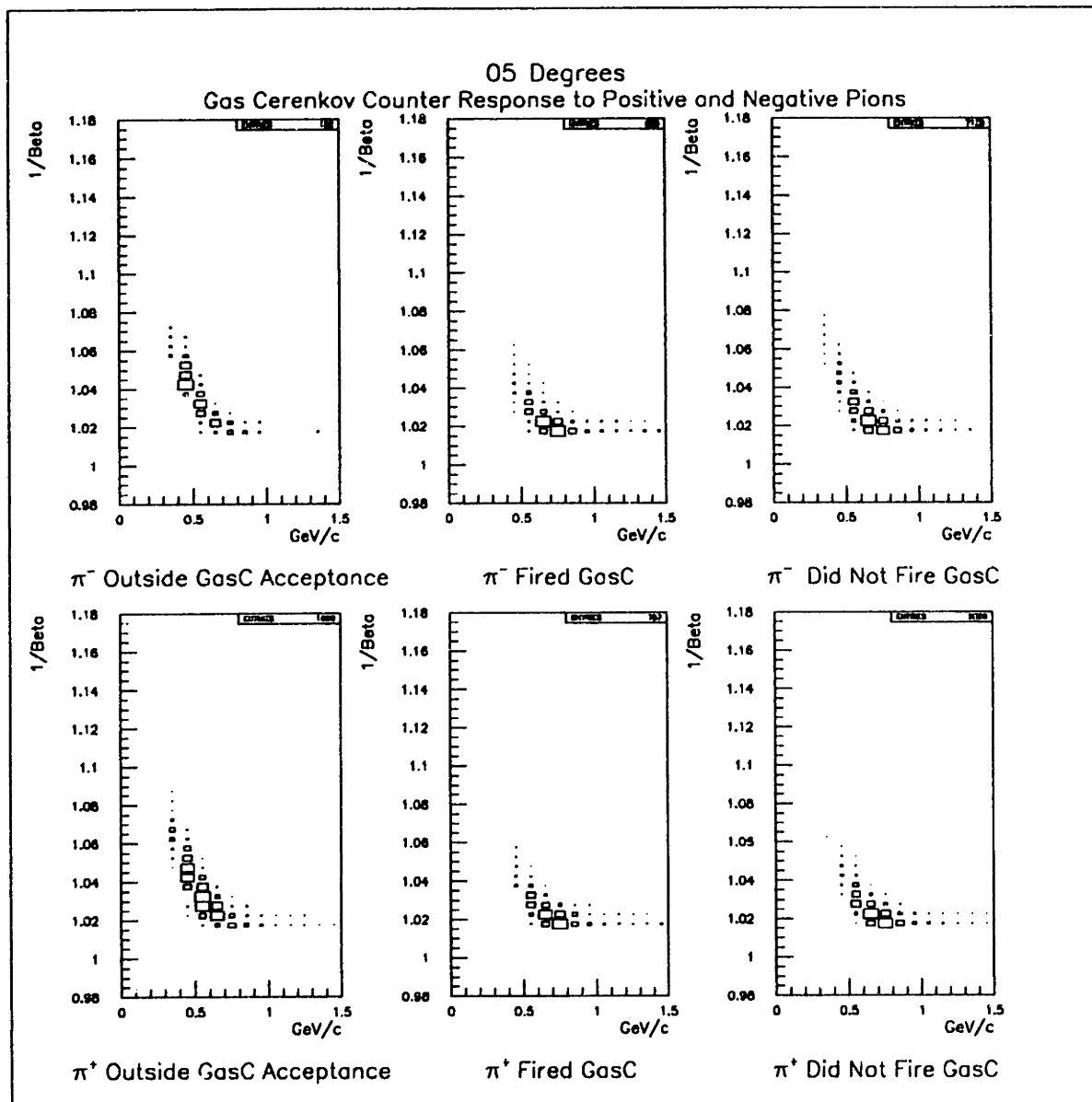
Figure C-1: GasC Response to $\pi^{\pm}$ at $5°$
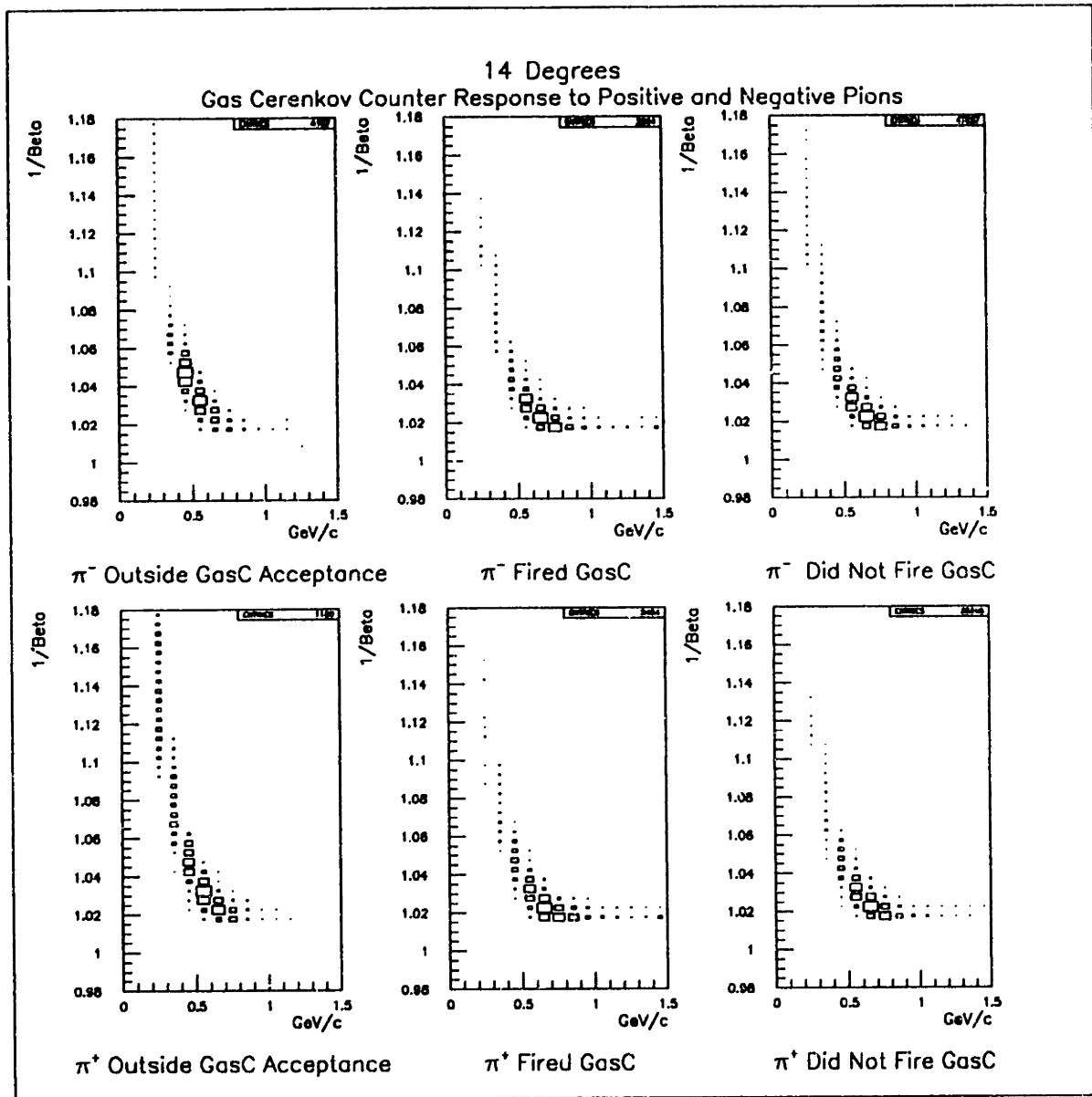
Figure C-2: GasC Response to $\pi^{\pm}$ at 14°
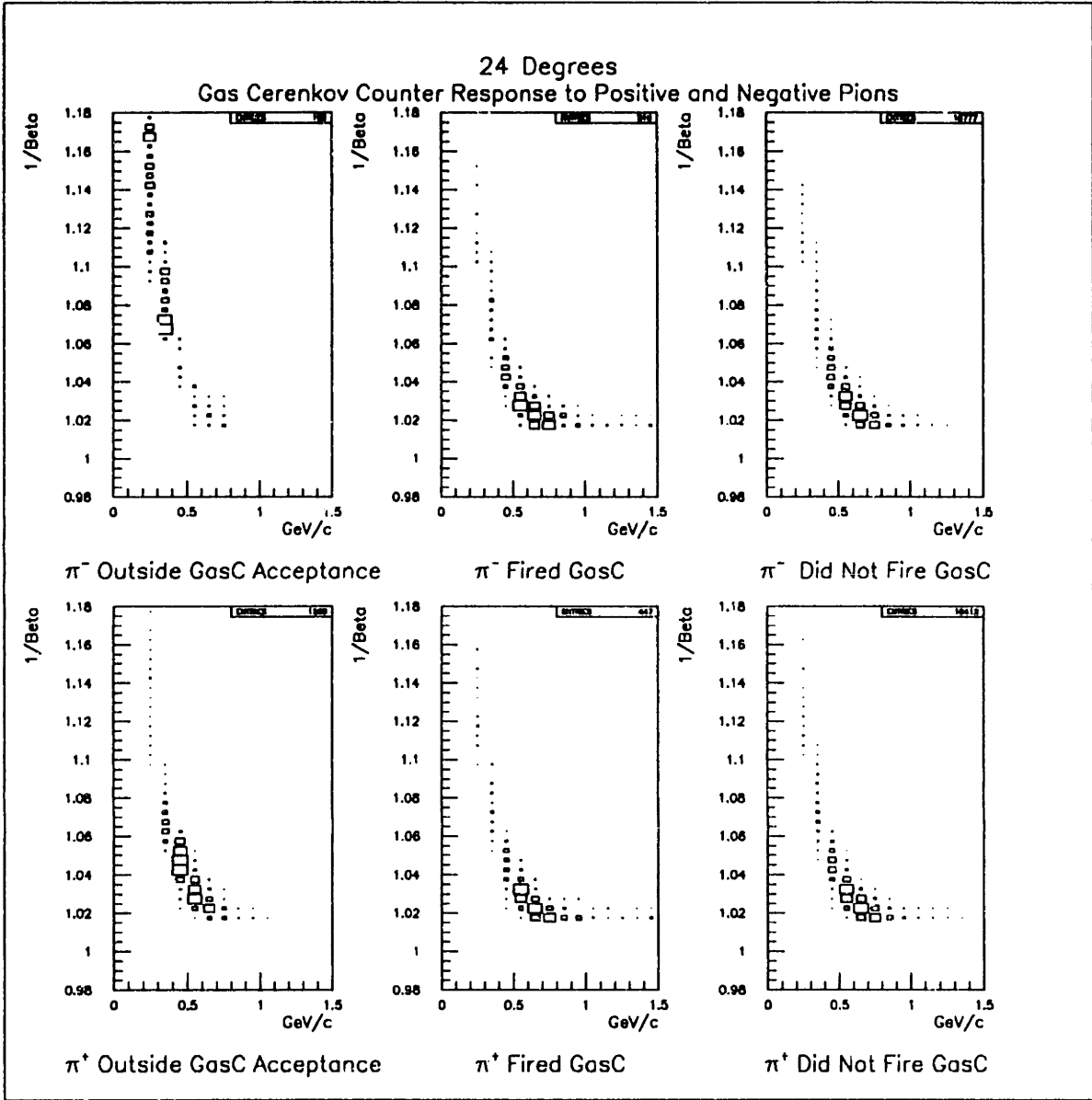
Figure C-3: GasC Response to $\pi^\pm$ at 24°

82
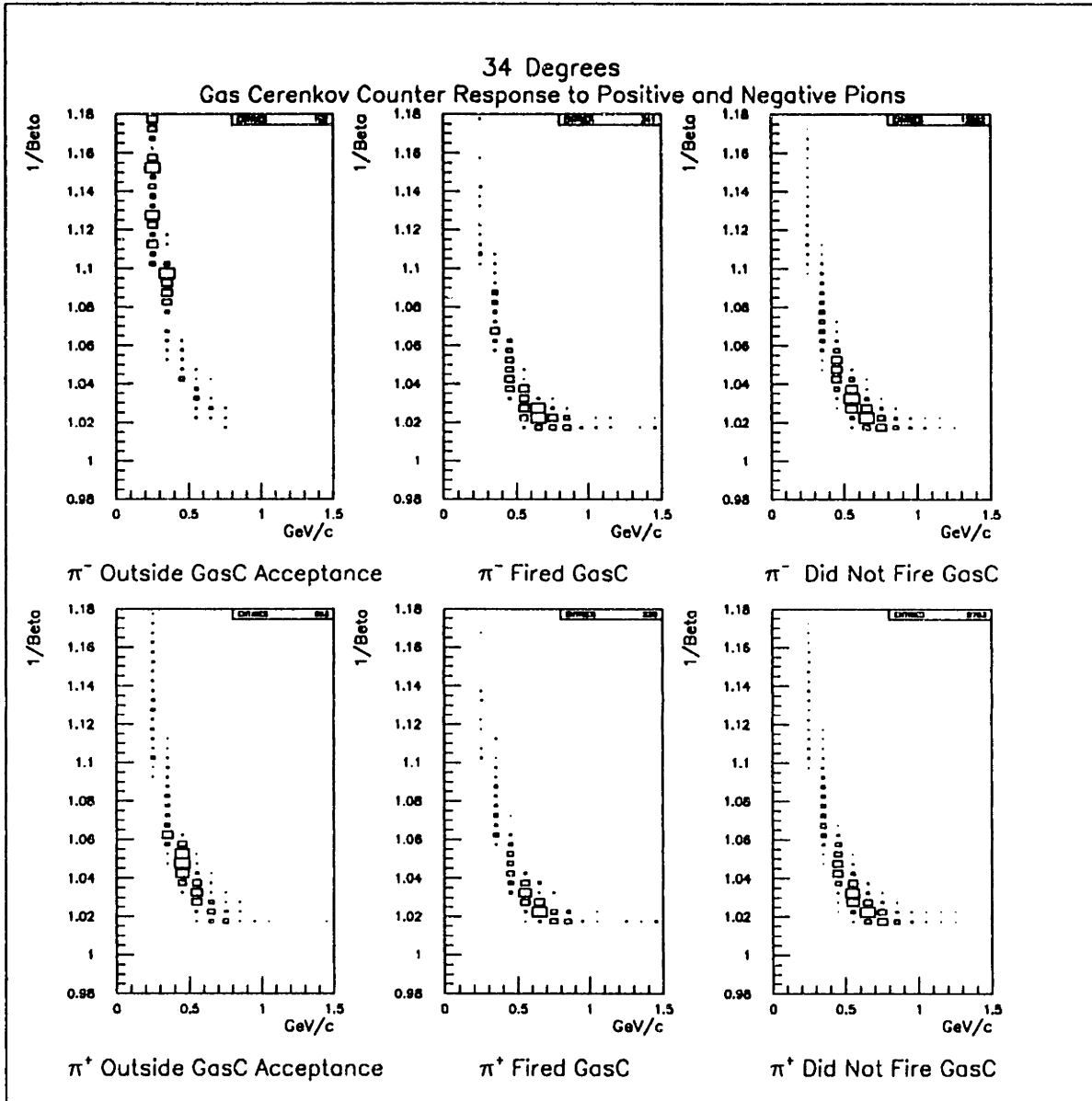
Figure C-4: GasC Response to $\pi^{\pm}$ at 34°
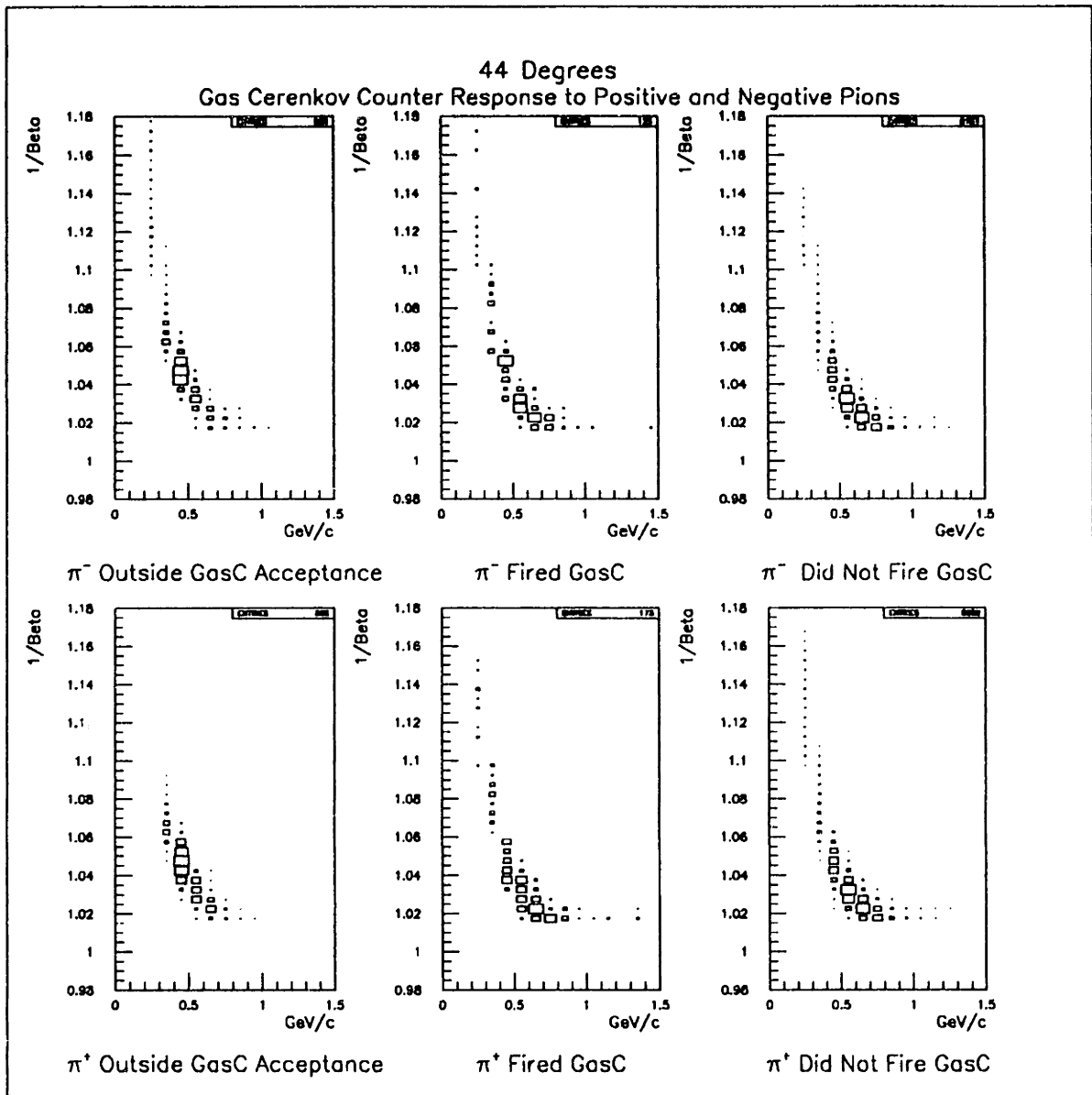
Figure C-5: GasC Response to $\pi^{\pm}$ at $44°$

Appendix D

General Gaussian Fits
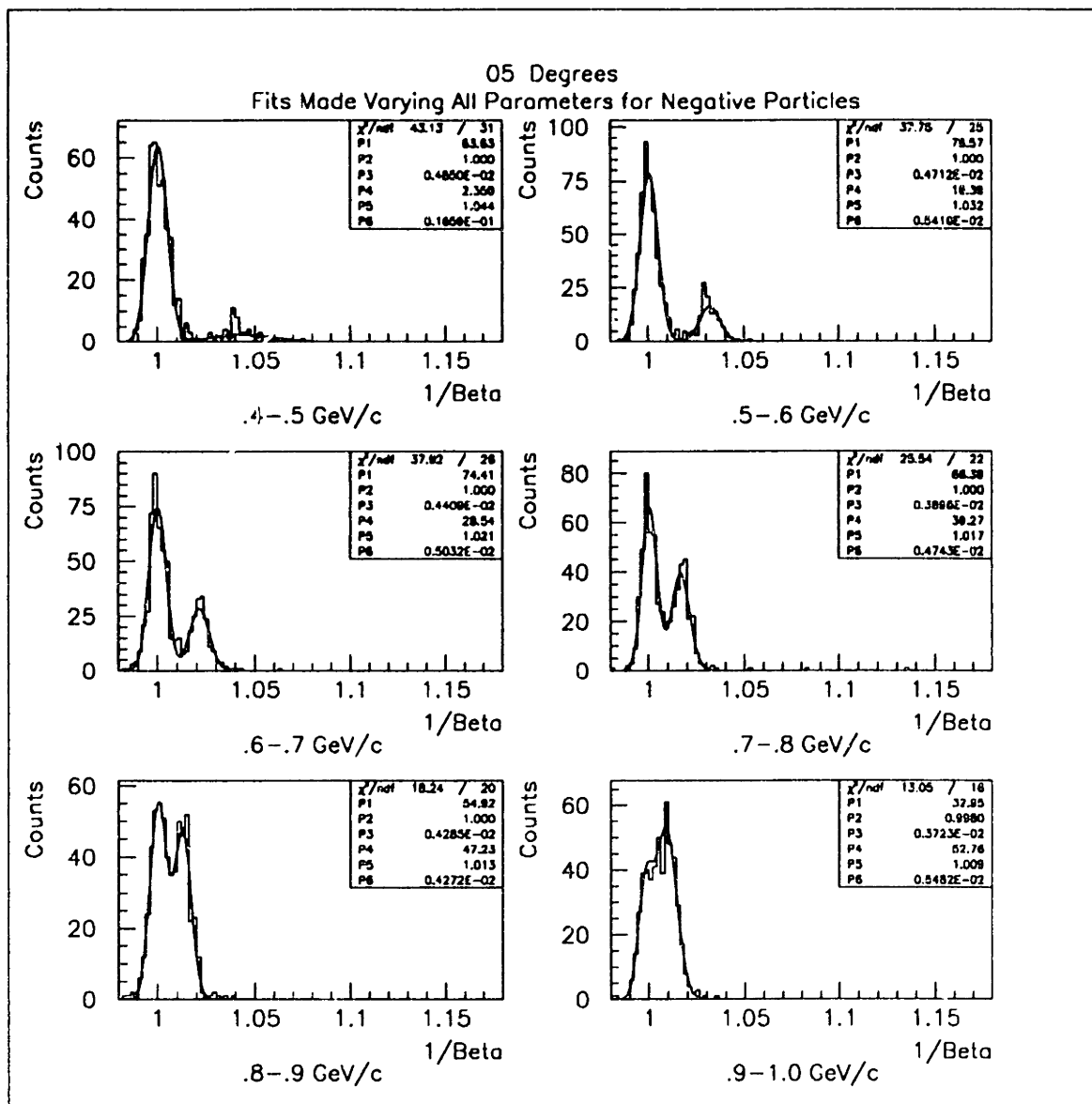
Figure D-1: General Gaussian Fits to Electrons and Negative Pions at 5°
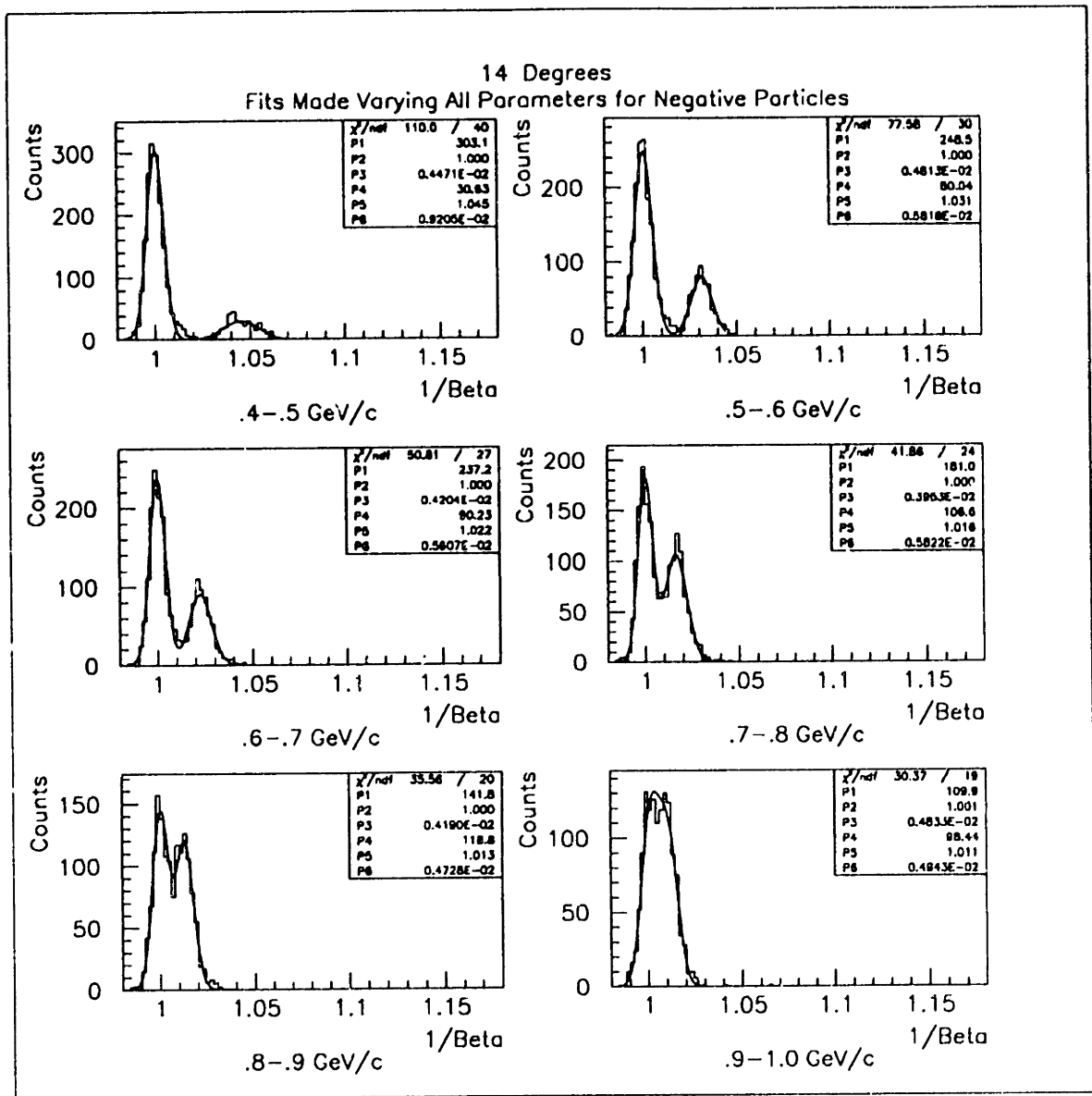
Figure D-2: General Gaussian Fits to Electrons and Negative Pions at 14°
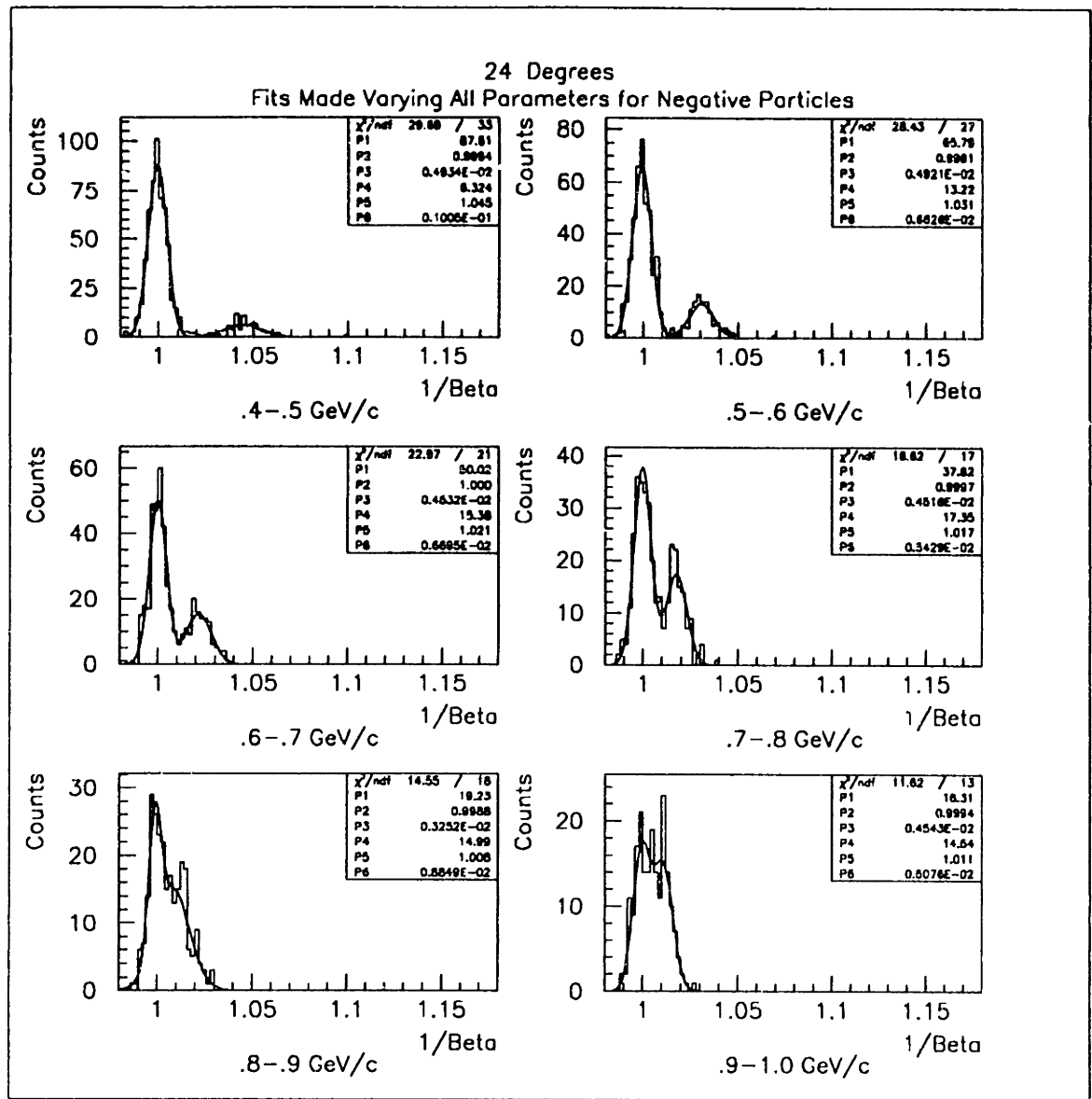
Figure D-3: General Gaussian Fits to Electrons and Negative Pions at 24°
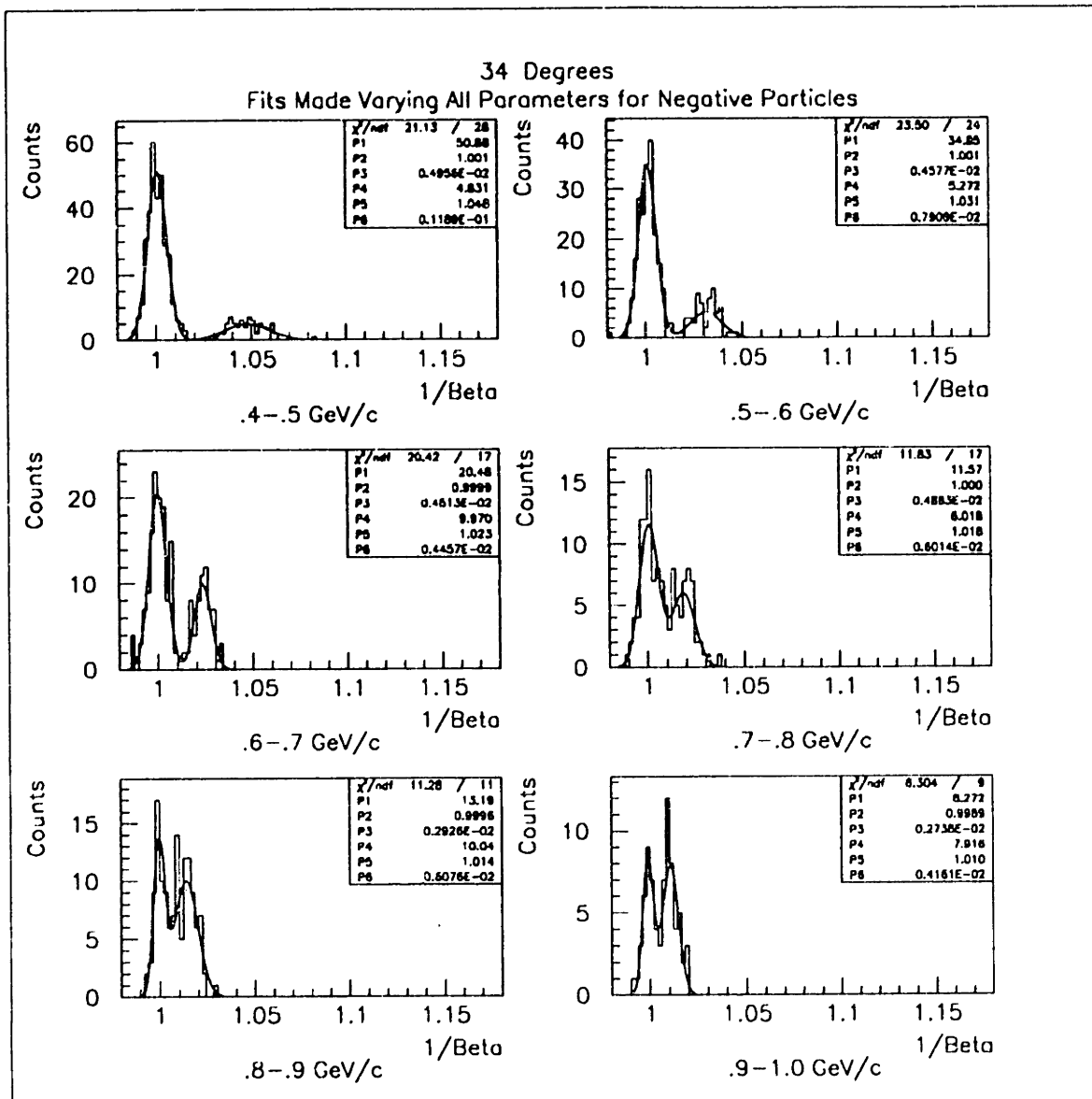
Figure D-4: General Gaussian Fits to Electrons and Negative Pions at 34°
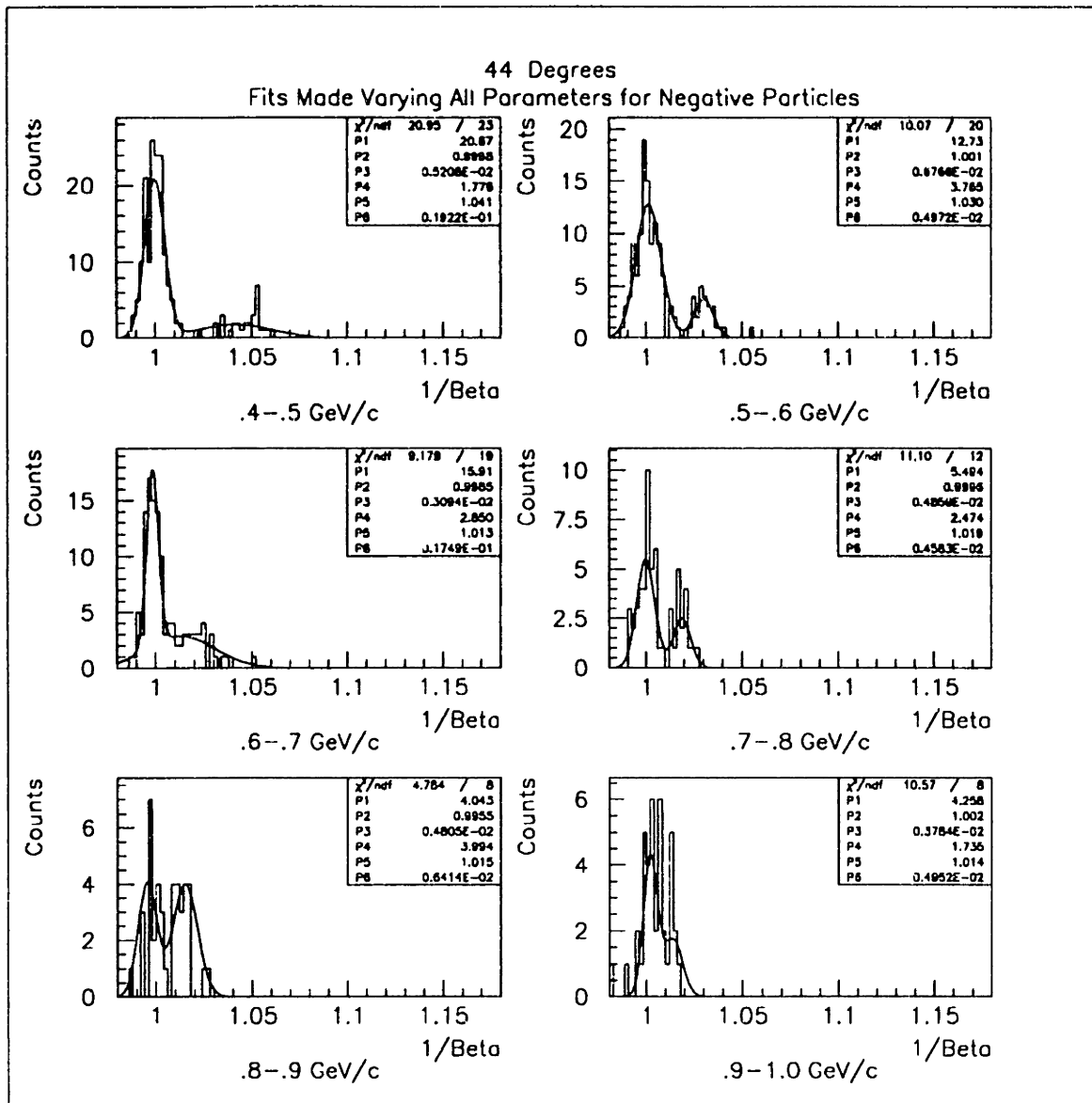
Figure D-5: General Gaussian Fits to Electrons and Negative Pions at 44°
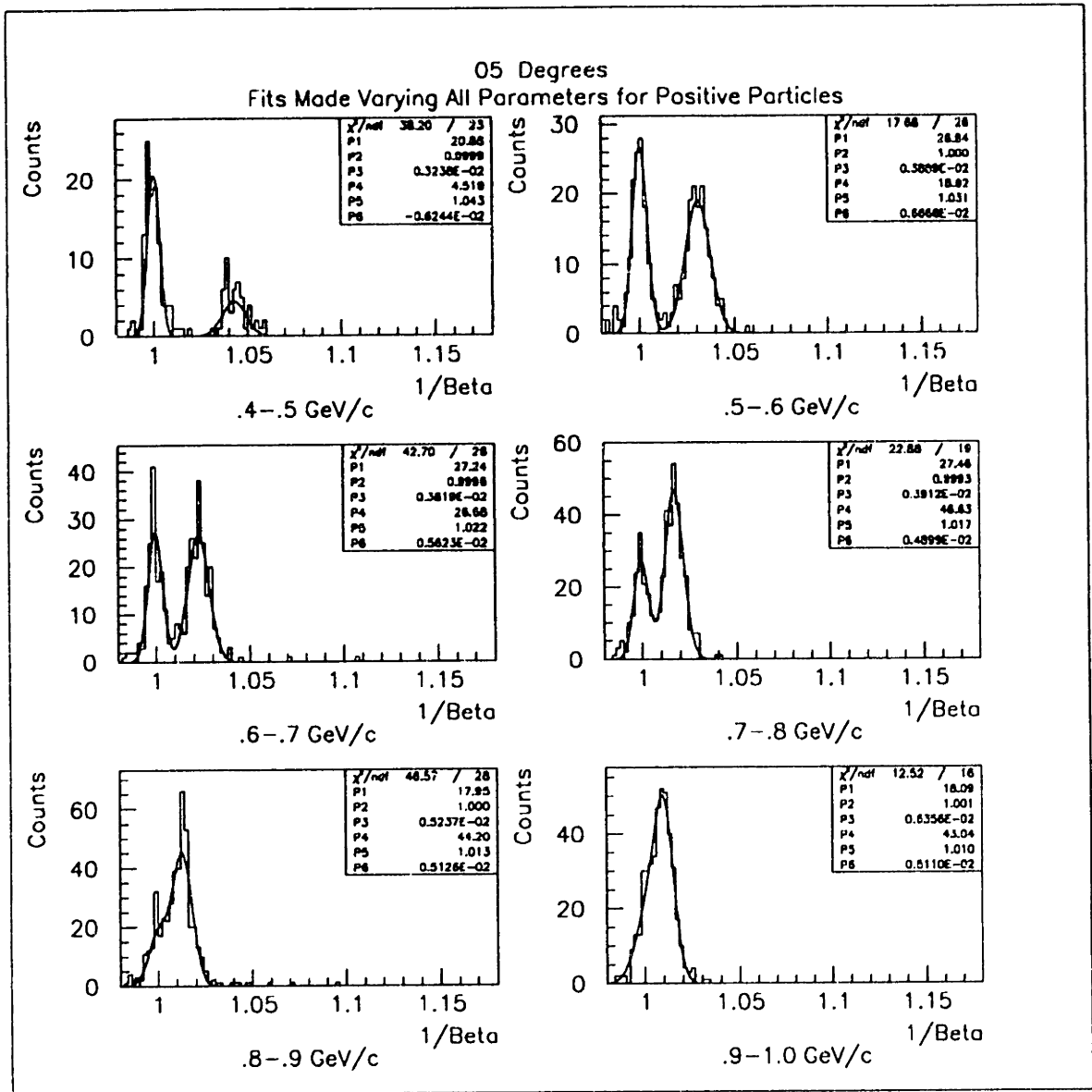
Figure D-6: General Gaussian Fits to Positrons and Positive Pions at 5°
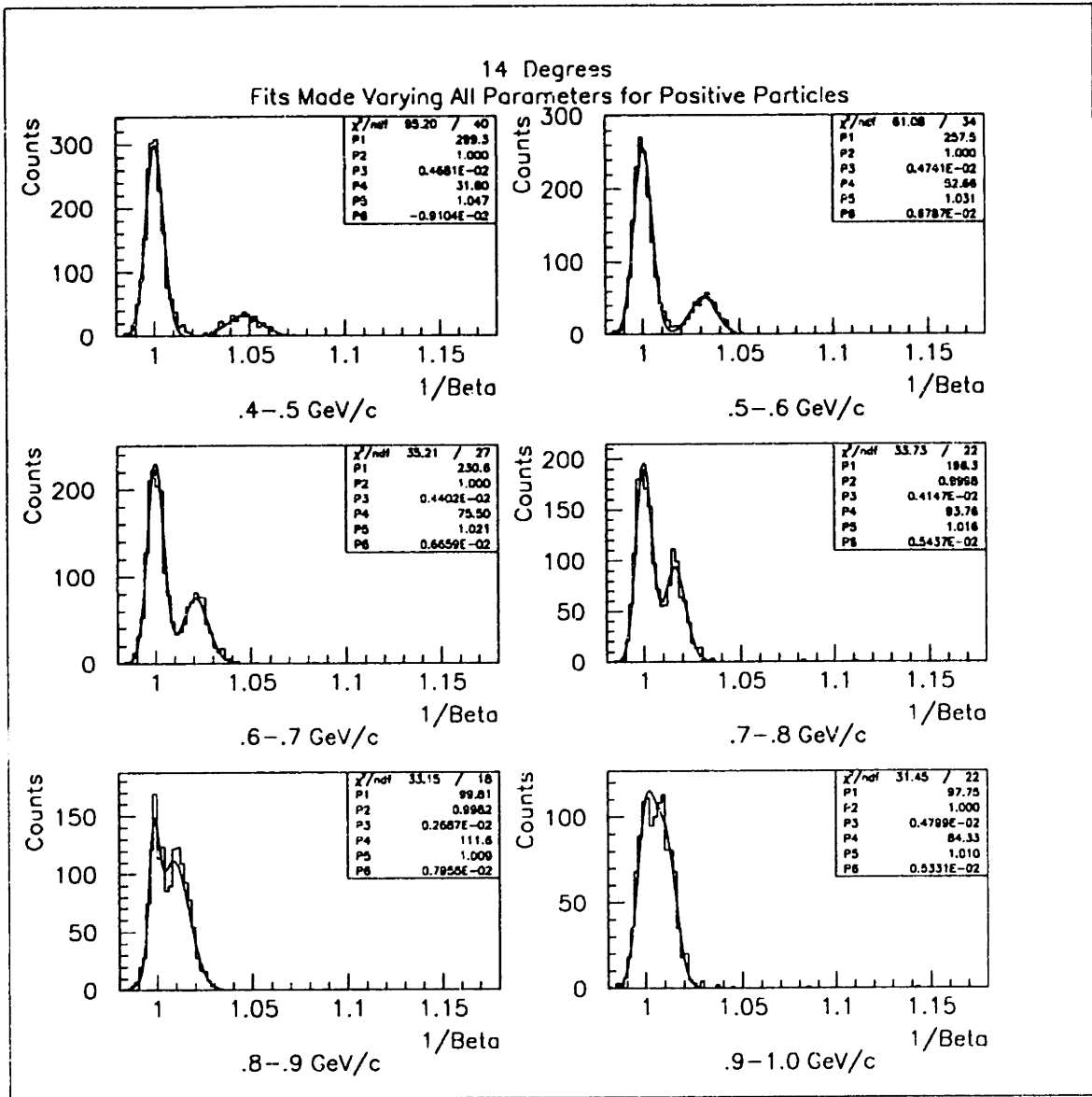
Figure D-7: General Gaussian Fits to Positrons and Positive Pions at 14°
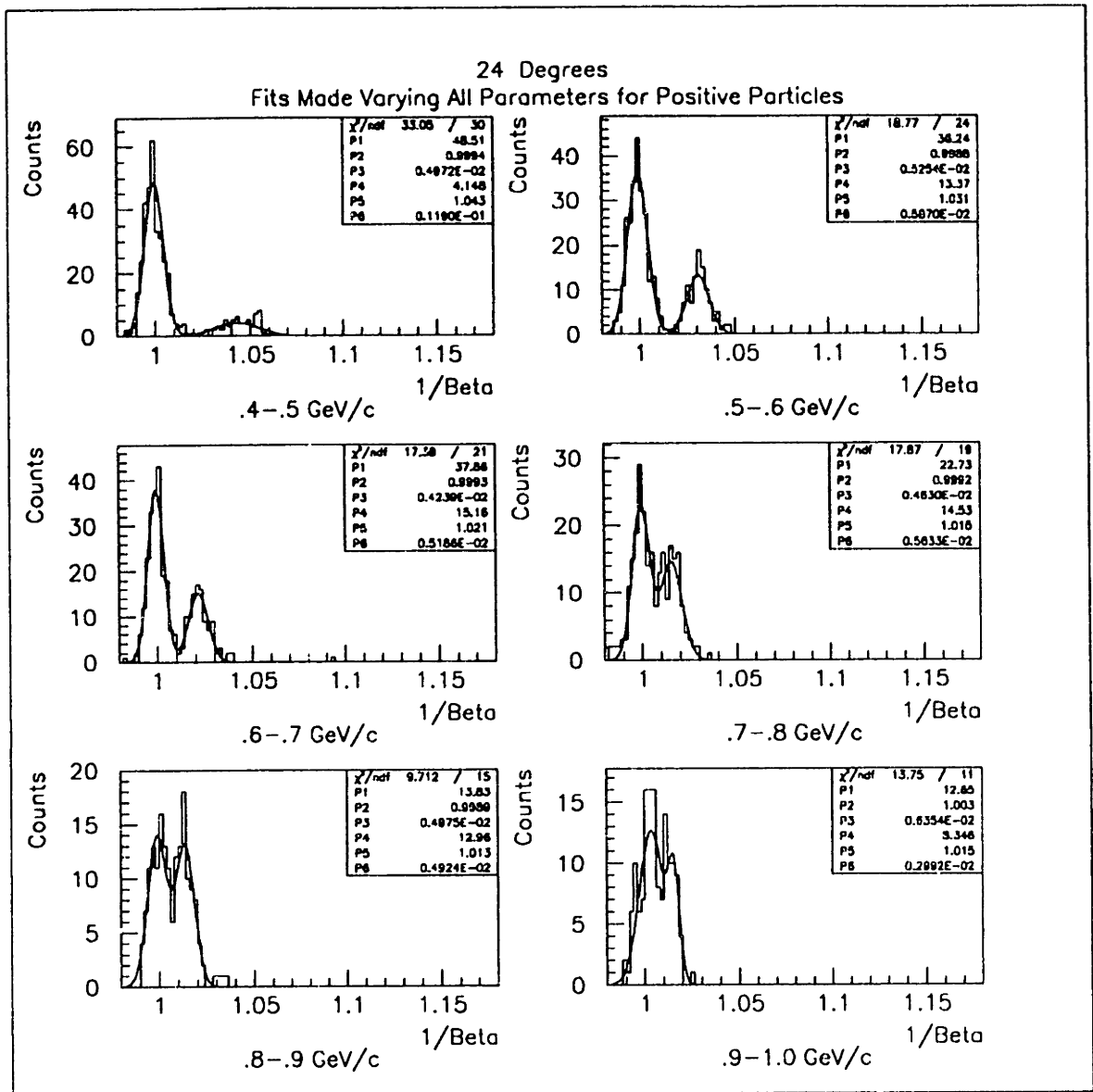
Figure D-8: General Gaussian Fits to Positrons and Positive Pions at 24°
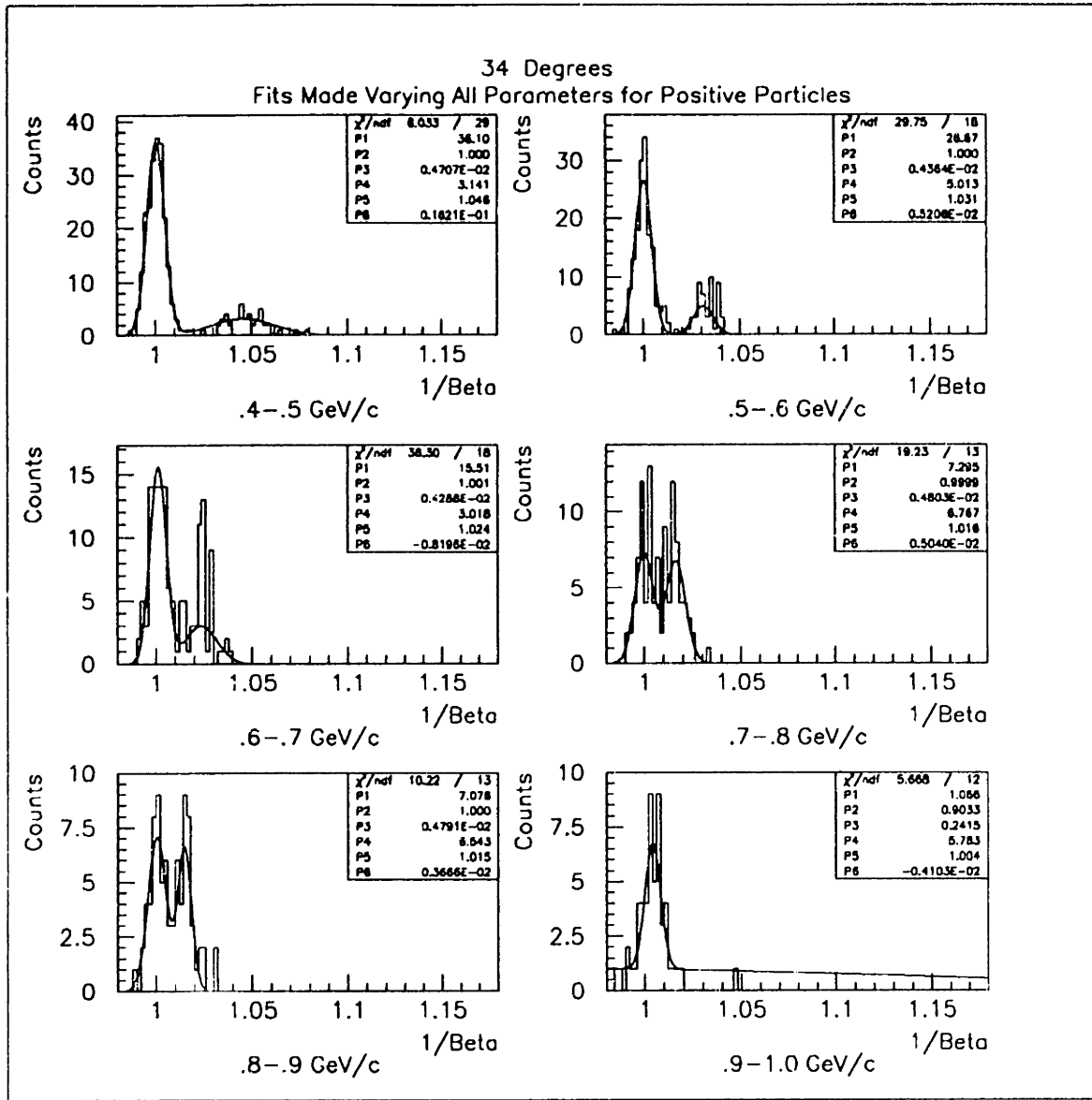
Figure D-9: General Gaussian Fits to Positrons and Positive Pions at 34°
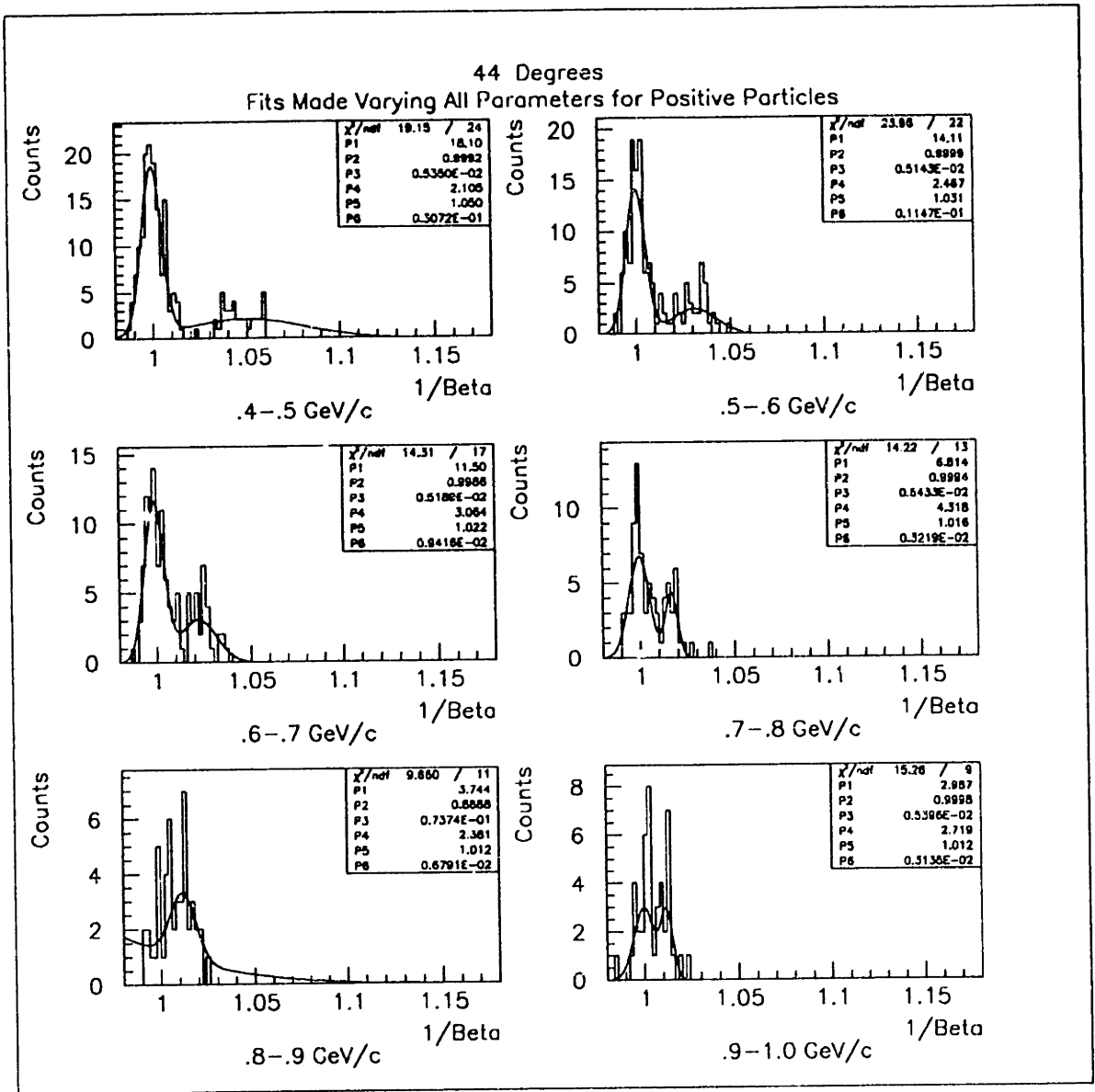
Figure D-10: General Gaussian Fits to Positrons and Positive Pions at 44°

95

Appendix E

Amplitude Gaussian Fits
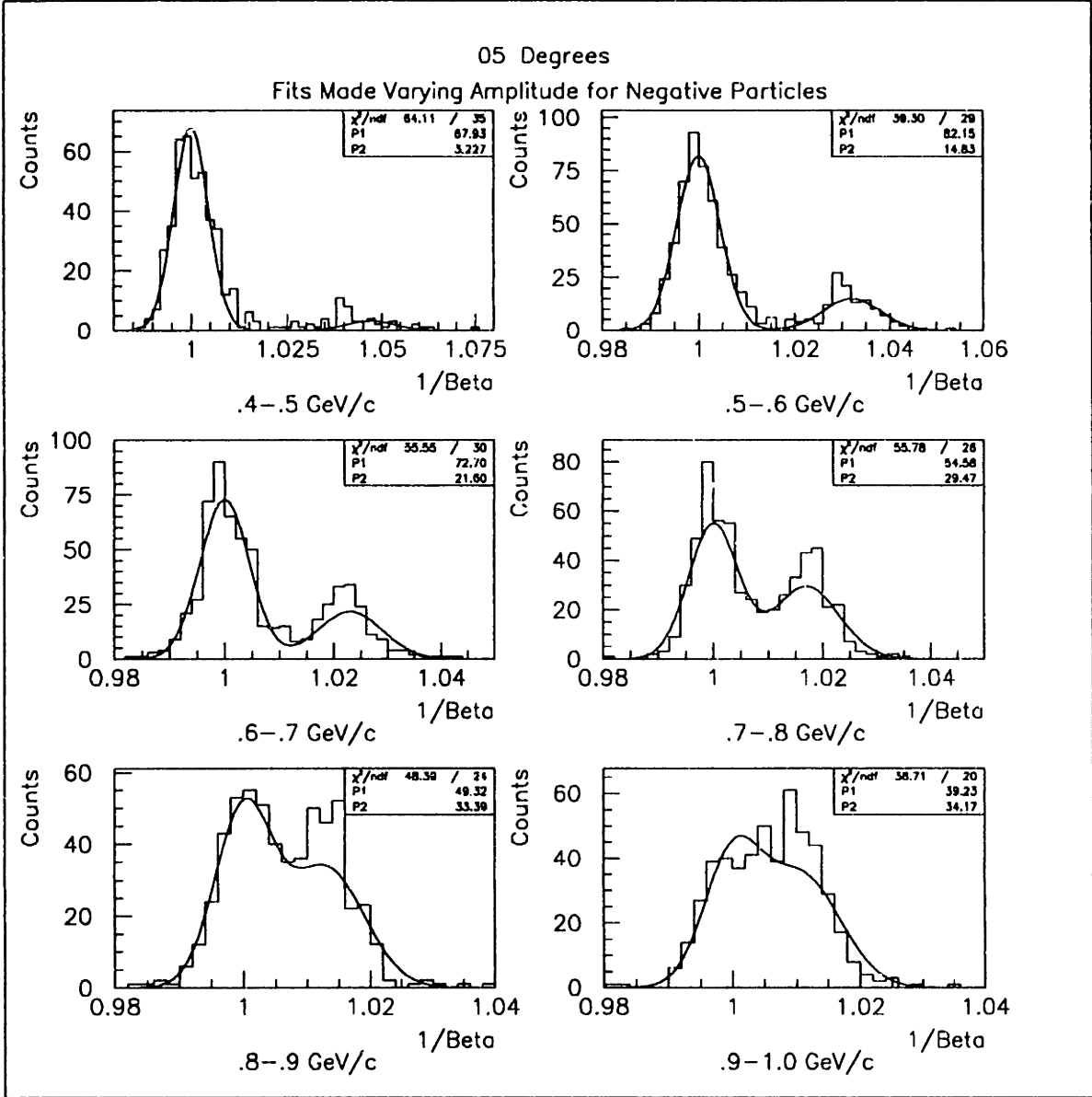
Figure E-1: Amplitude Gaussian Fits to Electrons and Negative Pions at 5°
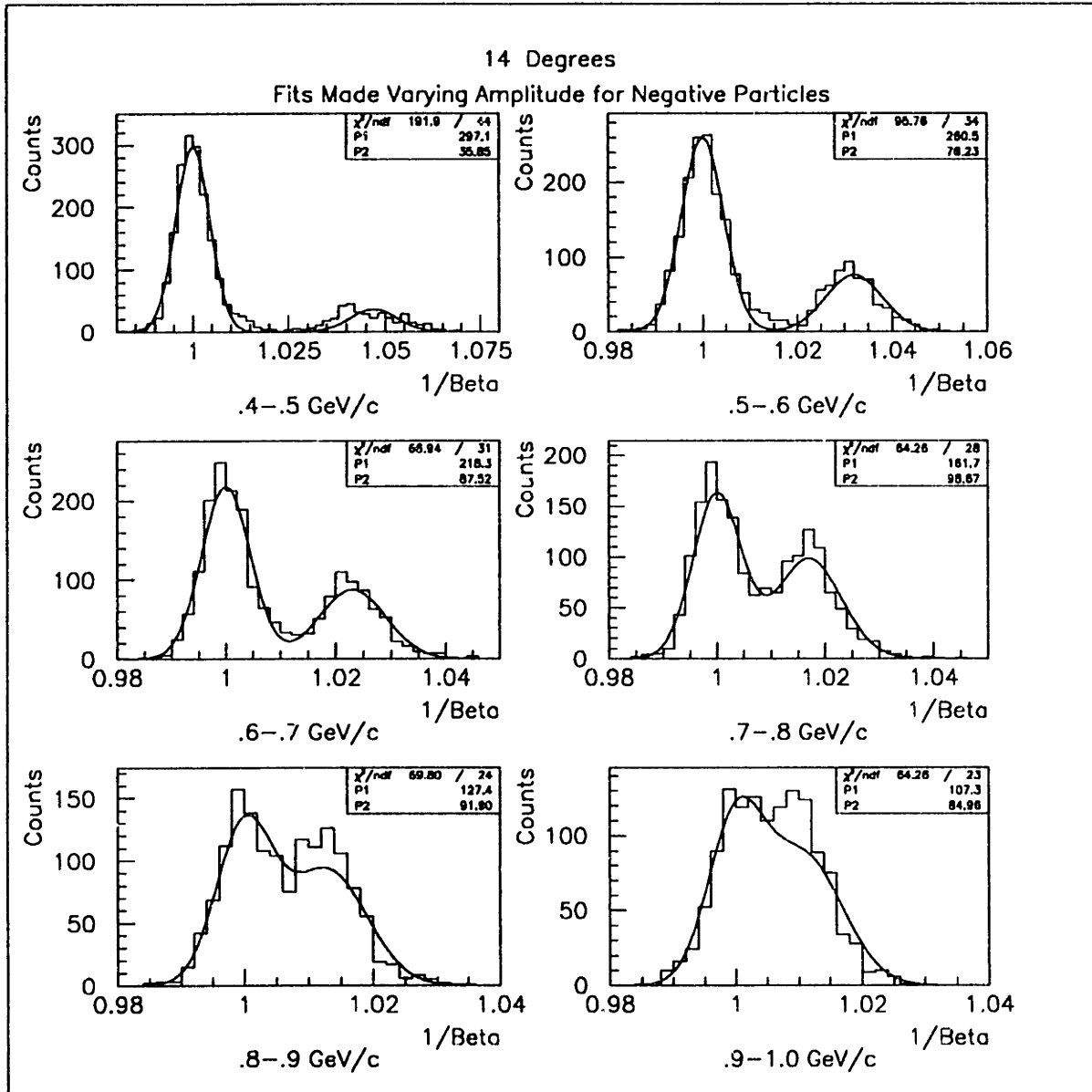
Figure E-2: Amplitude Gaussian Fits to Electrons and Negative Pions at 14°

99
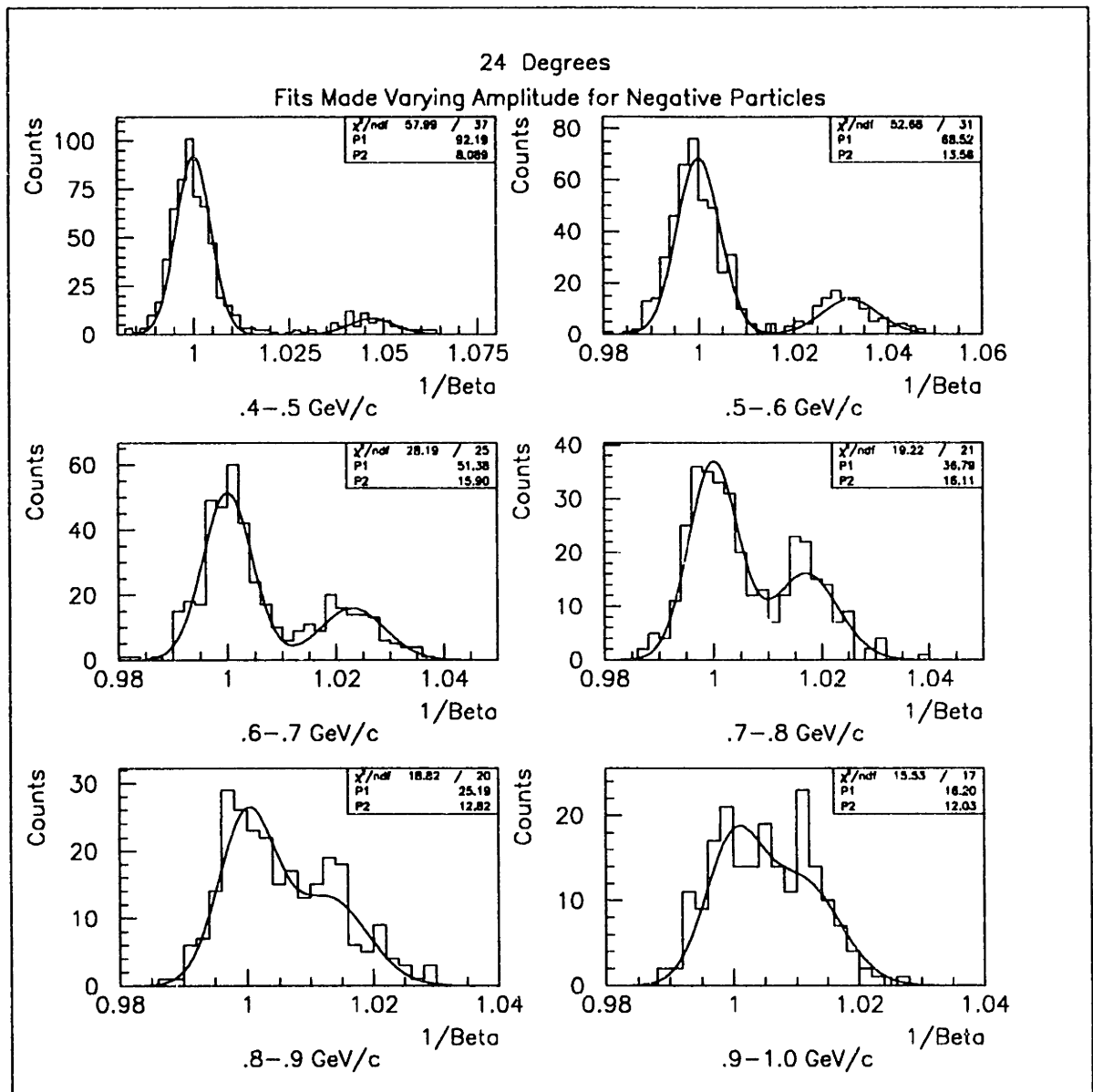
Figure E-3: Amplitude Gaussian Fits to Electrons and Negative Pions at 24°
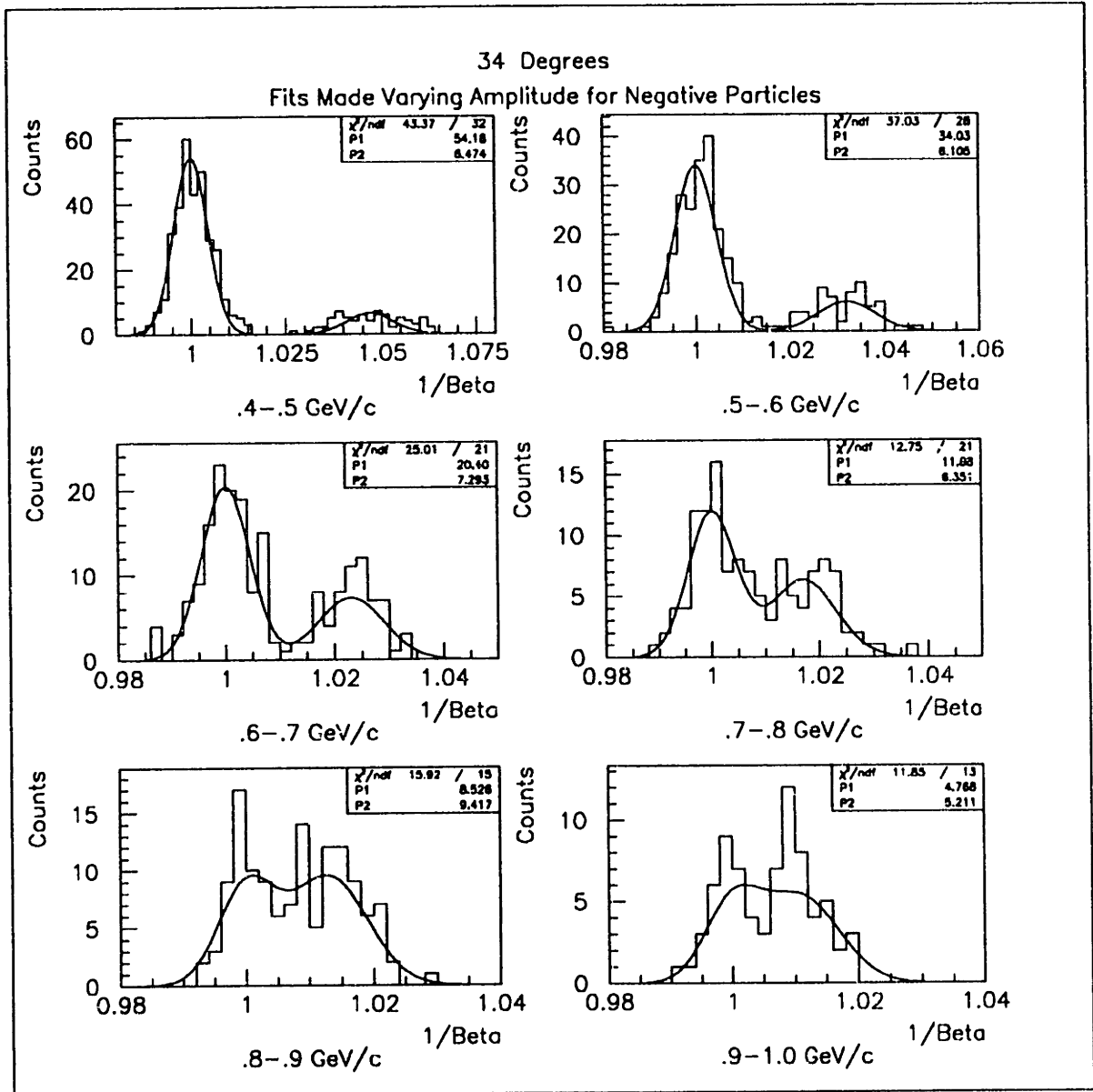
Figure E-4: Amplitude Gaussian Fits to Electrons and Negative Pions at 34°
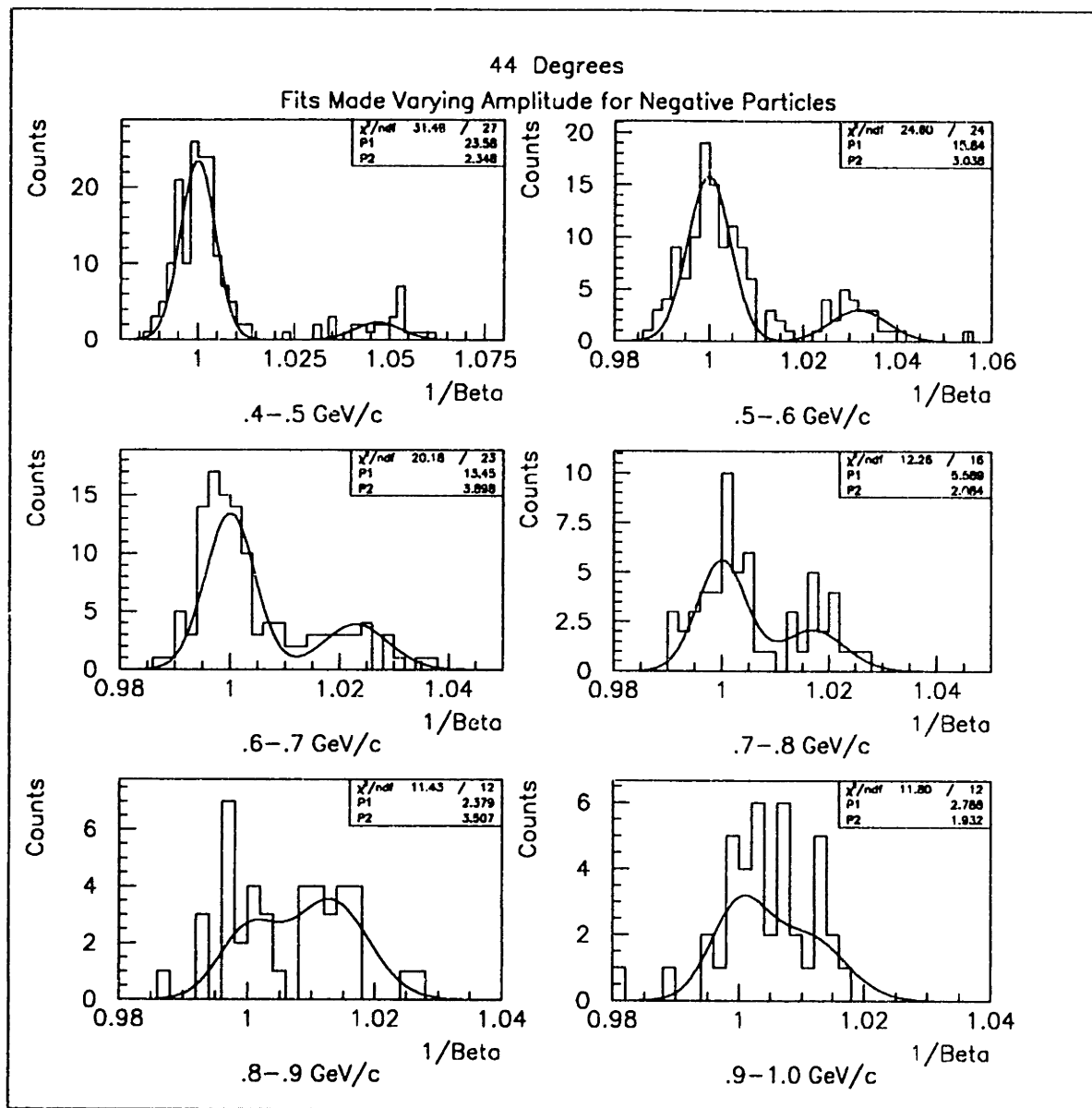
Figure E-5: Amplitude Gaussian Fits to Electrons and Negative Pions at 44°
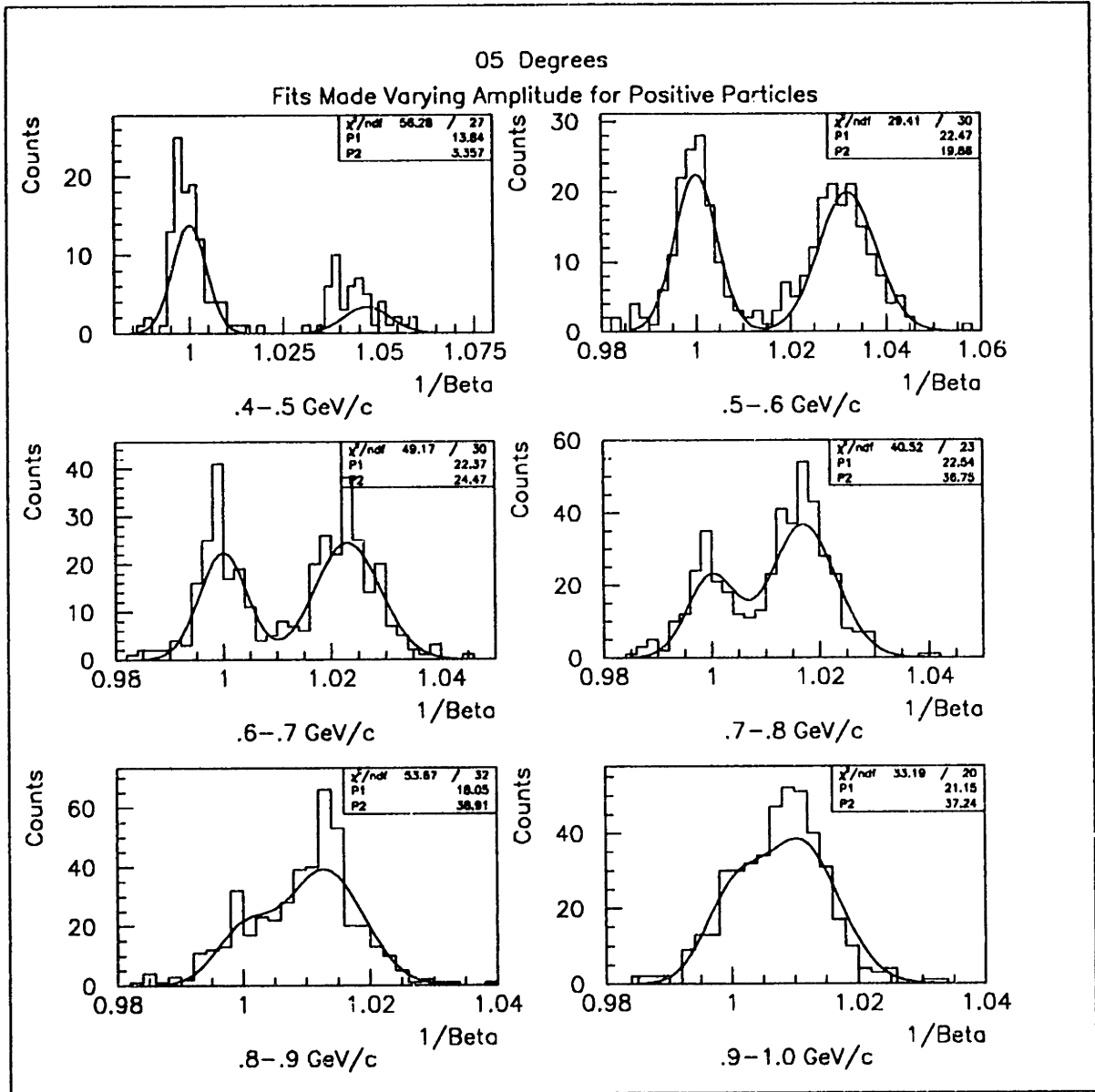
Figure E-6: Amplitude Gaussian Fits to Positrons and Positive Pions at 5°
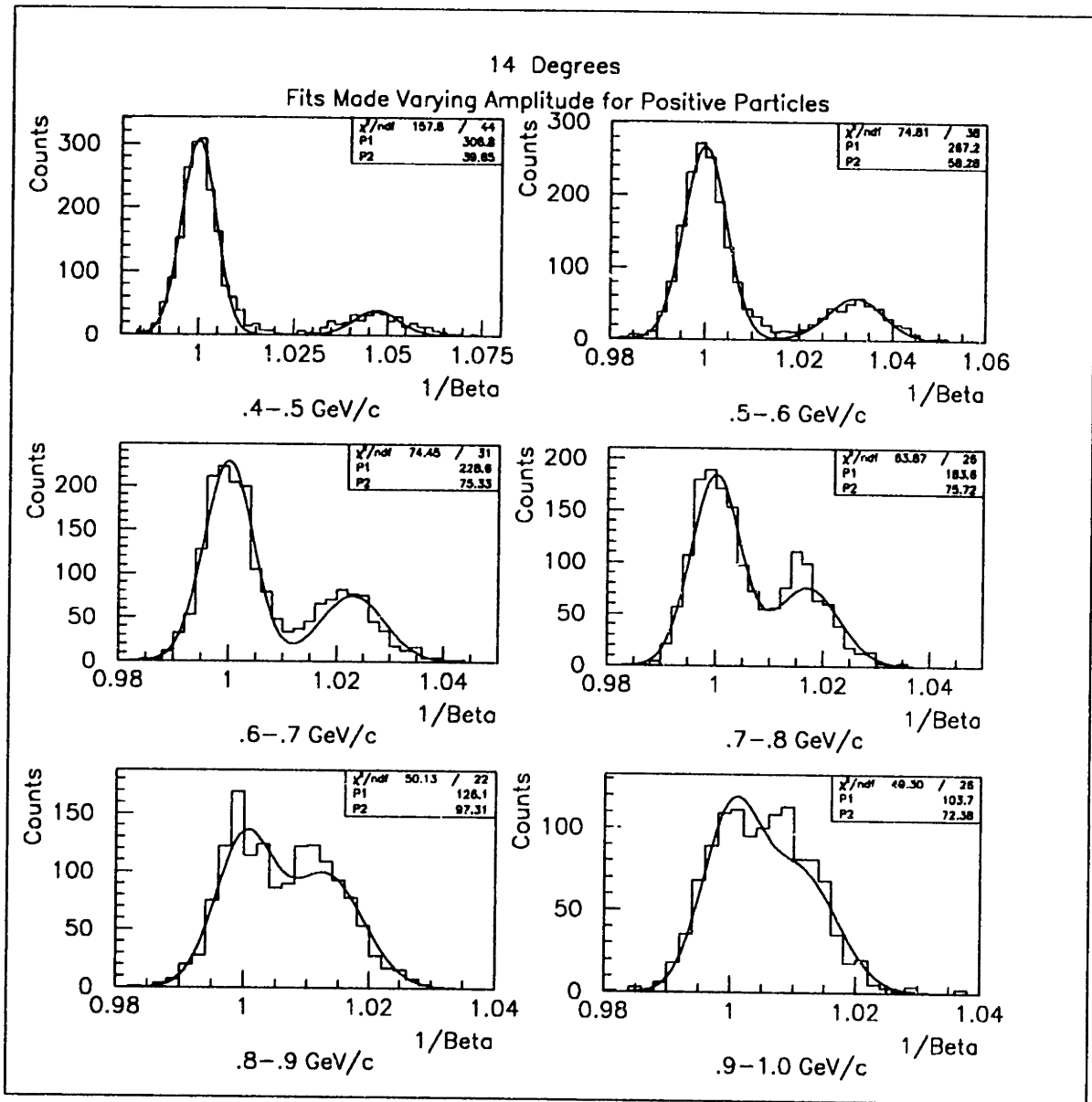
Figure E-7: Amplitude Gaussian Fits to Positrons and Positive Pions at 14°
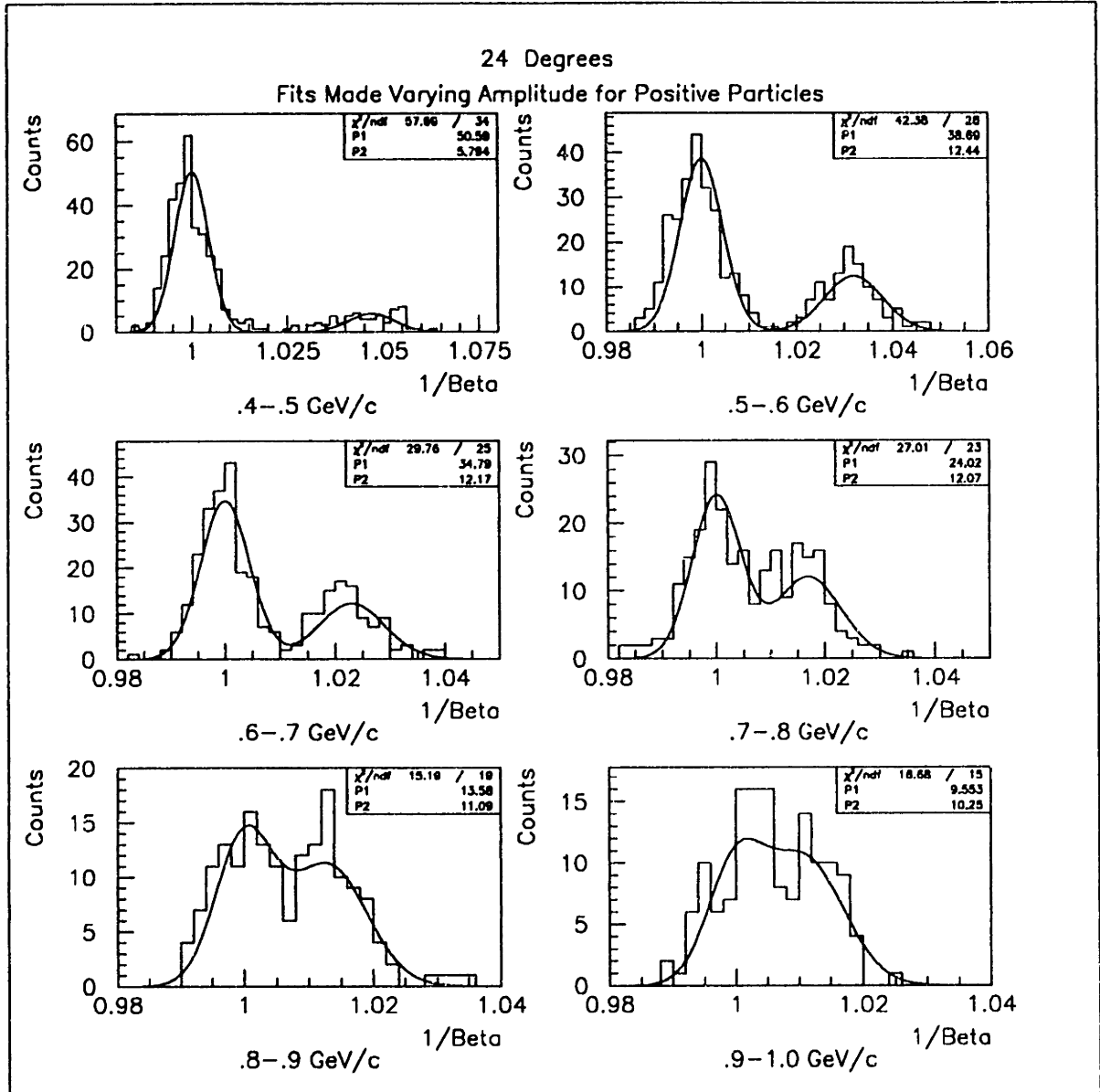
Figure E-8: Amplitude Gaussian Fits to Positrons and Positive Pions at 24°
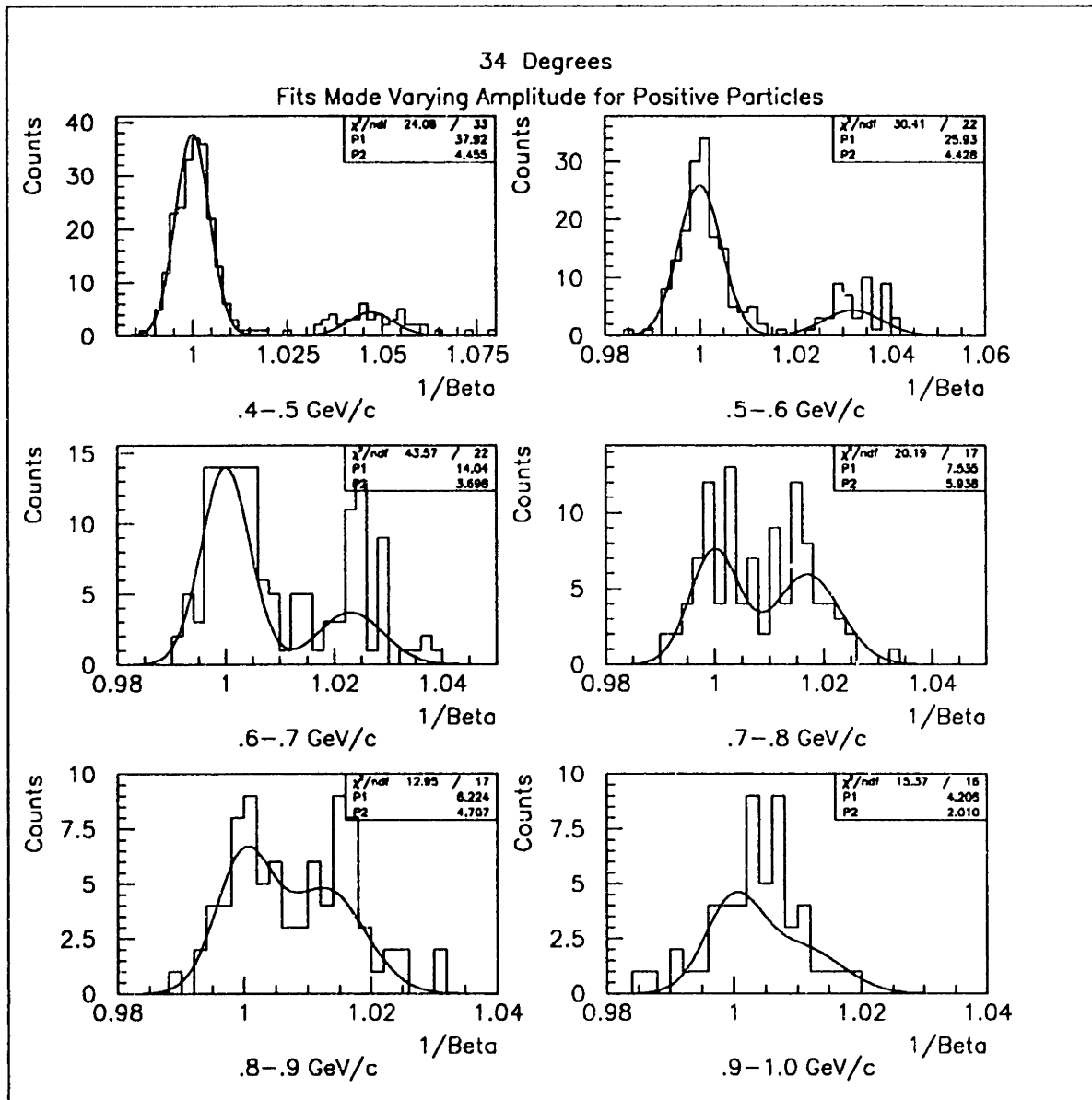
Figure E-9: Amplitude Gaussian Fits to Positrons and Positive Pions at 34°
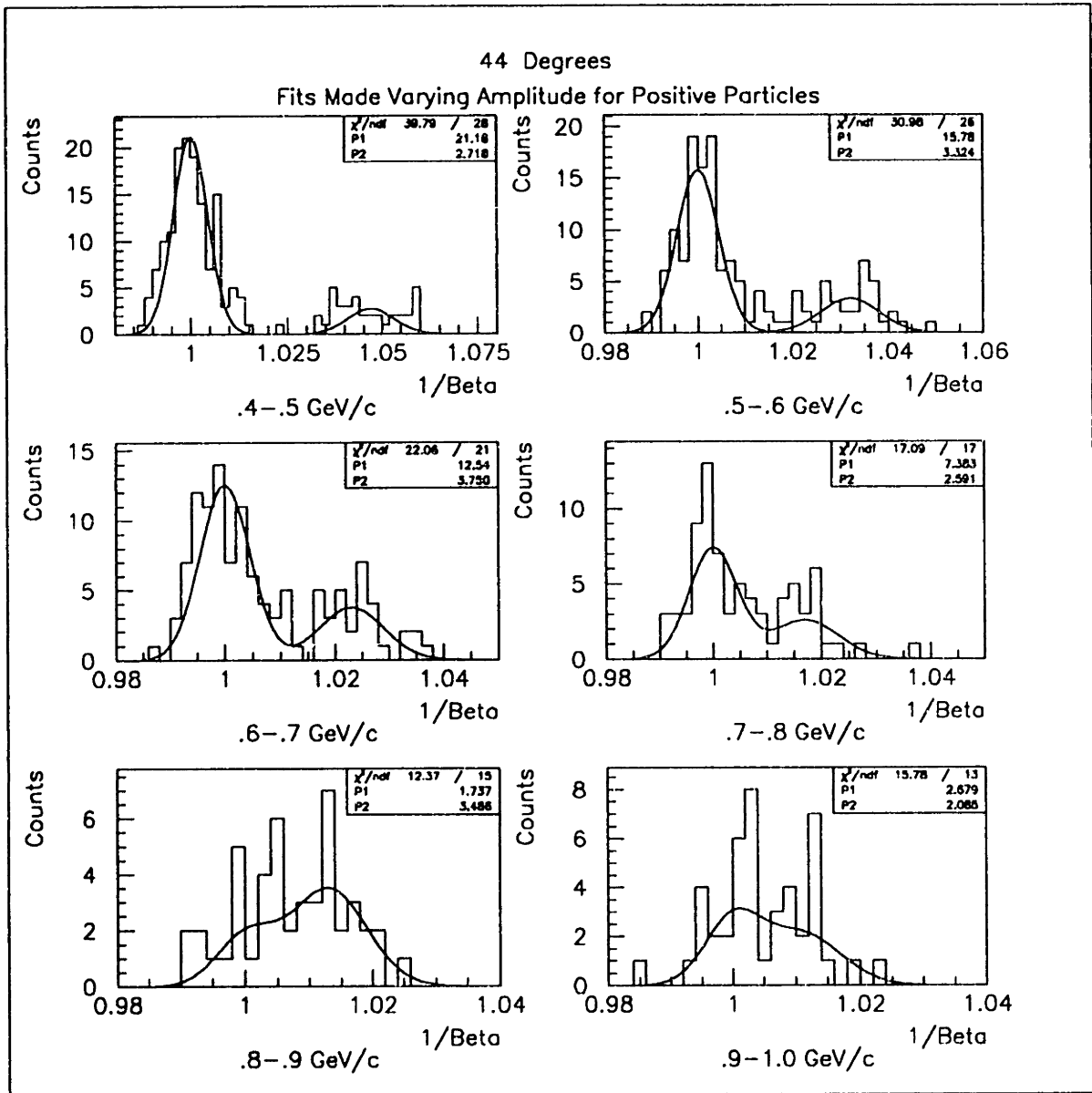
Figure E-10: Amplitude Gaussian Fits to Positrons and Positive Pions at 44°

Appendix F

Fitted Gaussian Means for $\pi^{\pm}$ and Sigmas for $\pi^{\pm}$ and $e^{\pm}$
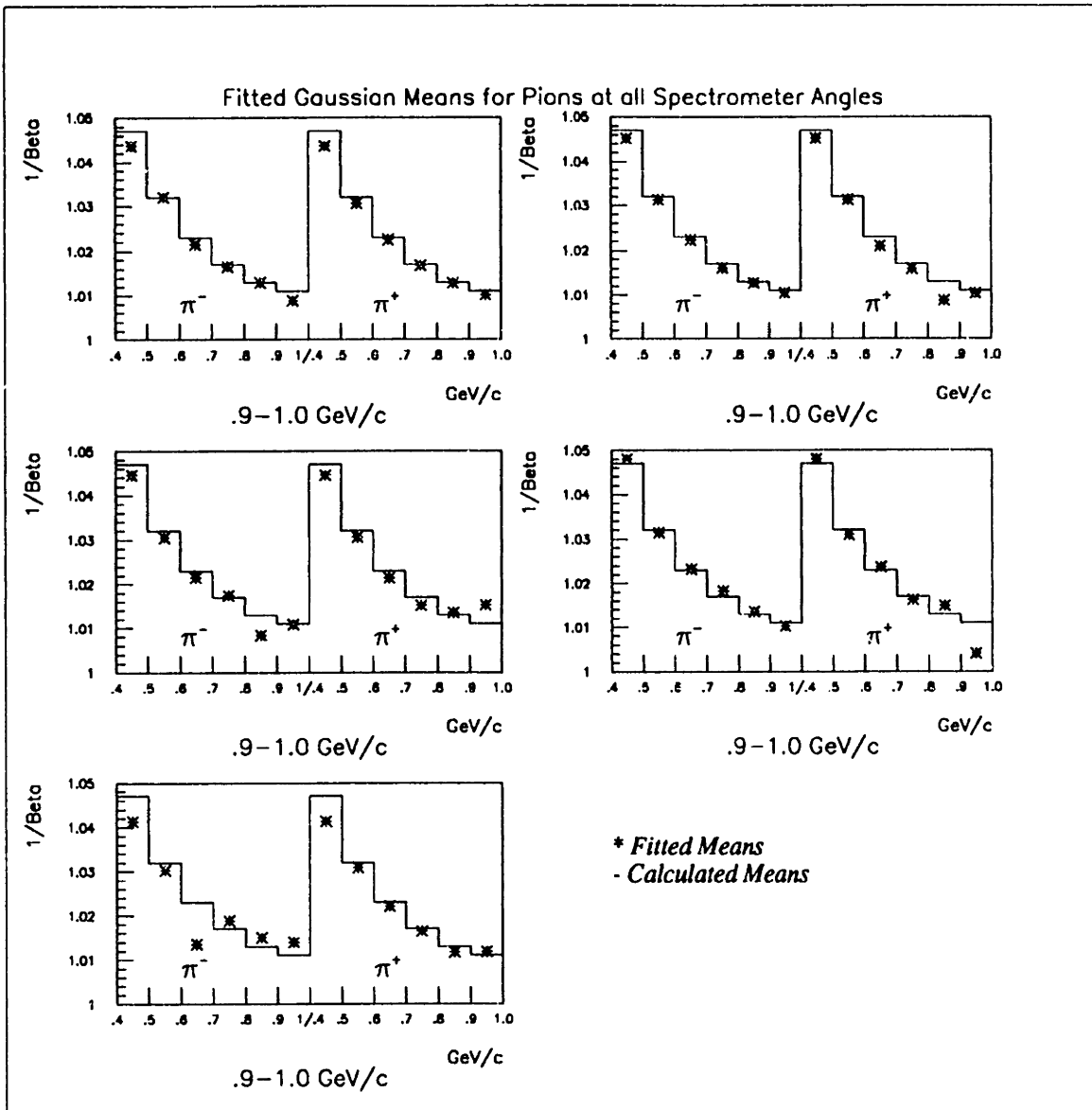
Figure F-1: Fitted Gaussian Means of $\pi^{\pm}$
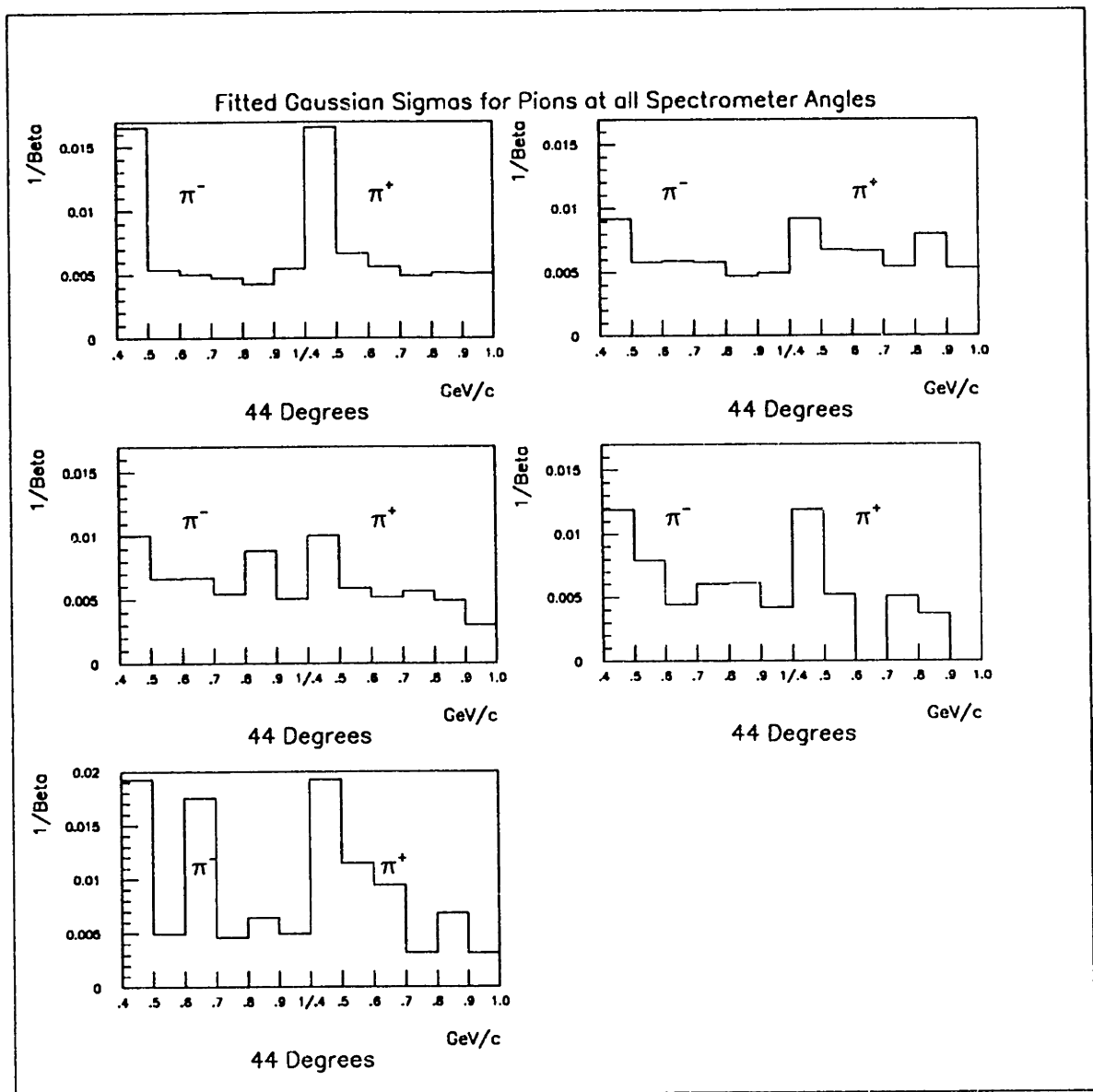
Figure F-2: Fitted Gaussian Sigmas of $\pi^\pm$
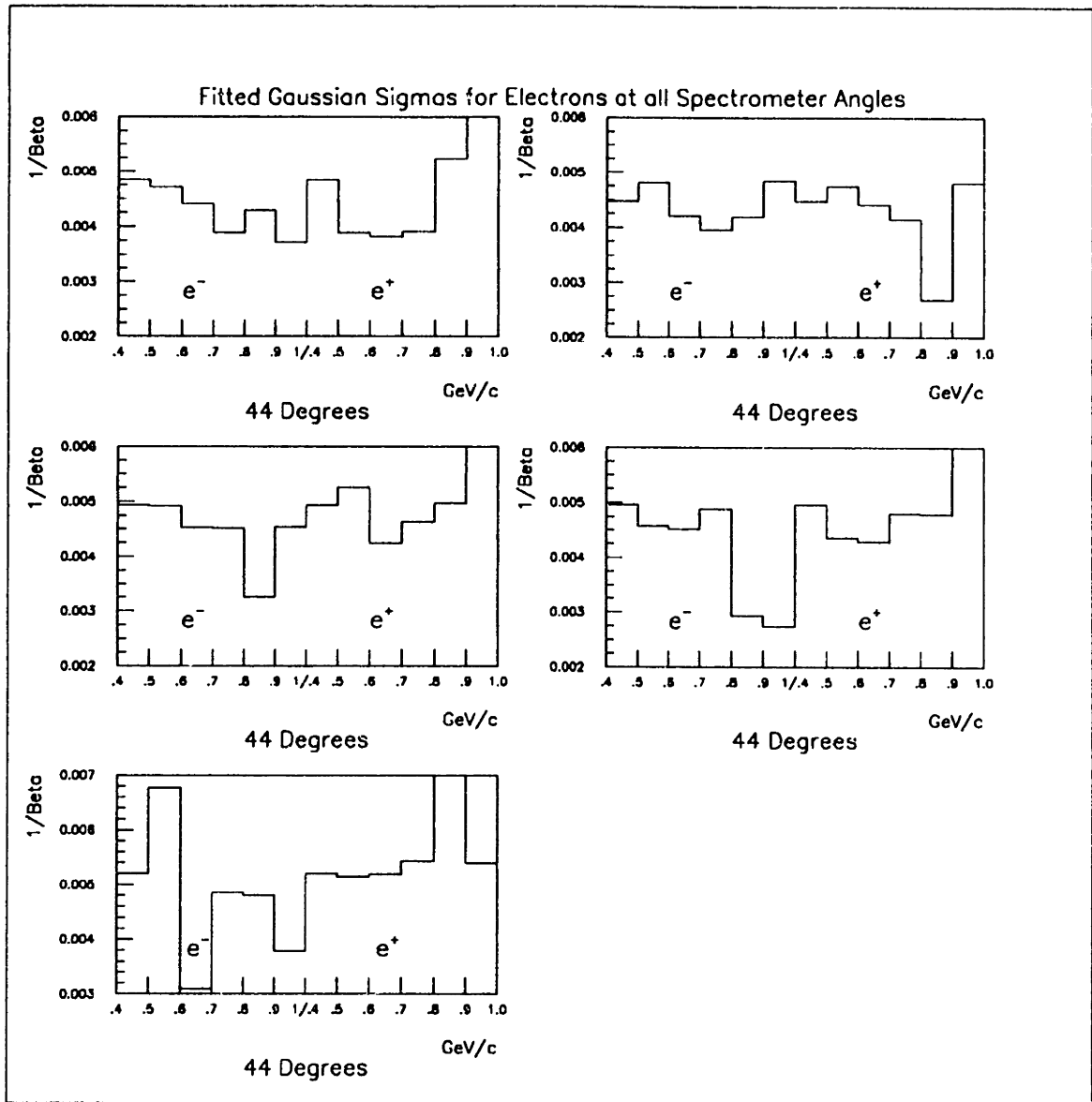
Figure F-3: Fitted Gaussian Sigmas of $e^{\pm}$

Appendix G

Comparisons of Gaussian Integrals to Bin Summation Counts
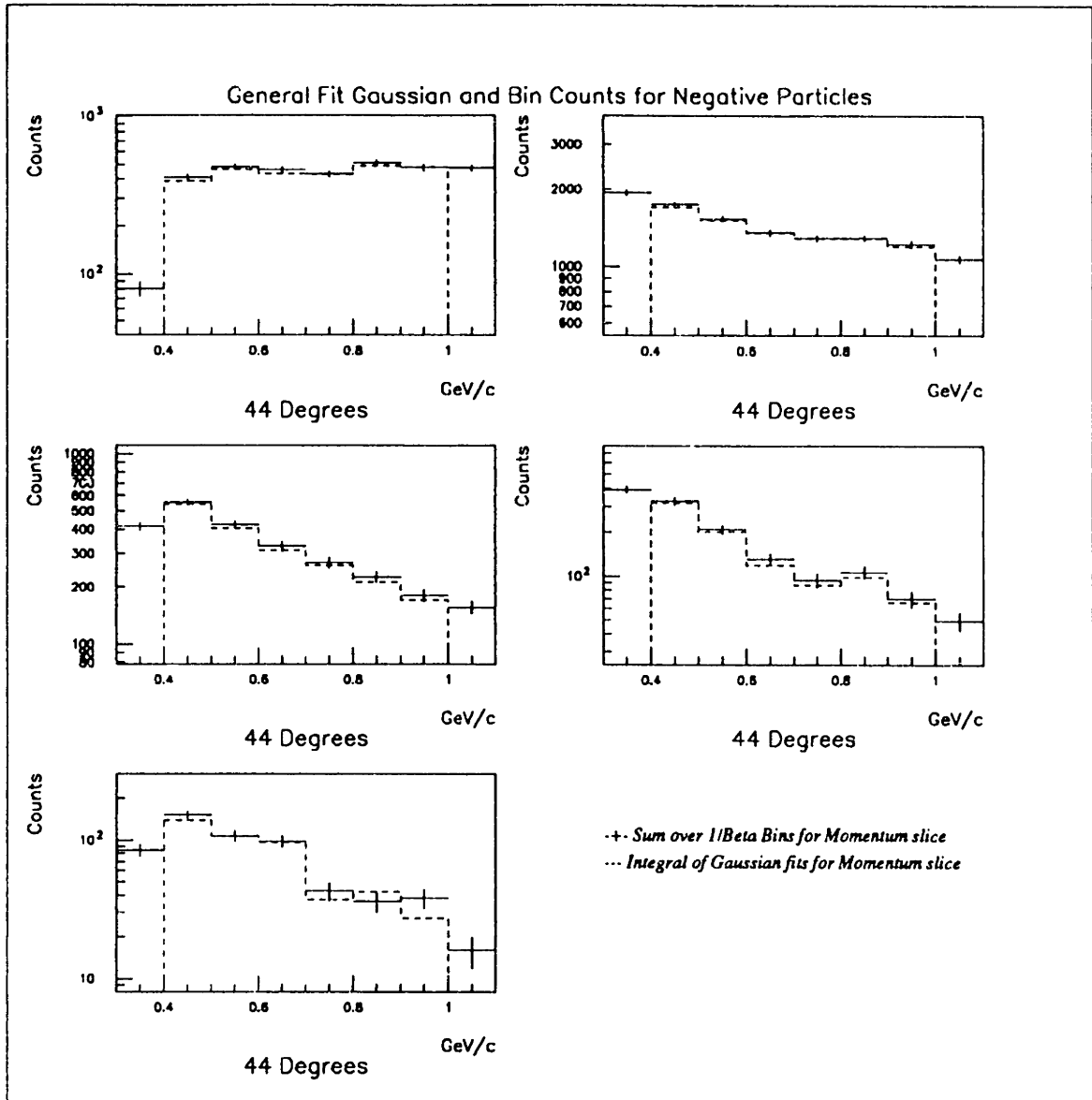
Figure G-1: General Gaussian Integrals and Bin Sums for Electrons and Negative Pions
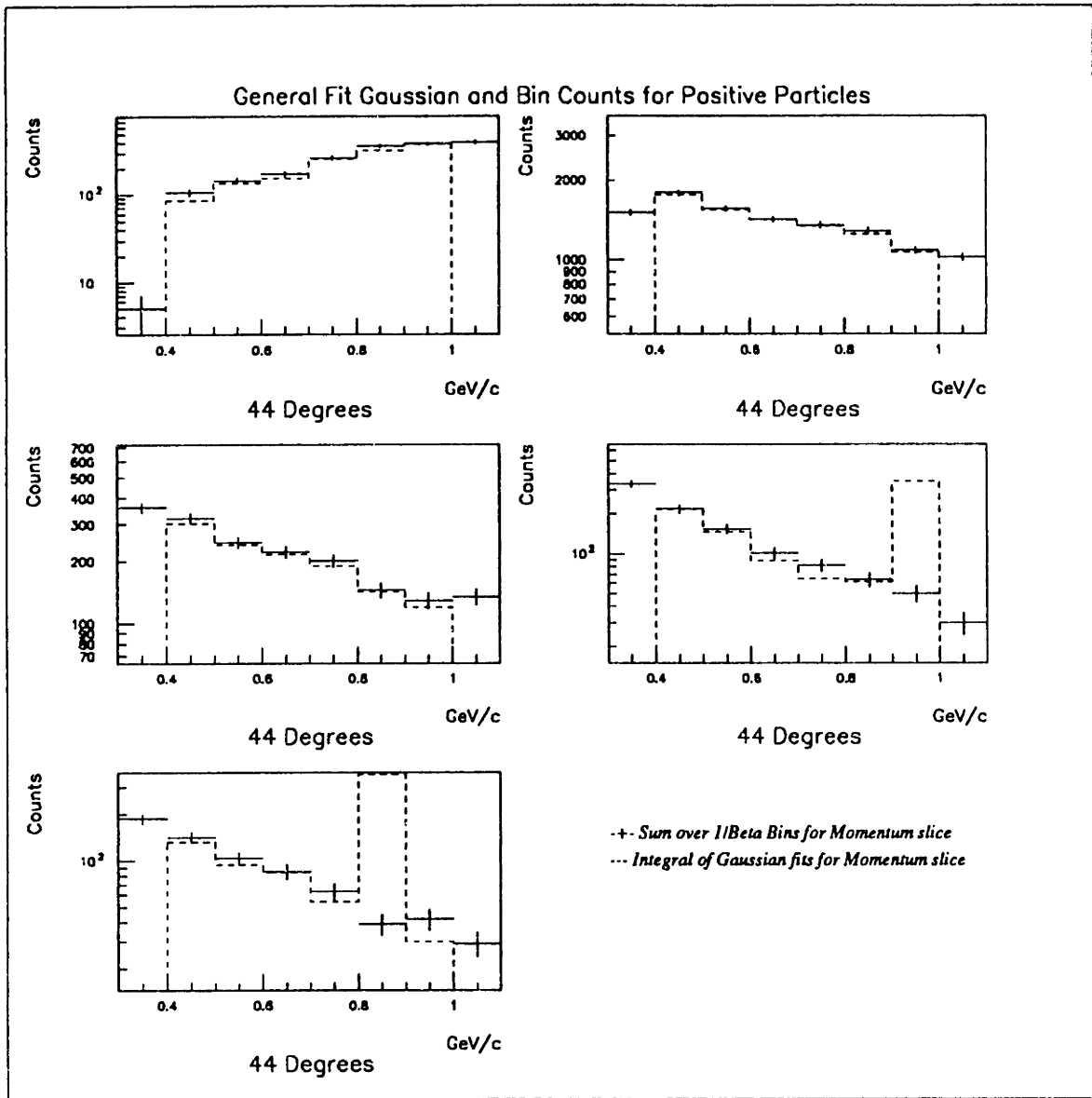
Figure G-2: General Gaussian Integrals and Bin Sums for Positrons and Positive Pions
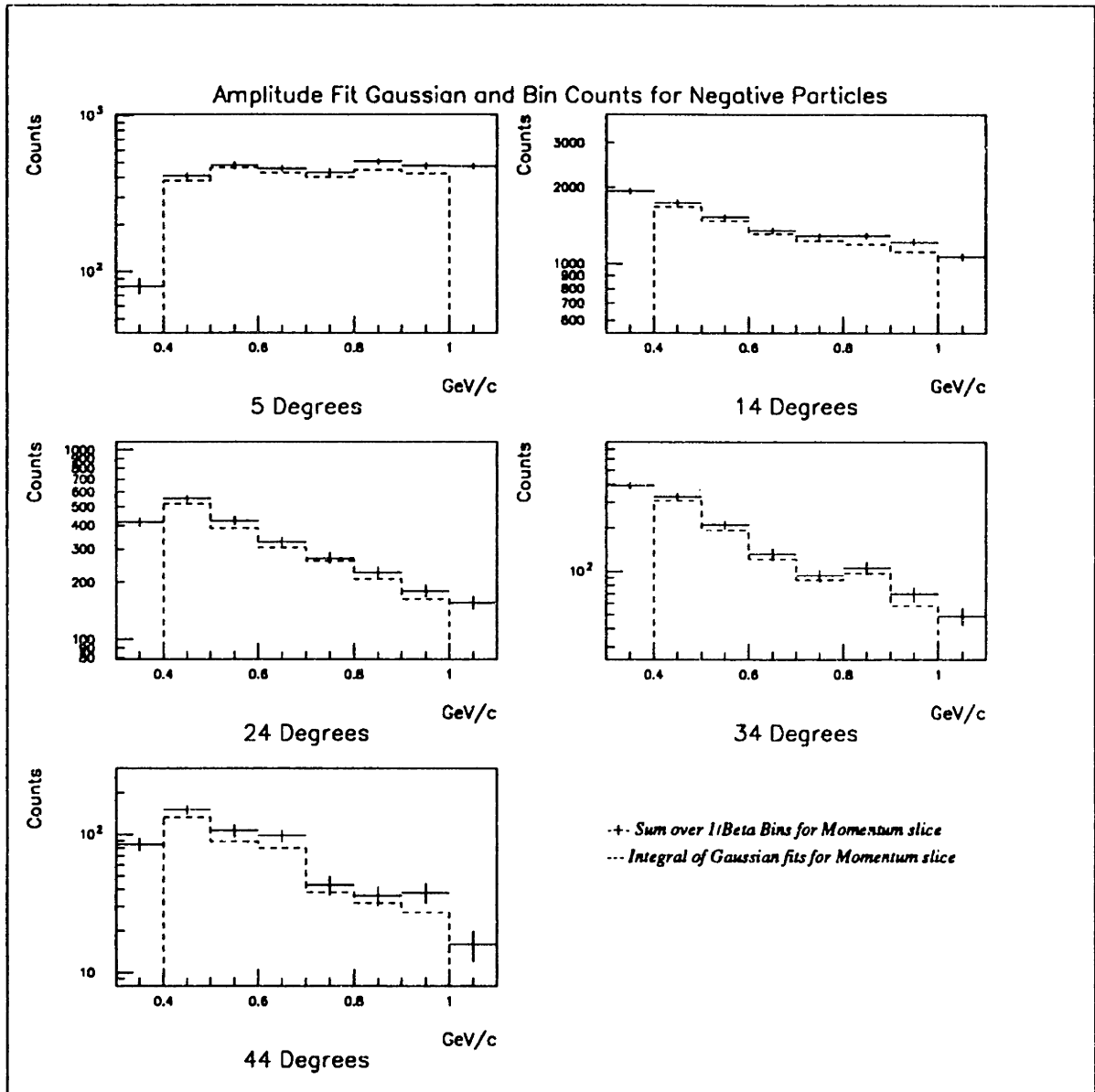
Figure G-3: Amplitude Gaussian Integrals and Bin Sums for Electrons and Negative Pions

116
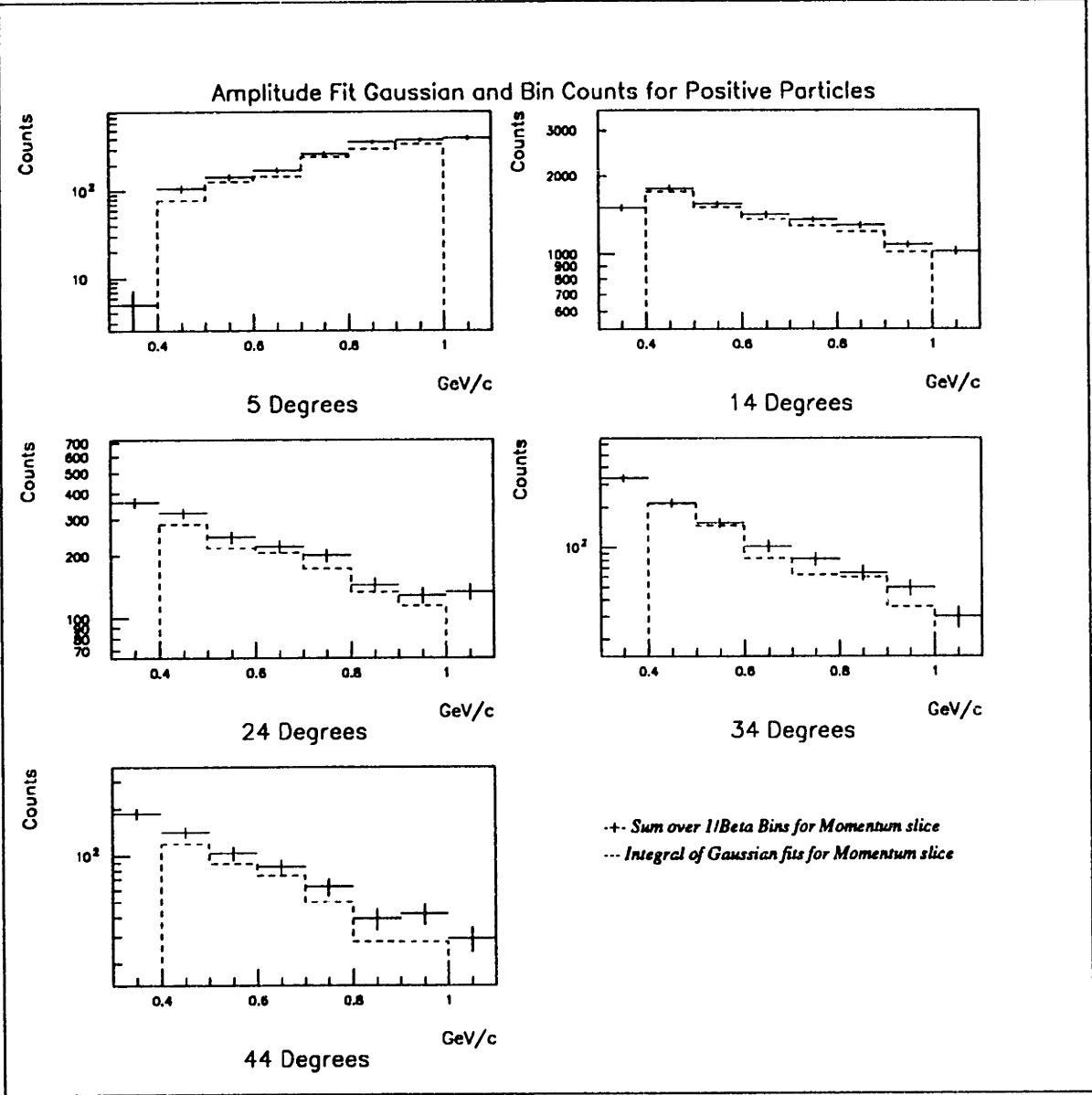
Figure G-4: General Gaussian Integrals and Bin Sums for Positrons and Positive Pions

Appendix H

Fractional Pion Contamination of $e^{\pm}$
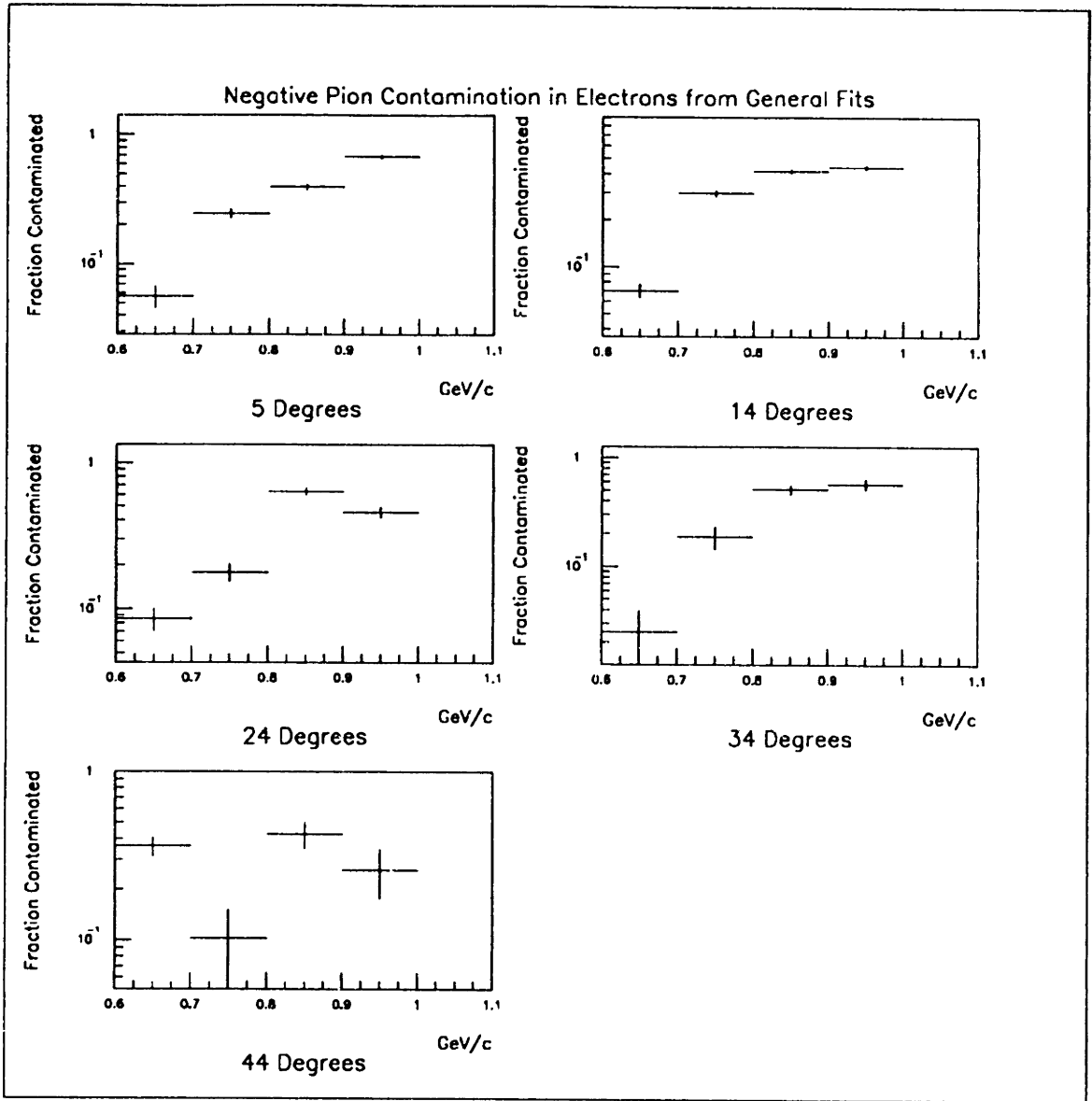
Figure H-1: Fractional Negative Pion Contamination of Electrons from General Gaussian Fits
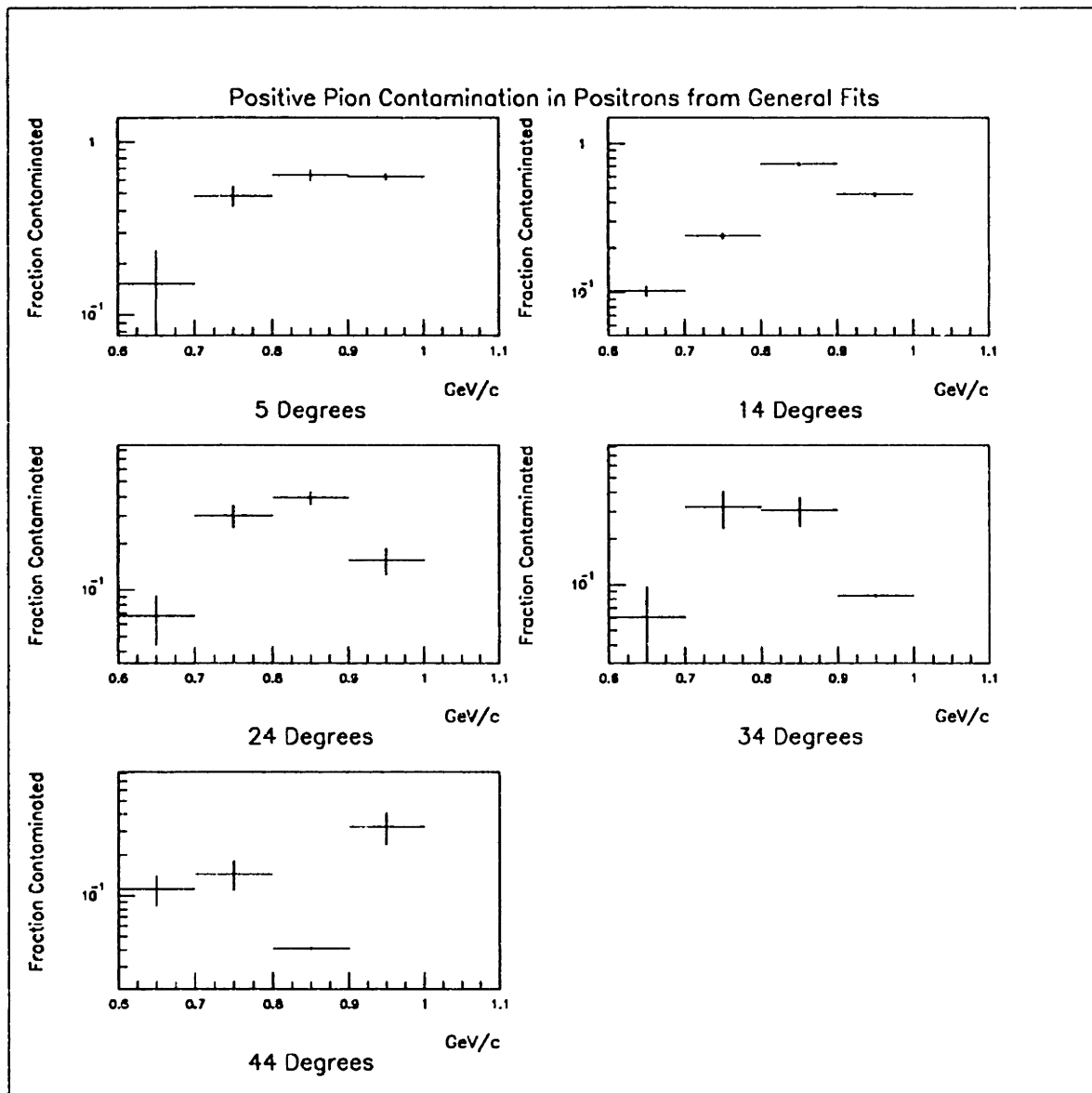
Figure H-2: Fractional Positive Pion Contamination of Positrons from General Gaussian Fits
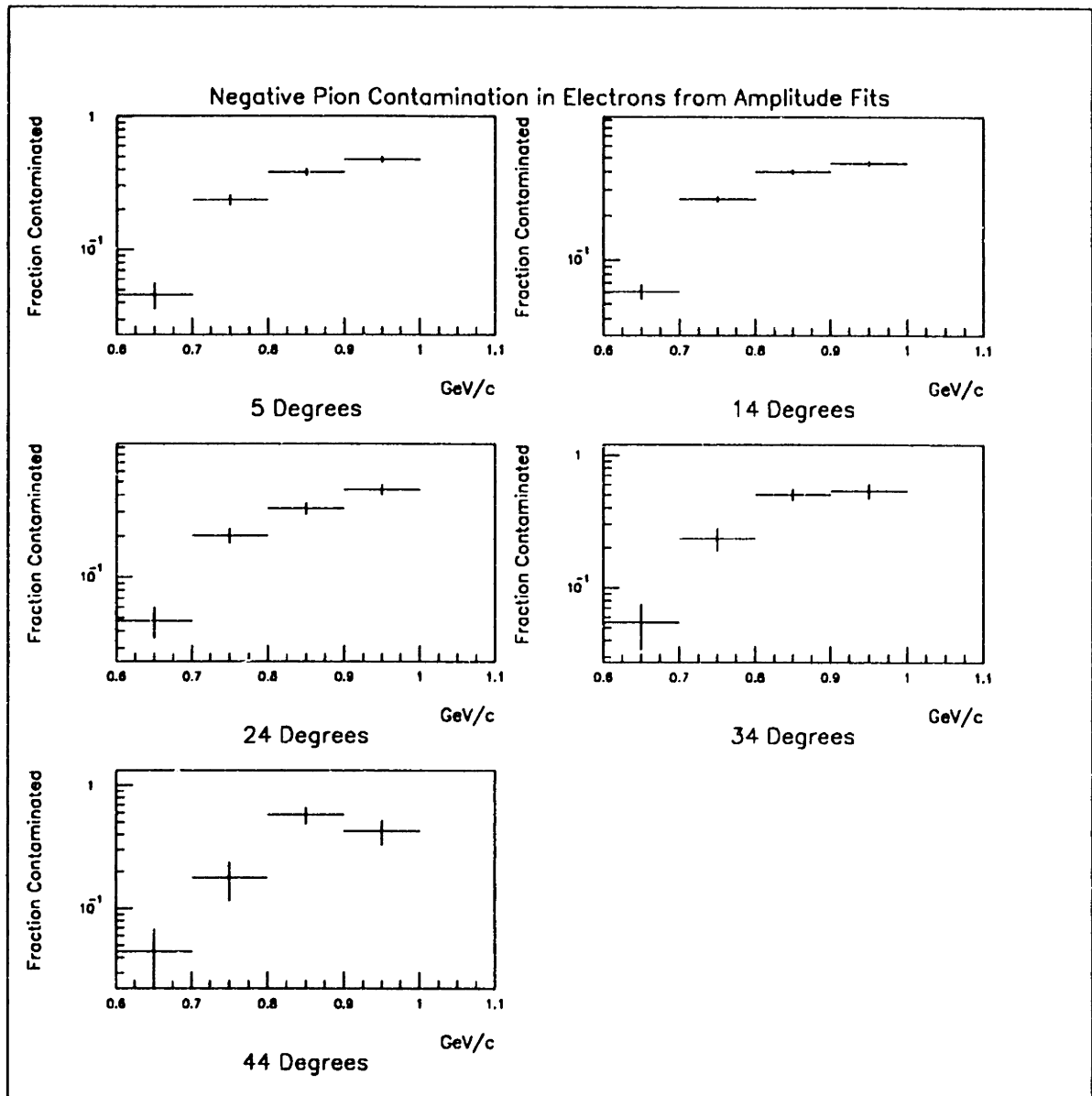
Figure H-3: Fractional Negative Pion Contamination of Electrons from Amplitude Gaussian Fits
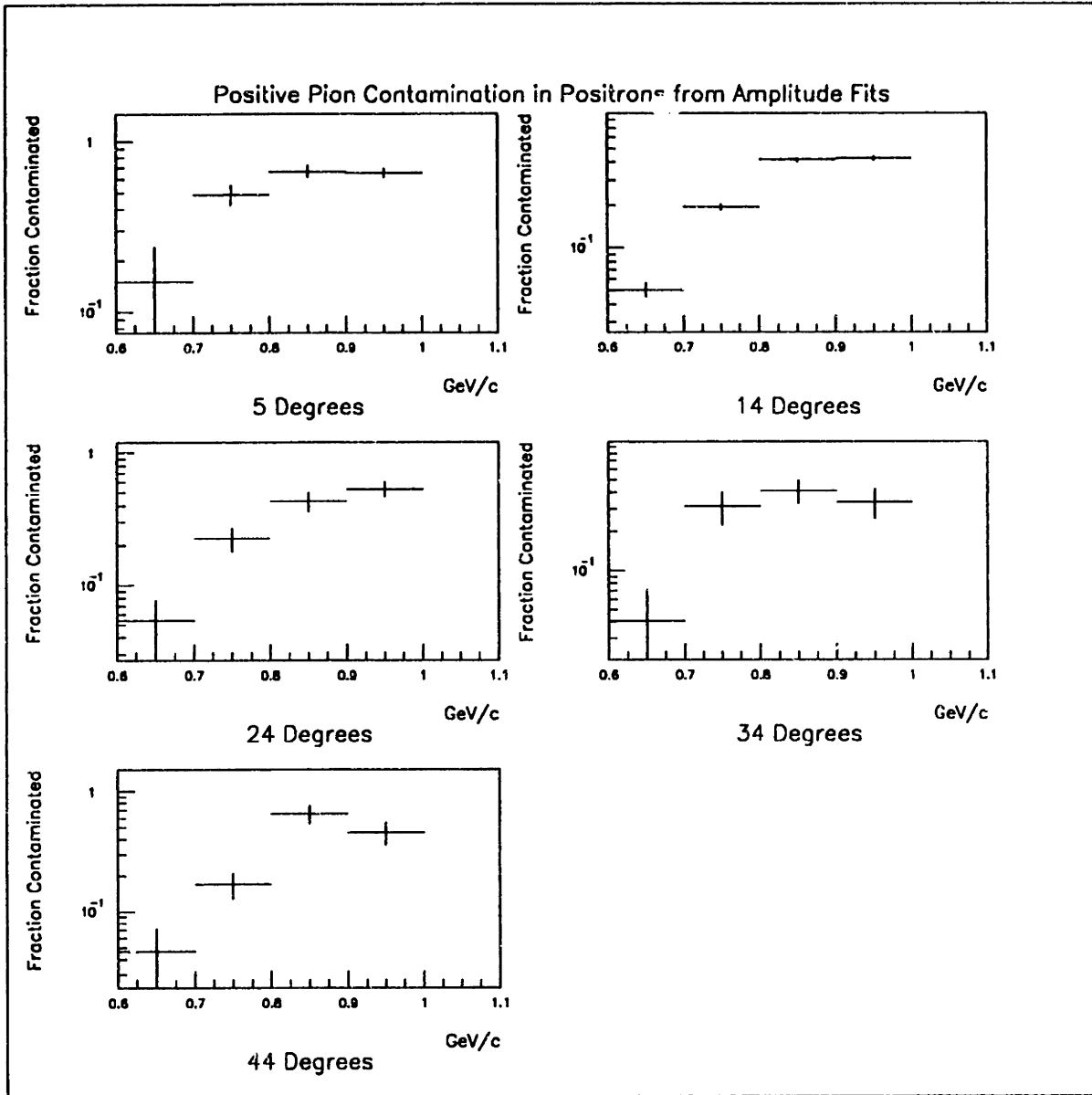
Figure H-4: Fractional Positive Pion Contamination of Positrons from Amplitude Gaussian Fits

Appendix I

Calculation of Errors in Contamination

Let contamination $= C = \frac{N_p}{N_p + N_e}$. Using error propagation and dropping the covariant term,

$$(\Delta C)^2 = (\frac{dC}{dN_p}\Delta N_p)^2 + (\frac{dC}{dN_e}\Delta N_e)^2.$$

Furthermore,

$$\frac{dC}{dN_e} = \frac{-N_p}{(N_p + N_e)^2}$$

and

$$\frac{dC}{dN_p} = \frac{N_e}{(N_p + N_e)^2}.$$

Presently, we will ignore the contamination errors due to the gaussian fits, and assume the uncertainties are approximately equivalent to the poissonian errors in the counts:

$$\Delta N_p \simeq \sqrt{N_p} \ and \ \Delta N_e \simeq \sqrt{N_e}.$$

Substitution yields

$$(\Delta C)^2 = (\frac{(-N_e\sqrt{nump})^2 + (N_p\sqrt{N_e})^2}{(N_p + N_e)^4})^{\frac{1}{2}}$$

reducing to

$$\Delta C = \frac{(N_e{}^2 N_p + N_p{}^2 N_e)^{\frac{1}{2}}}{(N_p + N_e)^2}.$$

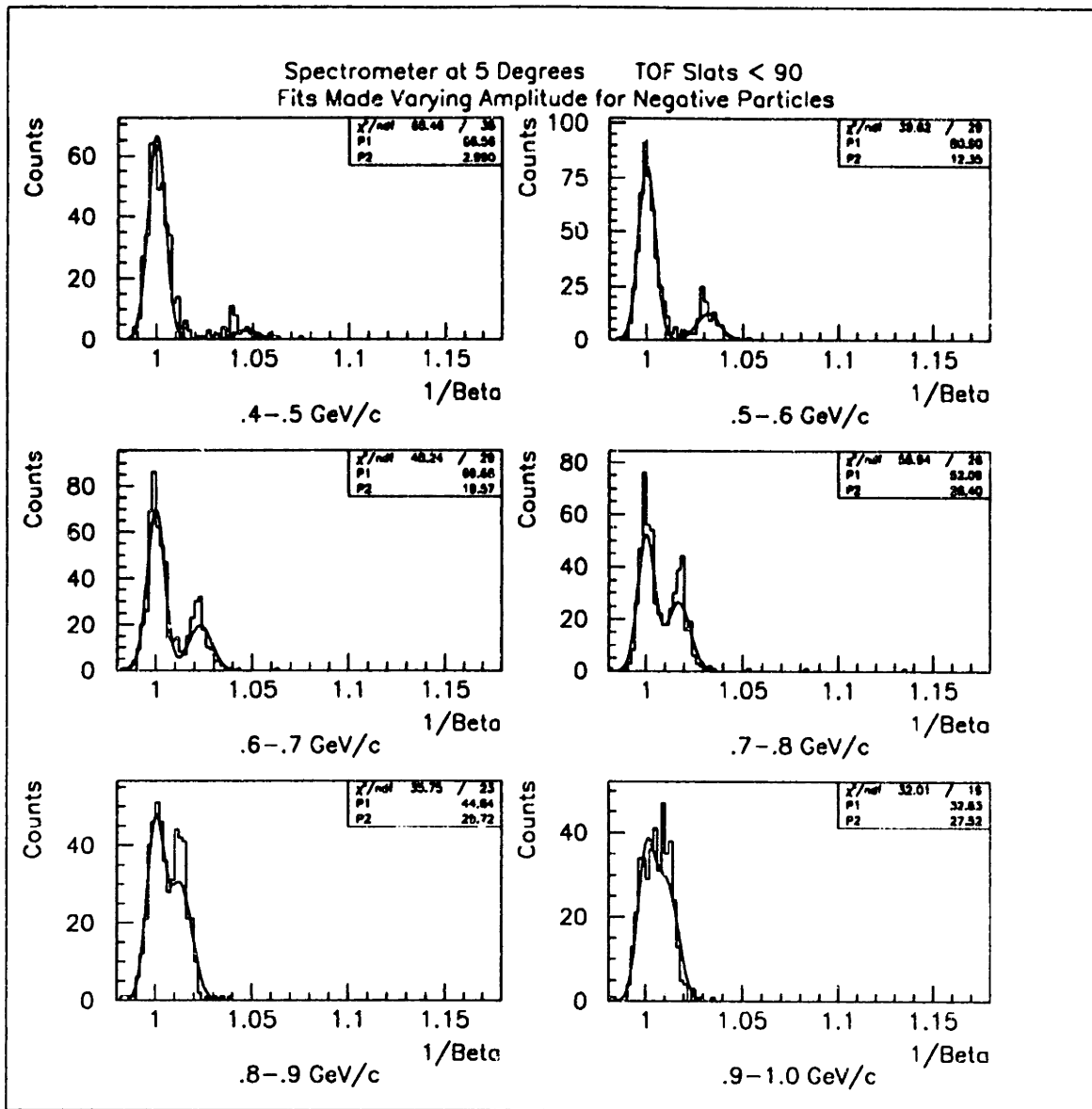# Appendix J

Gaussian Fits with Divided TOF Wall

Figure J-1: Gaussian Fit for Negative Particles Striking the Outside Half of the TOF Wall at 5° Spectrometer Setting
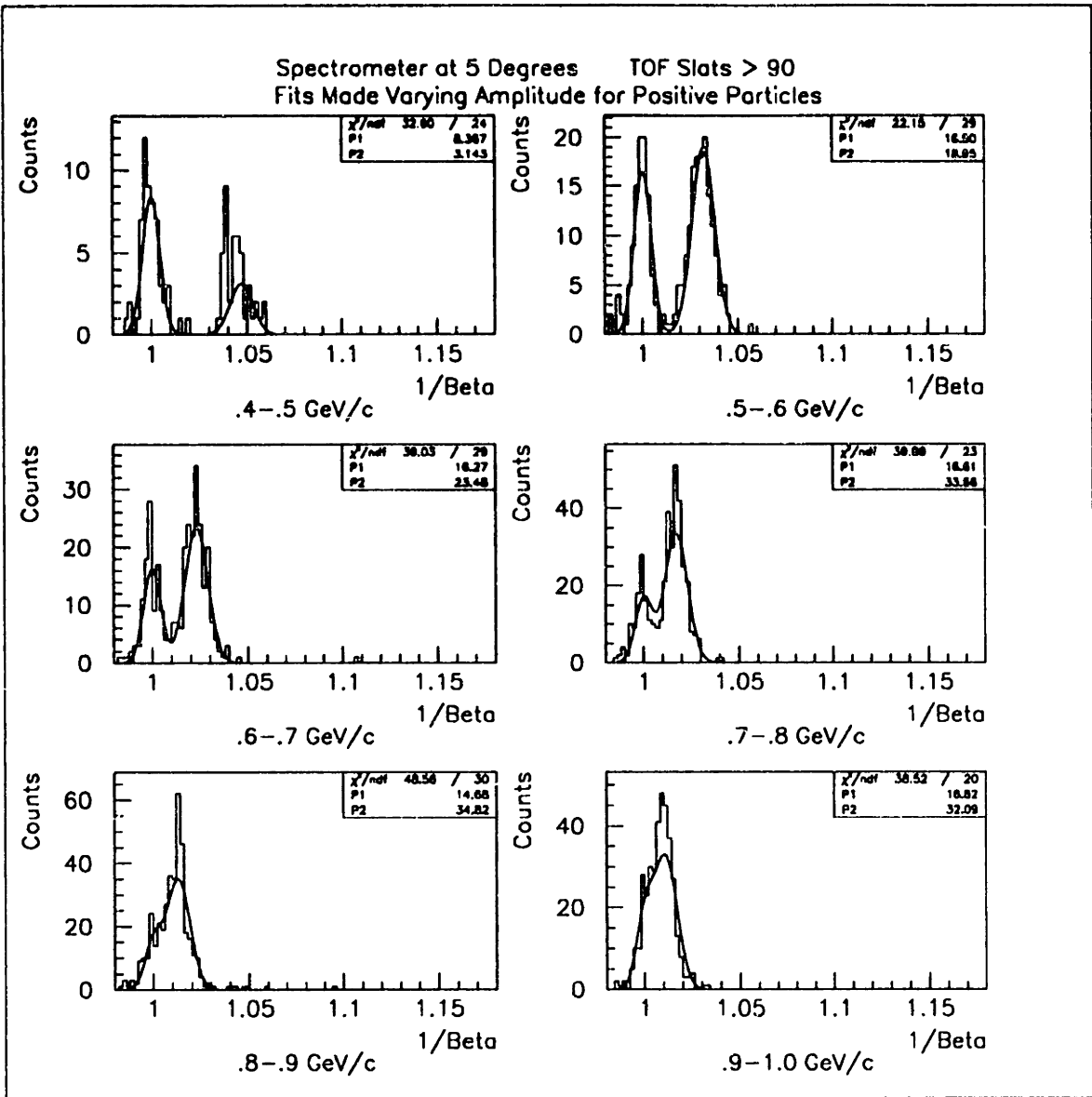
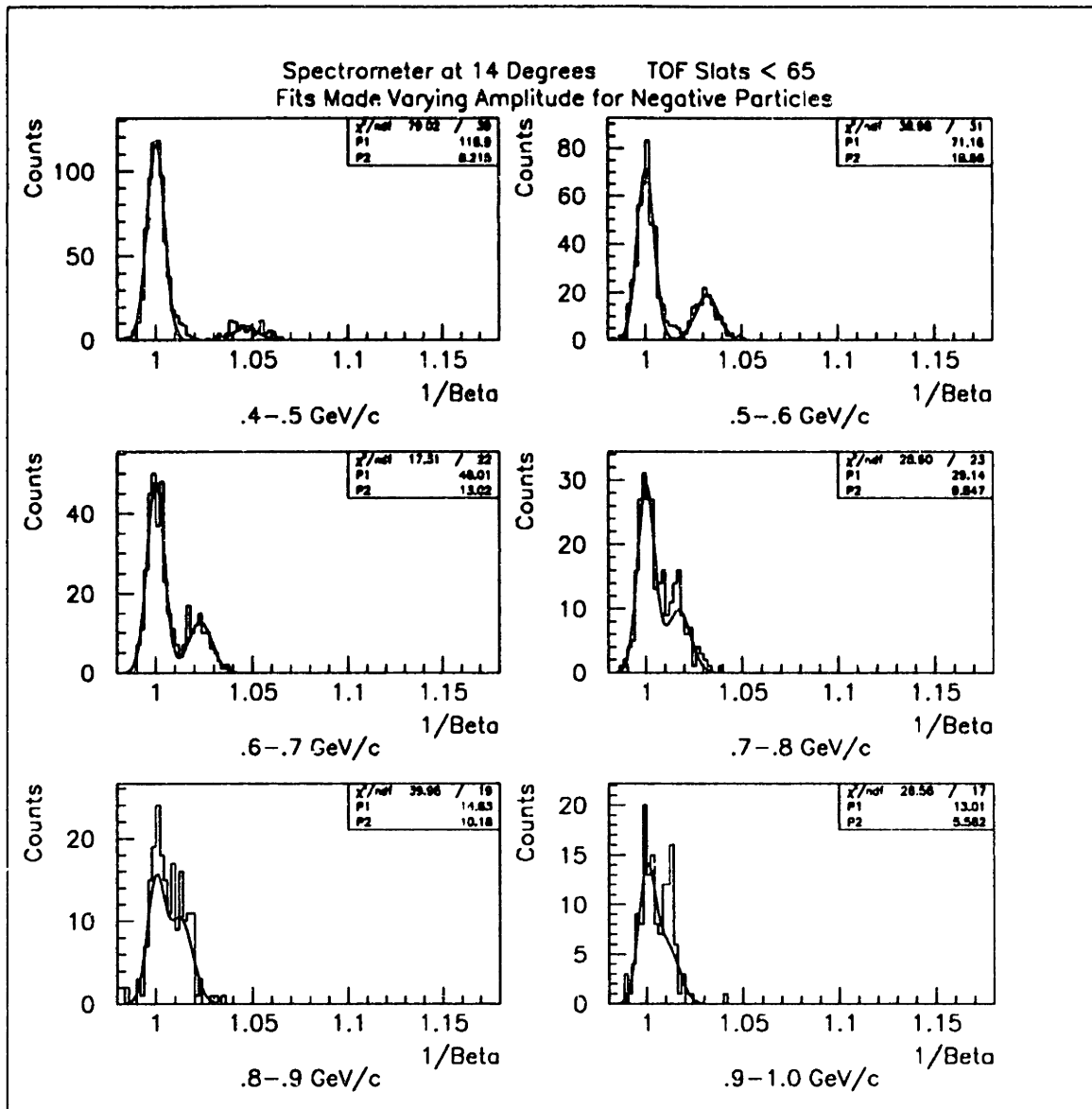Figure J-2: Gaussian Fit for Positive Particles Striking the Beam-Side Half of the TOF Wall at 5° Spectrometer Setting

Figure J-3: Gaussian Fit for Negative Particles Striking the Outside Third of the TOF Wall at 14° Spectrometer Setting
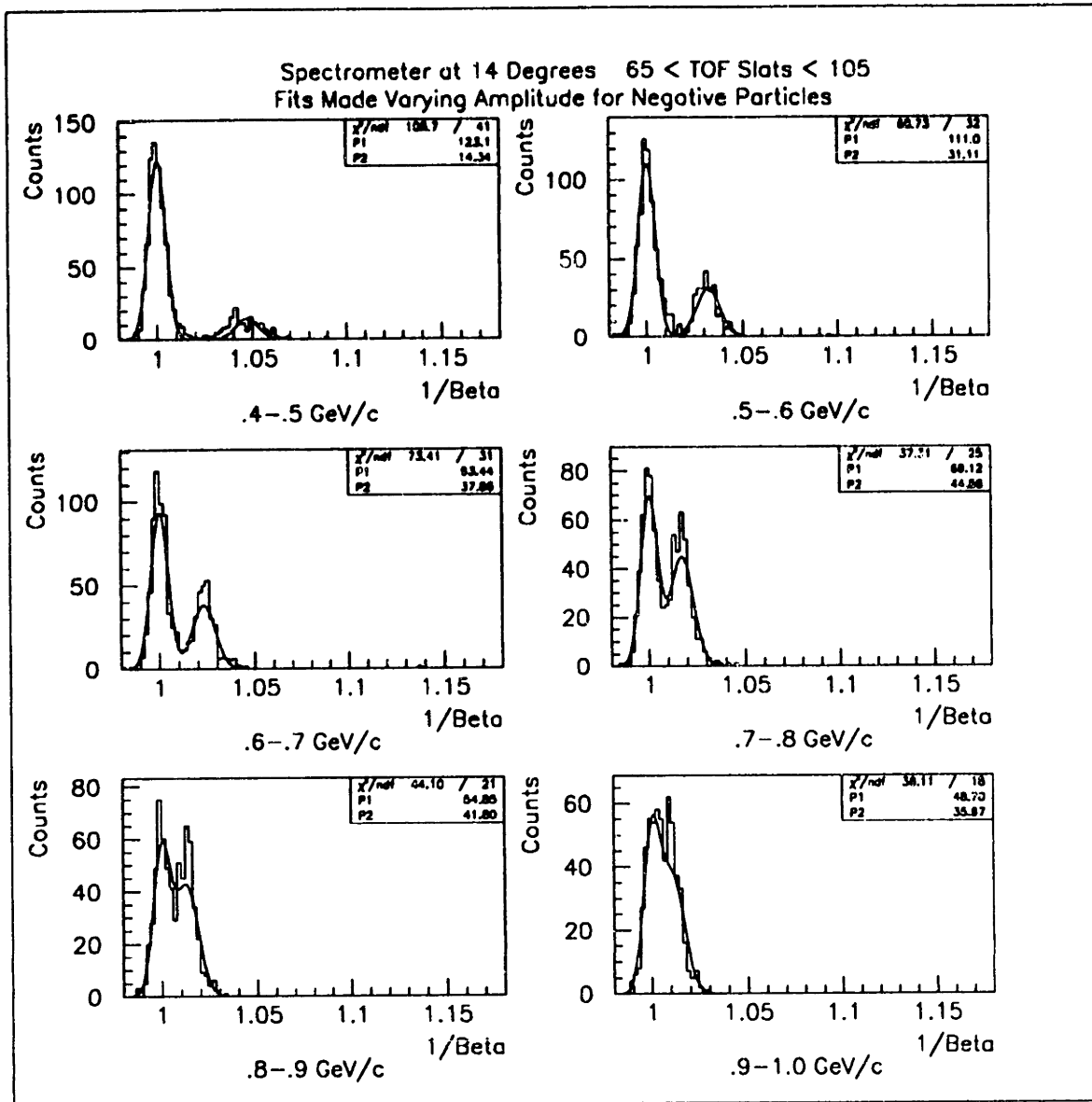
130

Figure J-4: Gaussian Fit for Negative Particles Striking the Middle Third of the TOF Wall at 14° Spectrometer Setting
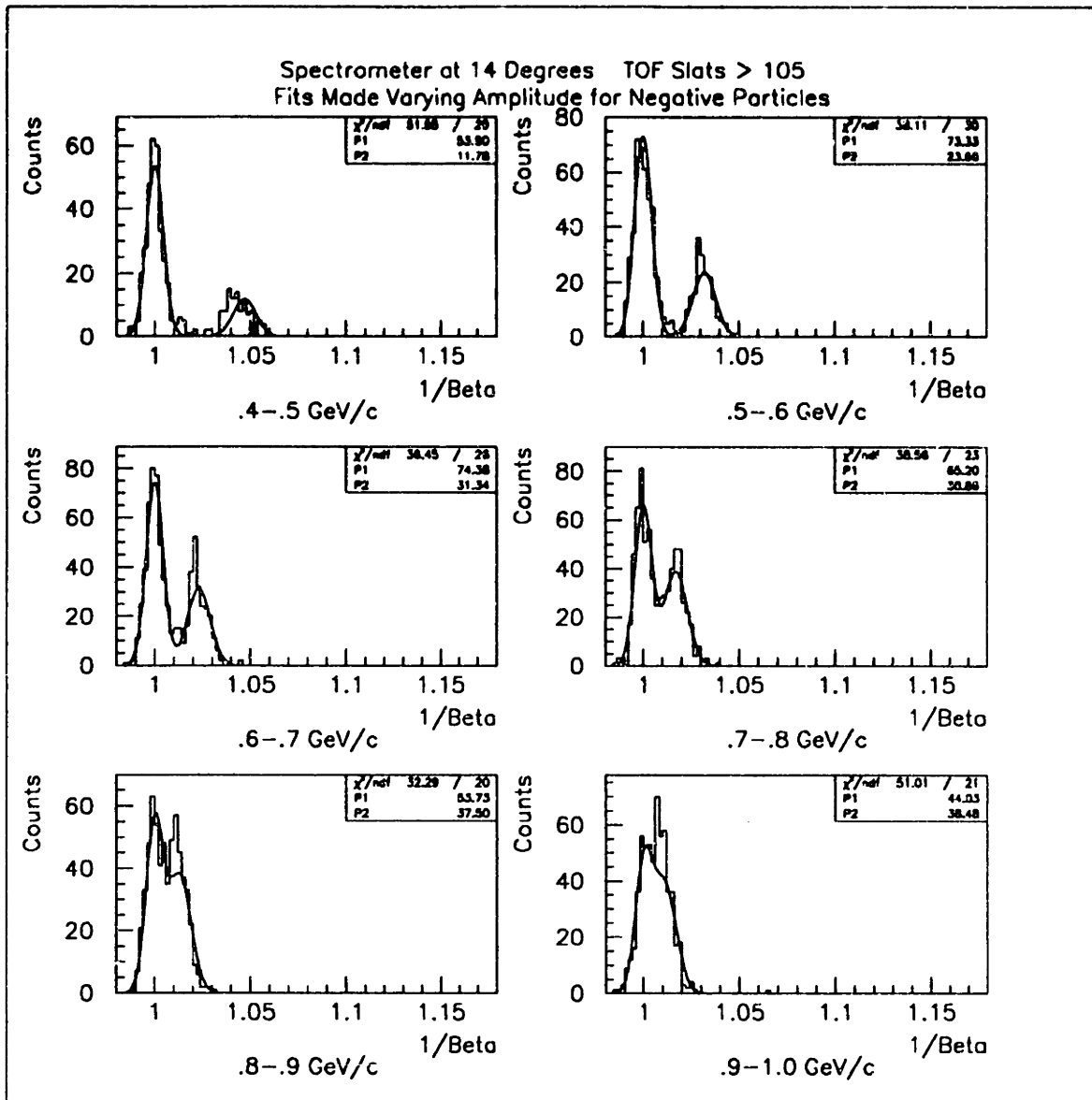
Figure J-5: Gaussian Fit for Negative Particles Striking the Beam-Side Third of the TOF Wall at 14° Spectrometer Setting
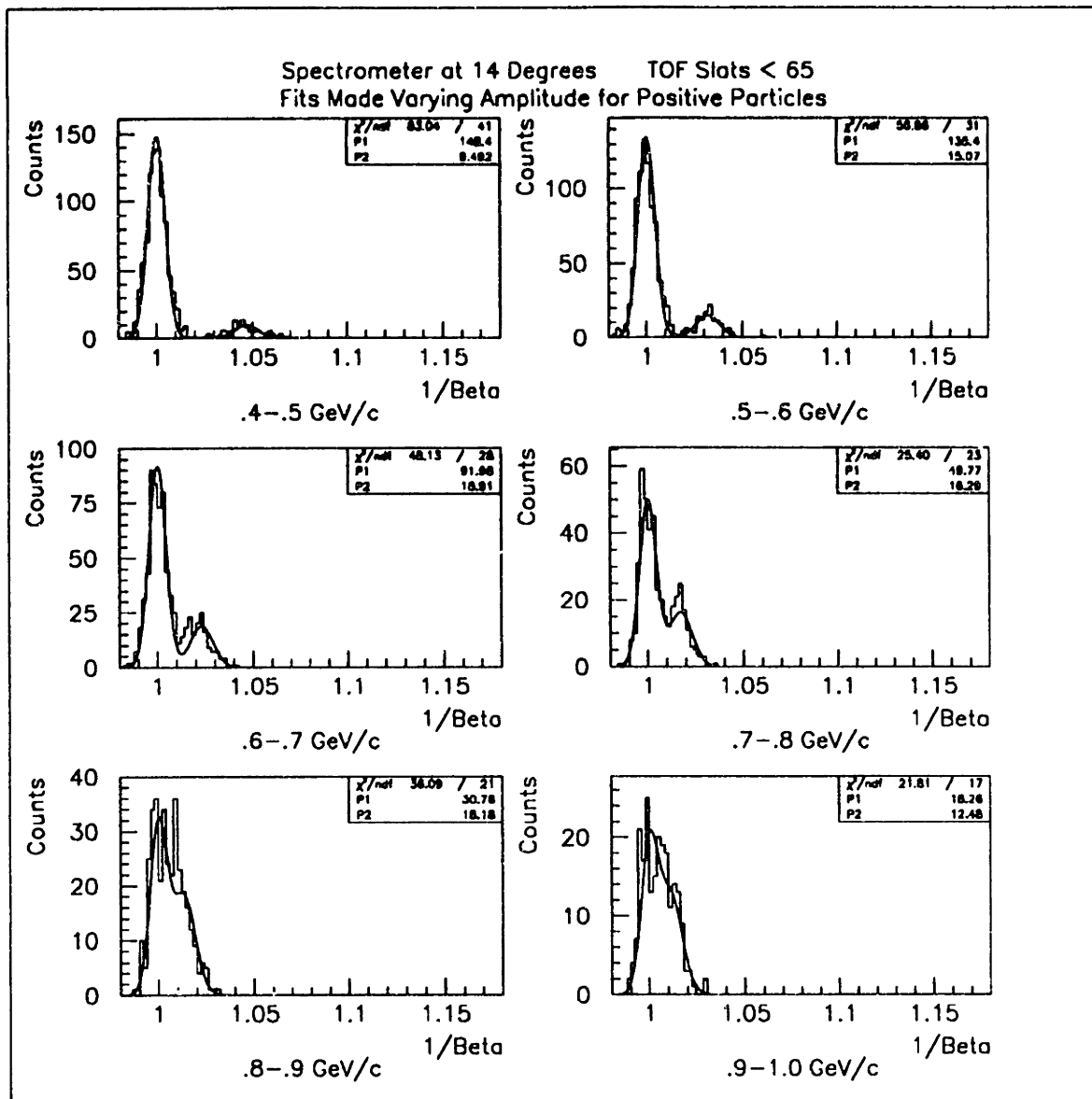
Figure J-6: Gaussian Fit for Positive Particles Striking the Outside Third of the TOF Wall at 14° Spectrometer Setting
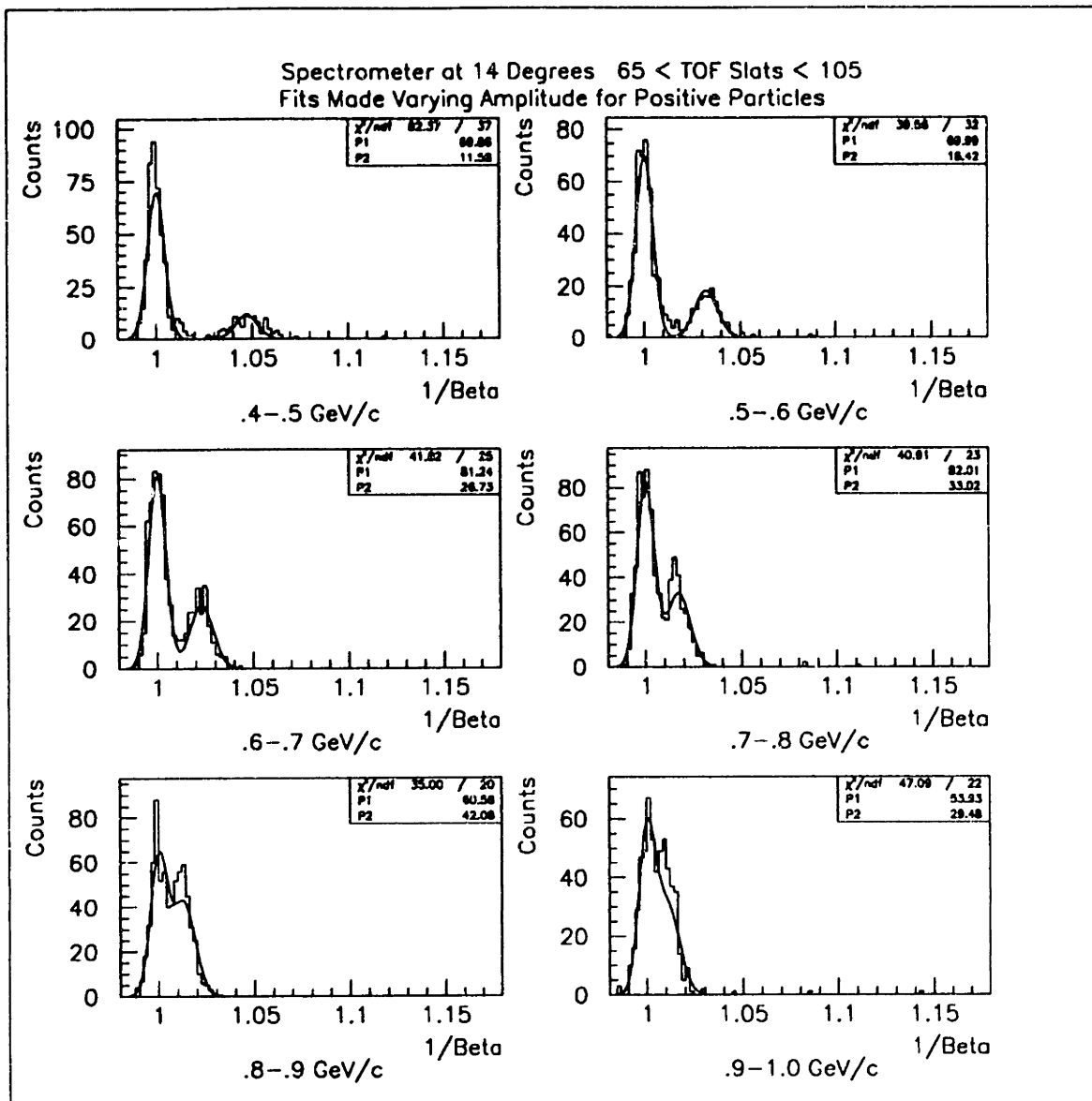
Figure J-7: Gaussian Fit for Positive Particles Striking the Middle Third of the TOF Wall at 14° Spectrometer Setting
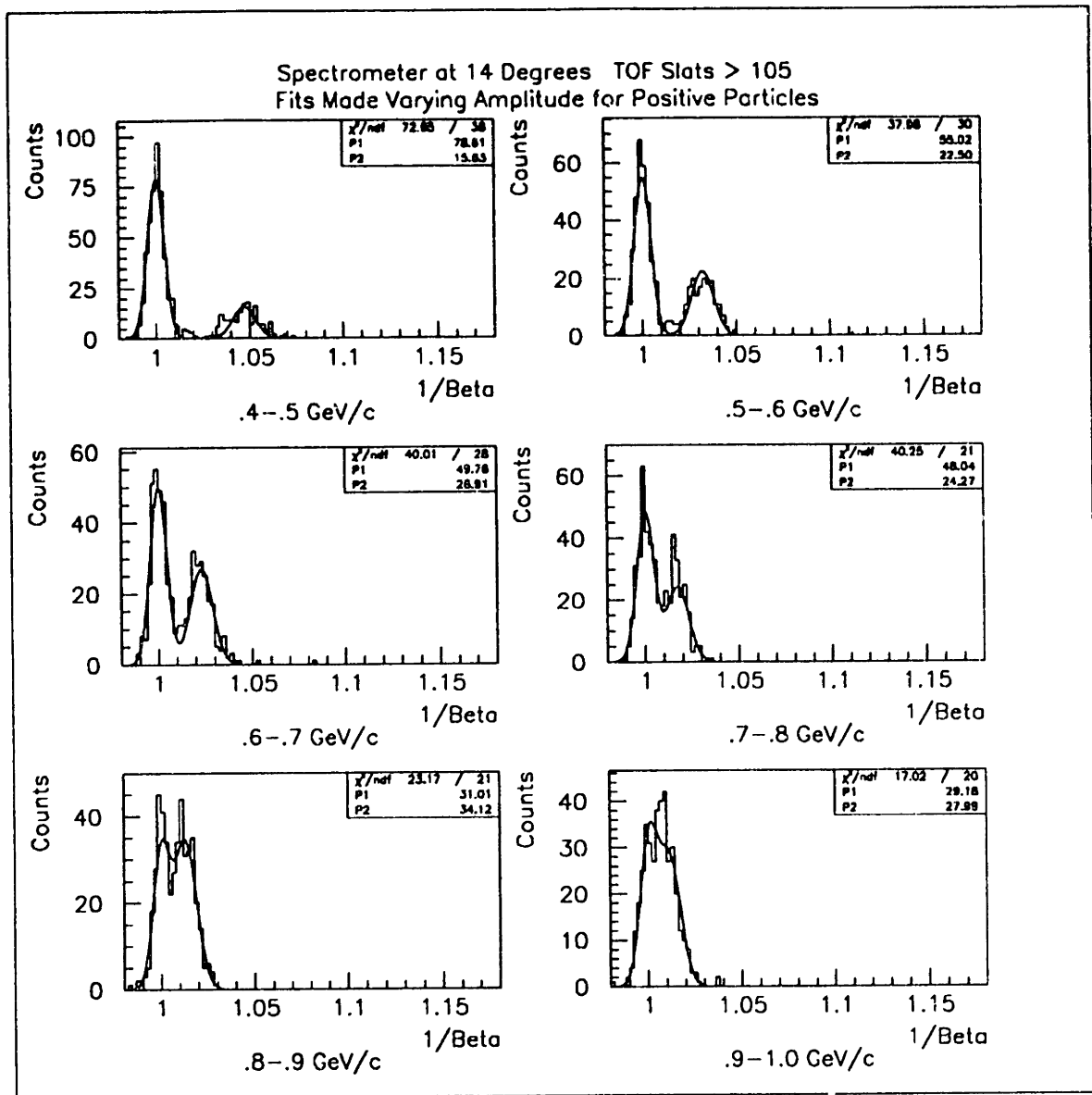
134

Figure J-8: Gaussian Fit for Positive Particles Striking the Beam-Side Third of the TOF Wall at 14° Spectrometer Setting